

Developing a genetic toolkit for plant-parasitic nematodes

Olaf Prosper Kranse

Hughes Hall,

Department of Plant Sciences,

Crop Science Centre,

University of Cambridge

This thesis is submitted for the degree of

Doctor of Philosophy, August 2023

Declaration

With this statement I confirm that this thesis is the result of my own work. Any collaborations or adaptations are addressed in the text and in this declaration.

There is a consortium dedicated to the work in Chapter 3: Transient expression and genome editing in plant-parasitic nematodes. The people included are: Sally Adams, Andre Pires-daSilva, Christopher Bell, Catherine J Lilley, Peter E Urwin, David Bird, Geert Smant, Godelieve Gheysen, John Jones, Mark Viney, Pierre Abad, Thomas R Maier, Thomas J Baum, Shahid Siddique, Valerie Williamson, and Sebastian Eves-van den Akker. All work shown in this Chapter was done by me.

The imaging robot was constructed together with Siyuan Wei and Sebastian Eves-van den Akker. In a collaboration with Ji Zhou and Jie Zhou, Nanjing Agricultural University, an AI was generated to automate nematode phenotyping.

This work is not substantially the same as any other work that has already been submitted for any degree or other qualification except as declared in the preface and specified in the text.

This thesis does not exceed the prescribed word limit for the Faculty of Biology Degree Committee (60,000 words).

ABSTRACT - Olaf Prosper Kranse - Developing a genetic toolkit for plant-parasitic nematodes

Nematodes belong to one of the most diverse phyla on the planet. Most nematodes are free-living and feed on bacteria, fungi, and protozoa. Plant-parasitic lifestyles are relatively rare in terms of numbers, however, through their parasitism these nematodes have a substantial impact on agriculture. They are estimated to account for over 10% of the annual life-sustaining crop losses, costing the industry roughly 100 billion U.S. dollars per year. There are two major groups of plant-parasitic nematodes: endoparasites and ectoparasites. The endo-parasites are the most economically important, and consequently the most widely studied. Endoparasitic nematodes, e.g., cyst nematodes, spend most or in some cases their entire life within the host, and feed exclusively on living host tissue.

Cyst nematodes alter the expression of a multitude of host genes, to coordinate the formation of a syncytial feeding-site. Loss in the ability to manipulate host genes required for the formation of this syncytium has a negative impact on parasitism: resulting in reduced nematode size and/or a reduction in the infection frequency. Given the intuitive pathways to impact from this fundamental understanding, there is considerable interest in the field to identify these, so called, susceptibility genes and the mechanisms by which they are manipulated.

This thesis describes and discusses efforts to expand the genetic toolkit for the plant- and nematode-side of the interaction to accelerate the study of the pathology as a whole. The thesis is principally focused on the model cyst nematode *Heterodera schachtii* due to its ability to parasitise the model plant *Arabidopsis thaliana*.

Knowledge on the nematode-side of the host-parasite interaction remains limited, partially due to the lack of functional genetic tools. Prior to this work, there was no method available to interrogate nematode gene "gain-of-function", and only one method (RNA-interference) available to interrogate nematode gene "loss-of-function". The first experimental chapter details a body of work aimed to address this constraint. It describes various attempts to deliver and express foreign genetic material in plant-parasitic nematodes using liposome-based transfection. Ultimately, the first gain-of-function experiments are demonstrated for any plant-parasitic nematode. Exogenous mRNA encoding eGFP and Luciferase are delivered to, and translated, *in Nematoda*.

On the plant-side of the interaction, functional genetic tools are already well established. The challenge is phenotyping of parasitism. Historically, infection is quantified by eye under the microscope. The main limitations of this approach are: 1) the relatively small number of technically tractable phenotypes (i.e., number of nematodes); and 2) the laborious nature of quantification. The second chapter describes efforts to lift both constraints using custom 3D

printed hardware and software to essentially digitise the assay. This new approach facilitates the measurement of infection, provides new phenotypes for analysis, and ultimately sets the stage for large-scale forward genetic screens.

Finally, the ability of this new screening method to facilitate the identification of new S genes was demonstrated. An experiment was conducted to measure the transcriptional response of *A. thaliana* shoot infection by *H. schachtii*. These data were cross-referenced to a published dataset of the transcriptional response of *A. thaliana* root infection to define a tissue independent response to nematode parasitism. To identify new putative S genes, a screen of mutants of differentially regulated genes was conducted using the new phenotyping capability.

Taken together, this work expands the tools available for the study of cyst nematodes demonstrating: 1) expression of exogenous genes *in Nematoda*; 2) digitisation of nematode phenotyping; and 3) identification of putative S genes by combining tissue-specific infection datasets.

Acknowledgements

To Sebastian Eves-van den Akker, for giving me the opportunity to do my PhD under his guidance. The PhD has been a life changing opportunity, for which I will be forever grateful. I have learned a lot of incredibly useful skills over the years which I will carry with me for the rest of my life. Thank you so much for everything.

I would like to thank the Biotechnology and Biological Sciences Research Council (BBSRC) and the University of Cambridge School of Biological Sciences for funding my PhD. It is a privilege to be financially supported throughout my career development.

Voor Ma en Pa, voor het nooit opgeven, voor het helpen en voor het blijven geloven. Ik hou heel veel van jullie allebei. Zonder jullie steun had ik hier vandaag niet gestaan. Hetzelfde geldt voor Opa, Oma en Sam. Je kan je niets beter wensen dan omringd zijn door zo veel liefde en mooie mensen.

To Marina, who stood by my side, who helped me continue, and will always keep me going. Thank you for all the love and support you have given me, and thank you for never saying no to takeaway.

And finally, to the amazing people I have met here in Cambridge. Without your help and support this thesis would not exist. A special thanks to, in no particular order: Anika, Francesco, Anna, Beth, Helen, Ko, Roberta, Unnati, Ji, Clement, Beatrice, Estefany, Jie, Kerry, Larry, Isabella, Victor, Siyuan, Thiago, Andrew, Carole, Thomas and Fernando, for their various help in and around the lab.

Table of Contents

1	Chapter one – General introduction	13
1.1	Nematodes	13
1.2	Nematode diversity	13
1.3	Parasitic nematodes	13
1.4	Plant-parasitic nematodes.....	14
1.5	Nematode control	14
1.5.1	Nematicides	14
1.5.2	Resistance	16
1.5.3	Susceptibility.....	16
1.5.4	Tolerance.....	16
1.5.5	Cultural practices	17
1.5.6	Accidental hosts.....	17
1.5.7	Bio-fumigation.....	17
1.5.8	Trap crops	18
1.5.9	RNA interference	18
1.6	Types of parasitism.....	18
1.7	Cyst nematodes.....	20
1.8	Nematodes as model species	24
1.9	Current research and limitations	25
1.10	Project overview	25
2	Chapter two - General materials and methods	27
2.1	Culturing nematodes.....	27
2.2	<i>Arabidopsis thaliana</i> growth	27
2.3	Inoculation of <i>Arabidopsis thaliana</i> with <i>Heterodera schachtii</i> in axenic culture.....	27
2.4	Nematode DNA extraction for PCR.....	27
2.5	Polymerase Chain Reaction.....	28
2.6	Ligation into a plasmid	30
2.7	Transformation, blue-white screening, and plasmid isolation	30

3	Chapter three - Transient expression and genome editing in plant-parasitic nematodes	31
3.1	Introduction	31
3.1.1	genetic tools in nematodes	31
3.1.2	Genetic tools in plant-parasitic nematodes.....	33
3.1.3	Aims	34
3.2	Materials and methods.....	35
3.2.1	Identifying genes of interest for targeting gene editing	35
3.2.2	CRISPR Design	35
3.2.3	Soaking of J2 <i>H. schachtii</i>	39
3.2.4	Detection of eGFP and mCherry	40
3.2.5	Detection of luciferase	42
3.3	Results.....	44
3.3.1	Expression of mRNA in plant-parasitic nematodes	44
3.3.2	Genome editing in plant-parasitic nematodes.	53
3.4	Discussion	63
3.4.1	Expression and detection of transgenes	63
3.4.2	Genetic modification via CRISPR-cas9 protein transfection	66
3.5	Conclusion.....	67
4	Chapter four – Automating nematode phenotyping	68
4.1	Introduction	68
4.1.1	Nematode infection assays and their limitations.....	68
4.1.2	Advancements in computer vision.....	68
4.1.3	Low-cost computing and the Raspberry Pi.....	69
4.1.4	Accessible 3D printing and design	72
4.2	Aims	72
4.2.1	Digitising the nematode parasitism assay	72
4.3	Materials and methods.....	74
4.3.1	Imaging of infection.....	74

4.3.2	Infection assay of <i>H. schachtii</i> on <i>A. thaliana</i>	75
4.3.3	QR code automation	77
4.3.4	Script-based counting and quantifiable traits.....	77
4.4	Results.....	78
4.4.1	The static device	78
4.4.2	Manually quantifying infection from images.....	81
4.4.3	The effect of root surface area on infection efficiency	81
4.4.4	Automatically quantifying infection from images.....	83
4.4.5	Reducing hand-on time.....	88
4.5	Discussion	91
4.5.1	Automation of nematode parasitism phenotyping.....	91
4.5.2	Plant physiology in nematode parasitism	93
4.6	Conclusion	94
5	Chapter five - Identifying a tissue independent response to nematode parasitism.....	95
5.1	Introduction	95
5.2	Screening for susceptibility genes.....	95
5.3	Identify the core transcriptional response to nematode parasitism	96
5.4	Aims	96
5.4.1	Develop and optimise the assay for shoot infection	96
5.4.2	RNA sequencing of shoot infected tissue.....	97
5.4.3	Identify key differences and similarities between tissues.....	97
5.4.4	Test the impact of the absence of core genes on nematode parasitism	97
5.5	Materials and Methods.....	98
5.5.1	Collecting leaf samples	98
5.5.2	RNA-seq analysis	98
5.5.3	Identify candidate genes based on root infection and leaf infection.....	99
5.6	Results.....	102
5.6.1	Optimisation of shoot tissue infection	102
5.6.2	Shoot infection for one time-point.....	106

5.6.3	Analysis of the conserved response.....	107
5.6.4	Susceptibility to infection for conserved upregulated genes	112
5.7	Discussion	118
5.7.1	Mapping the transcriptional response to <i>H. schachtii</i> parasitism of <i>A. thaliana</i> shoot tissue.....	118
5.7.2	The tissue-independent response to nematode parasitism	120
5.7.3	Conserved downregulated	121
5.7.4	Screening for susceptibility genes in the tissue-independent response to nematode infection.....	121
5.7.5	Limitations in susceptibility screening	122
5.8	Conclusion	125
6	Chapter six - General Discussion	126
6.1	A genetic probe to study the social behaviour of cyst nematodes	126
6.2	A fingerprint for syncytia, the where and the when.....	128
6.3	Screening parasitism genes through induced knockouts.....	131
6.4	Is susceptibility the right proxy for control?.....	132
6.5	General conclusion	134
7	Appendix.....	135
8	References	154

List of figures

- Figure 1.1: The structure of a fully functional syncytium. P. 23
- Figure 3.1: Pre-processing of confocal images for automatic fluorescence quantification and localisation. P. 46
- Figure 3.2: Expression of eGFP encoding mRNA in the plant parasitic nematode *Heterodera schachtii*. P. 48
- Figure 3.3: Detection of bioluminescence using various techniques. P. 50
- Figure 3.4: Detection of expressed luciferase from mRNA in the plant parasitic nematode *Heterodera schachtii*. P. 52
- Figure 3.5: Identification of putative ortholog of SQT-1 in *Heterodera schachtii*. P. 55
- Figure 3.6: Identifying template switching using nested PCR. P. 59
- Figure 3.7: The frequency of insertions and deletions. P. 61
- Figure 3.8: The frequency of base pair changes. P.62
- Figure 4.1: A Raspberry Pi 4B, and affordable small footprint computer. P. 71
- Figure 4.2: The static imaging tower. P. 80
- Figure 4.3: Quantifying root-surface area and visualising the effect on nematode parasitism. P. 82
- Figure 4.4: Comparison of contrasts, and quantification of infection on images taken using the static imaging tower. P. 84
- Figure 4.5: A visual representation of the effect of dye colour and light illumination on the visibility of *H. schachtii* on *A. thaliana*. P.86
- Figure 4.6: Quantifying female nematode infection using Morphological segmentation. P. 87
- Figure 4.7: Overview of working operations of the semi-automatic imaging robot. P. 90
- Figure 5.1: Various experiments trailed for shoot infection. P. 105
- Figure 5.2: Summary of the RNA-sequencing results from shoot infection of *Arabidopsis thaliana* with *Heterodera schachtii*. P. 108
- Figure 5.3: Results of RNA-seq analysis visualised. P. 109
- Figure 5.4: A STRING network of conserved upregulated genes during infection. P. 111

Figure 5.5: A schematic overview of the genes, and the locations of the potential T-DNA insert if present. P. 113

Figure 5.6: Genotyping of the confirmed homozygous lines. P. 114

Figure 5.7: The observed number of infecting females per tested genotype. P. 116

Figure 5.8: The observed female size per tested genotype. P. 117

Figure 5.9: A thought experiment for use of segregating lines as a means of reducing the genetic difference between the treatment (T-DNA insertion) and the control (wild type parent). P. 124

Figure 6.1: Observations of *Heterodera schachtii* males and J2s on petri-dishes with *Arabidopsis thaliana*. P. 127

Figure 6.2: A two component system to induce marker gene expression in nematode syncytia. P. 130

Figure 6.3: Number of nematodes in the field as a function of time for a given genotype of crop grown. P. 133

List of Tables

Table 1.1: A non-exhaustive list of nematicides. P. 15

Table 2.1: Thermocycle program used in amplification of DNA. P. 28

Table 3.1: A list of guide RNAs. P.33-36

Table 3.2: Different excitation wavelengths used to excite eGFP and mCherry respectively. P. 37

Table 3.3: The number of observed nucleic acid changes compared to the reference genome for two different base pair locations based on the donor fragment. P. 57

Table 4.1: Concentrations of used food dye in KNOP-medium. P. 76

Table 5.1: Primers used for genotyping. P. 100-101

Table 5.2: The success rate of aerial infection of shoots of *Arabidopsis thaliana* with *Heterodera schachtii* for varying nematode densities and inoculum volumes. P. 104

LIST OF ABRIVIATIONS

plant-parasitic nematodes (PPN)

resistance (R)

first-stage juvenile (J1).

infective second-stage juvenile (J2)

double stranded RNA (dsRNA)

cyst nematodes (CN)

initial syncytial cell (ISC)

polymerase chain reaction (PCR)

RNA interference (RNAi)

plasmid DNA (pDNA)

non-homologous end joining (NHEJ)

homology directed repair (HDR)

Basic Local Alignment Search Tool (BLAST)

general-purpose input/output (GPIO)

depth of field (DOF)

fused filament fabrication (FFF)

days post infection (dpi)

polylactic acid (PLA)

Acrylonitrile butadiene styrene (ABS)

Polyvinyl alcohol (PVA)

zinc chloride (ZnCl₂)

loxP flanked (floxed)

1 Chapter one – General introduction

1.1 Nematodes

Nematodes are worm-like organisms belonging to the phylum Nematoda and are the most numerous animals on the planet ¹, covering a range of lifestyles. The phylum Nematoda is a subset of the super-phylum Ecdysozoa, first described in 1997 through sequence similarity of 18S ribosomal DNA sequences in moulting animals ². These animals typically have a 3-4 layered cuticle, which is shed throughout various life stages ³.

Most known species are free-living, ranging from feeding on bacteria ⁴, fungi ⁵, algae ⁶, insects ⁷ to other nematodes ^{8,9}. Depending on the species, nematodes can vary in length from 700 µm (*Trichinella pseudospiralis*) ¹⁰ to eight meters (*Placentonema gigantissima*) ¹¹. At least 25,000 species of nematode have been identified, but the total number is estimated to be over 1 million ^{12,13}.

1.2 Nematode diversity

The molecular systematics of nematodes has been investigated in detail for over 20 years ¹⁴, and has changed drastically throughout its history. Chitwood's initial proposed classification divided the phylum into two classes: 1) Aphasmidia ¹⁶, later renamed Adenophorea ¹⁵, and 2) Phasmidia ^{16,17}, later renamed Secernentea ¹⁵. In 1998, based on phylogenetic analysis of small subunit ribosomal DNA sequences, five clades were defined: 1) Dorylaimida; 2) Enoplia; 3) Spirurina; 4) Tylenchina; and 5) Rhabditina ¹⁴. Further analyses of the mitochondrial DNA confirm the subclasses Dorylaimia and the order Rhabditida. Later, in 2006, Holterman *et al.* suggested a system containing 12 clades, dividing the previous class 'Secernentea', which included *Caenorhabditis elegans* and most plant and animal parasites into four separate clades ¹⁸. Throughout time, there has been much debate about nematode systematics. As recently as 2022, a new classification has been proposed by M. Hodda, comprising three classes, 32 orders and covering 28,537 species ¹⁹.

1.3 Parasitic nematodes

Parasitic lifestyles have devastating effects on human life. Somewhere between 20-50 % of the human population and nearly all living livestock are infected with at least one form of gastrointestinal nematode ²⁰⁻²³, with hookworm alone responsible for almost 60,000 human deaths per year ²⁴. Parasitic nematodes are also known to cause serious harm to incidental hosts. *Toxocara canis* (primary host *Canis familiaris*) can cause severe disease in incidental hosts such as *Homo sapiens* ²⁵. While most infections cause no symptoms, extreme cases could lead to neurological and ocular disorders ²⁶.

Parasitic nematodes, however, do not only impact society through direct parasitisation of the kingdom Animalia. Plant-parasitic nematodes (PPN) pose a significant threat through their impact on the economy and global food security.

1.4 Plant-parasitic nematodes

At least one species of PPN can parasitise every major crop²⁷. It is estimated that PPN cause around \$100–157 billion US in losses of crop per year^{28–30}, about 8.8–14.6% of total produce³¹. Agriculture makes up 4 % (\$4 trillion US) of the global gross domestic product (GDP)³², with in some developing countries accounting for 25 % of their GDP (Mar 31, 2023)³³. In 2021-2022 (most recently available statistic as of writing), the total income of crop output in the UK was £10,876 million (an increase of 20 % compared to previous years)³⁴. The most farmed crops for this year were: wheat (£2.7bn), barley (£1.2bn), potatoes (£703m), oilseed rape (£488m) and sugar beet (£216m)³⁵, totalling 22.4 million tonnes of crop food³⁵. For illustrative purposes about the potential damage of this pest, if the above estimates would apply to the UK, ignoring losses caused by other pests, somewhere between 2.1 and 3.8 million tonnes of food crops would be lost in the UK because of PPN alone.

1.5 Nematode control

1.5.1 Nematicides

There are various control strategies to combat PPN infection in the field. Traditionally, broad range nematicides are used. The first ever recorded event of the utilisation of any chemical to combat PPN was in 1881 when carbon disulfide was used to reduce infection of *Heterodera schachtii*³⁶. In recent years, most of the effective nematicides have been banned for use in agriculture due to concerns about the effects on human health, such as Vydate and Carbofan, which are the foremost effective nematicides against potato cyst nematodes (*Globodera* spp.). This leaves growers with only two alternatives: Nemathorin and Velume Prime^{37,38}. Importantly, Nemathorin is currently under review for renewal in both the EU and the UK³⁹, and Velume Prime offers relatively poor control over nematode populations on its own⁴⁰.

As shown in Table 1.1, most of the effective pesticides have seen their use banned due to human health or environmental concerns. Despite this, nematicide research has still seen growth in recent years⁴¹, which may be a direct result of the market size of \$1 billion US (2011⁴¹), which has risen to \$1.9 billion US in 2022⁴². However, the regulation trend is expected to increase with time, intensifying the interest in alternative solutions.

Table 1.1: Adapted and adjusted from: Food and Agriculture Organization of the United Nations ³⁸. A non-exhaustive list of nematicides. Most of these pesticides were allowed for use in 1992, since then their regulatory status has changed due to environmental and human health concerns. The regulatory status in this table reflects, * as of writing (2023), the European Union, the United States of America and ** Including the United Kingdom.

Crop	Nematode pest	Active compound	Brand name (if applicable)	Regulatory status in agriculture*
Potato	<i>Globodera</i> spp.	Aldicarb	Temik	Limited** ^{37,43}
		Oxamyl	Vydate	Banned** ⁴⁴
		Carbofuran	Furadan	Banned** ⁴⁵
		1,3-dichloropropene	Telone C-35	Banned ⁴⁶
		Metam sodium	Metam 510	Approved ⁴⁷
		Fosthiazate	Nemathorin	Approved ⁴⁸
		Fluensulfone	Nimitz	Banned ⁴⁹
		Fluopyram	Velum Prime	Approved ⁵⁰
		Carbofuran	Furadan	Banned ⁵¹
Tomato, cucurbits	<i>Meloidogyne</i> spp.	Aldicarb	Temik	Limited** ^{37,43}
		Ethoprophos	Mocap	Banned** ⁵²
		Oxamyl	Vydate	Banned** ⁴⁴
		Fenamiphos	Nemacur/ Femaniphos 400	Banned ⁵³
		Dazomet	Dazomet	Approved ⁵⁴
Citrus	<i>Tylenchulus semipenetrans</i>	Fenamiphos	Nemacur/Femaniphos 400	Banned ⁵³
		Aldicarb	Temik	Limited** ^{37,43}
Grape	<i>Meloidogyne</i> spp.	Fenamiphos	Nemacur/ Femaniphos 400	Banned ⁵³
	<i>Xiphinema index</i>	Aldicarb	Temik	Limited** ^{37,43}
Banana	<i>Radopholus similis</i>	Carbofuran	Furadan	Banned** ⁵¹
	<i>Helicotylenchus</i> spp.	Ethoprophos	Mocap	Banned** ⁵²
	<i>Pratylenchus</i> spp.	Fenamiphos	Nemacur/ Femaniphos 400	Banned ⁵³
	<i>Meloidogyne</i> spp.	Isazofos	Isazofos	Banned ⁵⁵
		Ebufos	Cadusafos	Banned ⁵⁶

1.5.2 Resistance

One of the most prominent measures to control nematode population in the field is resistant cultivars. Resistance refers to a defence response initiated by the host because of recognition directly or indirectly by a resistance (R) gene of a pathogen-derived signal^{57–59}. A subset of the known natural R genes against PPN is given in a summary by Laura J. Davies and Axel A. Elling (2015)⁶⁰. The first cloned resistance gene against PPN, HS1^{pro-1}, was identified in sugar beet against the cyst nematode *H. schachtii*⁶¹. Like in susceptible hosts, nematodes can migrate to the vascular cylinder and attempt syncytium formation. Once feeding has been initiated, however, activation of the HS1^{pro-1} R gene causes cells surrounding the syncytium to become necrotic, preventing the nematode from completing its lifecycle⁶².

The structure of HS1^{pro-1} has low similarity to the other identified resistance genes as it encodes for a leucine-rich protein containing a transmembrane domain. More commonly, R genes encode proteins that contain two structures: 1) a central nucleotide-binding site (NBS); and 2) a C-terminal leucine-rich repeat (LRR) region. The NBS site can bind ADP (inactive state) or ATP (active state)⁶³. The LLR is the variable domain and is generally accepted to be responsible for detecting pathogen-specific signals⁶⁴. The result of an activated R gene is typically denoted with a hypersensitive response, resulting in host cell death.

The most widely studied resistance pathway in cyst nematode infection is the activation of *Gpa2* via recognition of the secreted protein RBP-1 of *Globodera pallida*⁶⁵. The resistance gene H1 confers to resistance of various pathotypes of *Globodera rostochiensis*⁶⁶. Both these resistance genes are used in virtually all potato producing countries⁶⁷.

1.5.3 Susceptibility

Susceptibility is a term that describes the compatibility between the nematode and its host. To parasitise, nematodes use a plethora of enzymes and/or effectors to facilitate migration and parasitisation. Any incompatibility can have a direct impact on the ability of the nematode to parasitise. For example, the cyst nematode *H. schachtii* parasitises on its host by forming a feeding organ, termed the syncytium, by differentially regulating a subset of plant genes⁶⁸. One of the genes strongly upregulated in *A. thaliana* over the course of infection is *HIPP27*. A loss of function mutant of this gene reduces the number of infecting nematodes, syncytia size, female size, and overall egg number per cyst⁶⁹. As more recently discovered, a knock-out of AtPANB1, one of genes involved in vitamin B5 biosynthesis pathway, results in a reduction in number of females, smaller syncytia, smaller cysts, and egg count⁶⁸.

1.5.4 Tolerance

In agriculture, one of the most critical factors is yield. Damage contributed by nematode parasitism depends on a few factors: 1) nematode density; 2) nematode species; and 3) host

genotype⁷⁰. The minimum number of nematodes for a measurable burden to the host is called the tolerance limit⁷¹. Above this threshold, the plant yield declines exponentially with increased nematode density until the infection is saturated⁷¹.

While general areas on genomes conferring with tolerance have been mapped⁷², to this date, there remains relatively little known about the genetic components involved in tolerance as most studies have focused only on impact in the field^{70,73}. Nevertheless, tolerance is an important phenotype in agriculture, and in some cropping systems, like as sugar beet, is preferred over resistant but intolerant varieties with respect to yield⁷⁴.

1.5.5 Cultural practices

Once a population of nematodes exists in the field, it is stable for an extended period, e.g., cysts of *G. pallida* can survive for up to 30 years in the soil⁷⁵, with a spontaneous hatching rate of only 26 % per year, while the remainder lay dormant and only hatch in the presence of a host-specific hatching factor⁷⁶.

By growing non-hosts or resistant hosts between seasons of susceptible crops, the nematode population can be kept under the economic damage threshold. A complex calculation system determines the best-fitting crop rotation schedule. This depends on the nematode species, climate, crop, and other environmental and economic factors⁷⁵. These cultural practices can improve biodiversity and soil structure, increasing plant health and yield⁷⁵. However, some rotation schedules can quickly become economically unviable as complete cycles could be longer than five years of less profitable crops⁷⁶.

1.5.6 Accidental hosts

Naturally, our understanding of important pests through agricultural interest is centred around the most economically important crops. However, various weeds have been identified as hosts for PPN and can reduce the efficiency of crop rotation⁷⁷. As such, treatment of the field with herbicides showed a decrease in the nematode population of 37 %, compared to an increase in the untreated control field of 34 %⁷⁸.

1.5.7 Bio-fumigation

As discussed above, synthetic nematicides are becoming more restricted through regulations. However, a type of chemical control is gaining popularity, bio-fumigation. A frequently utilised method for bio-fumigation is using *Brassica* species as a cover crop. When the plant tissue is disrupted mechanically or by an herbivore, glucosinolates are released. Other plant cell types release myrosinase, which in the presence of water hydrolyses glucosinolates to thiocyanates, nitriles, and isothiocyanates, with the latter considered the most essential hydrolysis product as a biofumigant⁷⁹. In a field study, the use of *Brassica* residue reported a decrease of 44 %

in *G. pallida* and *G. rostochiensis*⁸⁰. However, *Brassicaceae* can be hosts for other species such as *Meloidogyne* spp., potentially increasing populations of other damaging nematodes⁸¹.

1.5.8 Trap crops

Whilst nematodes are in eggs inside cysts, they are protected from external environmental factors and can survive for over 30 years in the soil⁸². However, once hatched from their protective shells, the infective second-stage juvenile (J2) can only survive <2 weeks without a suitable host⁸³. Trap crops refer to plants that activate the hatching from the egg but are either resistant or non-hosts, preventing the nematode from completing its life cycle and thus reducing the number of nematodes in the field. This can be very effective (92-97 %) at reducing the observed *G. pallida* population⁸⁴. While the name trap crop sounds promising, it refers in general to plants that can induce nematode hatching but aren't susceptible. One such example is *Solanum sisymbriifolium*, one of the best trap crops for control of *G. pallida*. This weed however, is in most countries considered an invasive species⁸⁵, requiring special disposal measures making it an unattractive control measure⁸⁶.

1.5.9 RNA interference

Engineering resistance is always an attractive approach as it would allow for a targetable solution that can be created and amended to the requirements of the specific scenario. One such method revolves around the ability to silence nematode genes through RNA interference, as demonstrated in cyst nematodes⁸⁷, root-knot nematodes⁸⁸ and migratory nematodes⁸⁹. Stable expression of double stranded RNA (dsRNA) targeting a nematode gene crucial for successful parasitism could drastically reduce infection. The dsRNA could either be processed by the host to small interfering RNA and ingested by the parasite or processed internally, as demonstrated via soaking nematodes in dsRNA⁸⁸. This concept was first shown in dsRNA expressing tobacco, which managed to silence two housekeeping genes of *Meloidogyne incognita* resulting in at least a 90% reduction of infection⁹⁰. Since then, at least 39 targets over 12 nematode species have been identified⁹¹. In practice, this control measure has seen little use due to concerns about biosafety, such as off target effects on non-target organisms exposed to the genetically modified material⁹¹.

1.6 Types of parasitism

The term plant-parasitic nematode holds no phylogenetic value as PPN parasitise their host in a variety of ways. Below are a few examples of feeding behaviours with the associated plant phenotype. *Longidorus* spp. feed from outside the root and result in stunted host growth⁹². Some species are also critical viral vectors transmitting 13 known nepoviruses^{93,94}. *Paratylenchus* is another migratory nematode that does not enter its host⁹⁵. Through feeding on root epidermal cells, the nematode causes reduced plant growth, reduction in yield and

leaf chlorosis ⁹⁶. *Trichodorus* has a wide host range ⁹⁶, and through its feeding, damages the root tip, preventing elongation and causing “stubby”-looking root phenotype. Nematodes of the genus *Pratylenchus* typically cause damage by lesions formed in roots due to their migratory feeding inside the root ⁹⁷. These lesions remove a barrier of entry for bacteria and fungi, which can lead to secondary infections, such as *Verticillium dahlia*, resulting “potato early dying” disease ^{98,99}. *Radopholus* parasitises most notably on banana (*Musa spp.*) and *Citrus spp.* through migratory endoparasitism, leading to root necrosis, stunted growth and thinning of the canopy. Other root parasitic species, such as *Heterodera* and *Globodera* are cyst nematodes, that through sedentary feeding on a nematode-induced feeding organ result in stunted growth, wilted plants, and leaf chlorosis ⁹⁵. *Meloidogyne*, which are root-knot nematodes, also parasitise on their host via specialised feeding cells ⁹⁵. *Anguina* are gall-forming nematodes, mainly parasitising on grasses and seeds ⁹⁶.

Taken together, all soil-borne PPN species essentially either cause damage to the root system, impair water and nutrient uptake for their host in severe cases, are a vector for viral transmission, damage plant structures leading to secondary infections, or damage seeds.

From the abovementioned species, we can identify four types of feeding behaviour ¹⁰⁰.

1) Ectoparasite

Ectoparasitic nematodes, as the name suggests, are nematodes that remain outside the root as they feed. This inadvertently means the nematode is more exposed to external threats like predators and environmental factors ¹⁰¹. These nematodes may feed on various root tissue layers, depending on the length of their stylets ¹⁰².

2) Semi-Endoparasites

Semi-endoparasites are a group of nematodes that only enter the host with the anterior part of the body. For example, the semi-endoparasite *Tylenchulus semipenetrans* partially penetrates the root, feeding on 3-6 nurse cells ¹⁰³. The exterior part of her body sticks out of the host root and is believed to be required for mating with males ¹⁰³.

3) Migratory Endoparasites

In contrast to the ectoparasitic nematodes, endoparasites are relatively well protected from external factors, as most or all their life cycle is within the host. Typically, these nematodes have five total moulting stages: four juvenile moulting stages and one final adult stage. Among these parasites are *Pratylenchus spp.*, which have a broad host range. These nematodes feed on cortical tissue, causing cell death and necrotic lesions (typically as an indirect result of secondary pathogen infection of the damaged host tissue) ¹⁰⁴.

Stem and bulb nematodes are also migratory endoparasites but, do not feed on plant roots. Instead, they feed on the stems and bulbs of their host, causing diseases like onion bloat. This group also includes foliar parasites of the genus *Aphelenchoides* and *Litylenchus*¹⁰⁵. These nematodes feed on the epidermis and mesophyll tissues of leaves, which can lead to lesions and stunted plant growth¹⁰⁵.

4) Sedentary Endoparasites

Sedentary endoparasites spend most or all their lives inside their host. Like their migratory counterpart, these nematodes typically have five moulting stages. The key difference to migratory endoparasites is that sedentary nematodes remain feeding on one or more specialised nematode-specific feeding cells, for example, cyst and root-knot nematodes.

A member of this group of nematodes was the first ever described PPN. In 1743, John Turberville Needham wrote in his letter to the Royal Society after observing 'fibres' in a sample of blighted corn: 'I am satisfied they are a species of aquatic Animals, and may be denominated Worms, Eels, or Serpents, which they much resemble'¹⁰⁶. The species was later identified as *Anguina tritici*, which invades the plant's meristem, and migrate to the flower buds, where eventually nematodes convert the seeds into galls¹⁰⁷.

From the pests mentioned above, the sedentary endoparasites (i.e., cyst and root-knot) are among the most damaging in agriculture and, therefore, most widely studied.

1.7 Cyst nematodes

The group cyst nematodes (CN) belong to the subfamily Heteroderinae, containing eight subgenera: 1) *Heterodera*; 2) *Globodera*; 3) *Cactodera*; 4) *Dolichodera*; 5) *Paradolichodera*; 6) *Betulodera*; 7) *Punctodera*; and 8) *Vittatidera*. The first two genera are the most economically important⁷⁵.

While still inside the mother, eggs of CN initially contain an embryo which, through embryogenesis, develops into a first-stage juvenile (J1). For most CN, the first J1 moults within the egg into a second-stage juvenile (J2), equipping the nematode with a needle-like mouthpart called a stylet. The eggs at this stage, harbouring the dormant J2, are still contained within the cyst (the dead body of a female)¹⁰⁸. The species and environment depend on how long a J2 can survive this stage. The dormancy period can be divided into two types: 1) quiescence; and 2) diapause. Quiescence is a state that is reversed in the presence of favourable conditions, e.g., the presence of a suitable host¹⁰⁹. Diapause is a state dominant over quiescence as it persists despite favourable conditions. It is typically only broken by exposure to environmental conditions like cold, which can then be followed by favourable

conditions to break the dormancy ¹¹⁰. Through a combination of both these types of dormancies, the cyst nematode *G. rostochiensis* can survive for 20 years in the soil ¹¹¹.

Once hatching is initiated, the J2 will attempt to break free from the egg. There are different species dependent physical changes to the eggshell and behavioural adaptations of the J2 during the hatching process ¹¹². The nematode slowly forms a hole in the eggshell via a thrusting motion of the stylet, through which it eventually hatches ¹¹³. From this point forward, the nematode has a relatively short period in which it can survive without a host as it is an obligate biotroph. For example, while *G. rostochiensis* may lie dormant in the soil for 20 years, the hatched J2 will only survive for less than two weeks without parasitising ¹¹⁴.

The host releases a series of chemicals, which the nematode can recognise, and utilises to navigate towards the root ¹¹⁵⁻¹¹⁸. The J2 uses the stylet in a thrusting motion to penetrate root epidermal cells, gaining access to the host. This thrusting and migrating motion continue until the nematode reaches the vascular cylinder. The nematode stops using the stylet as a migration tool and utilises it to probe for cells to parasitise on. For *H. schachtii*, the target cells are procambial or pericyclic ^{119,120}. The stylet is carefully inserted into the host cell, and saliva from the oesophageal glands is injected. If there is an adverse reaction from the host cell, e.g., the collapsing of the protoplast, then the nematode will retract the stylet and continue searching for another suitable cell. If there is no adverse reaction, then the nematode will not retract the stylet, marking the formation of the initial syncytial cell (ISC) ^{119,121}.

The goal of the nematode is to transform the plant root cell into a multinucleate metabolically active feeding organ and maintain it for the remainder of its biotrophic stage. The modifications to the host cell are facilitated through stylet-mediated delivery of secretions from the nematode's oesophageal glands. The glands can be divided into a single dorsal gland and two subventral glands. Secretions from all glands are released through the stylet ^{122,123}. Whilst activity of both types of gland cells is observed in all life stages of nematodes, the subventral glands are primarily active in the stages leading up to and including the initial syncytial cell formation. In contrast, the dorsal gland is most active during the remaining sedentary stages ¹²². The genes encoding for these secretions are called parasitism genes or, more broadly, effectors ¹²⁴.

Shortly after the selection of the ISC, the J2 of *H. schachtii* enters a preparation period, decreasing the number of granules in the subventral glands while increasing them in the dorsal glands ^{125,126}. The stylet is withdrawn and re-inserted, and the nematode gland cell secretions are injected into the cytoplasm ¹²⁶. From this moment, the nematode starts withdrawing nutrients from the host cell through a specialised feeding tube. At this stage, the ISC and its nucleus are slightly increased in size, and the nematode stylet is covered by a callose-like

substance, which can also be found on the cell walls of neighbouring cells ^{127,128}. The ISC cytoplasm proliferates, and the vacuole reduces in volume ¹²⁹. Plasmodesmata sizes are increased between neighbouring cells of the ISC ¹³⁰, through which they eventually fuse ¹³¹. In later development, the growth is facilitated through the degradation of the cell walls of the syncytium and neighbouring cells, after which the fusion of plasma membranes allows for the incorporation of neighbouring cell protoplasts (Figure 1.1) ¹³². However, the outer most cell wall of the syncytium increases in width resulting in ingrowth around vascular tissue (Figure 1.1 B) ¹³³. Importantly, not every cell type is incorporated into the feeding organ. Fully differentiated xylem vessels are not, whilst metaxylem precursor cells are, leading to a syncytium that grows adjacent to the xylem or phloem vessels ¹¹⁹. This expansion of the feeding site continues until approximately 200 cells are incorporated ¹¹⁹.

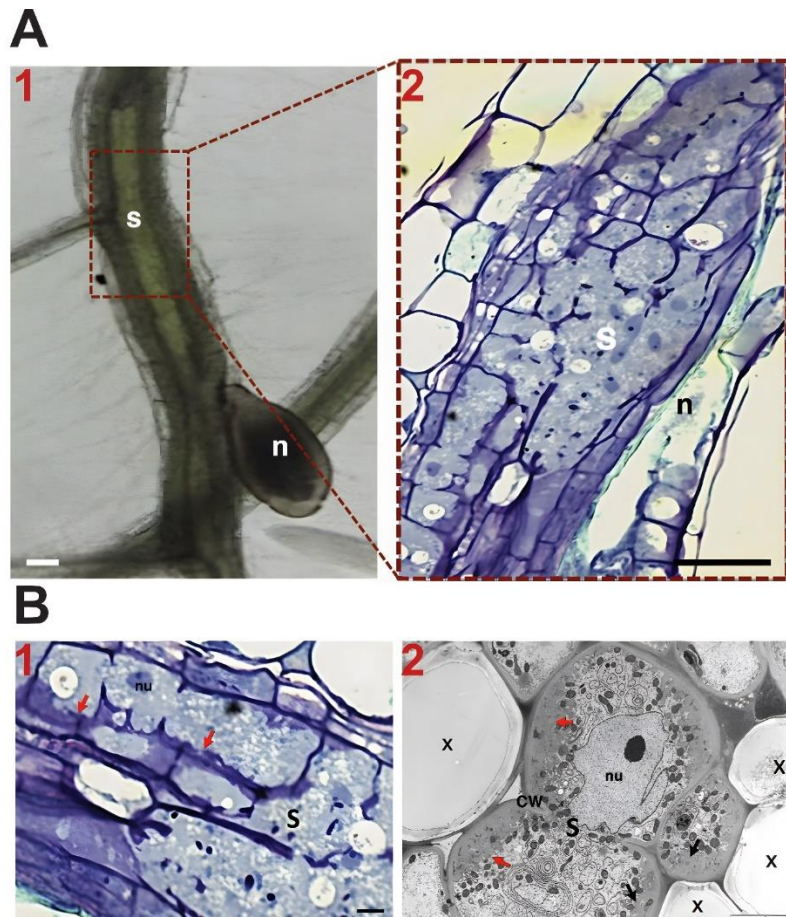


Figure 1.1 Adapted and adjusted from: Natalia Rodiuc et al. ¹³³. The structure of a fully functional syncytium. A) 1: *Heterodera schachtii* female parasitising *Arabidopsis thaliana* root. The root widening within the red box is the syncytium. 2: A cross-section of the syncytium showing the fusing of cells through the degradation of the cell walls and fusing of neighbouring cells. B) 1,2: Toluidine blue staining of syncytium, showing the thickening and ingrowth of cell walls (red arrows).

It is important to note that at the stage of initiation of the ISC, the nematodes are not sexually differentiated. Through various moulting stages, the nematode finally reaches maturity. While the exact mechanism remains unknown, it is generally believed that the nutrition provided by the feeding organ is a determining factor in sex differentiation¹³⁴. The developing female is estimated to require about 29 times more nutrition than males¹³⁵.

To indicate the time frame of these events, the following information describes development of the nematode based on an experiment of *H. schachtii* parasitising on *Arabidopsis thaliana* in axenic culture¹³⁶. Plants are inoculated with 200 J2s; this time-point is denoted as day zero. Within two days, 39 J2s had entered the root, with the majority already reaching the vascular cylinder. The growing feeding organ was visible from day three onwards, followed by some juveniles swelling on day four. By day six, 77 % of the parasitising J2s had started to moult, progressing to the J3 stage. The first following moulting stage was on day 10, progressing to J4. Importantly, not all nematodes matured to their final life stage, as 31 % stopped developing at the J4 stage. The first adult nematodes were females, observed from day 14 and shortly followed by males on day 17.

The female nematodes are shaped like a lemon and will remain attached to the root for the rest of their lives. Males have returned to a vermiform shape and spend the remainder of their life mating with females¹³⁷. The mated females eventually tan, turn to a cyst and die, filling the body with eggs that can provide protection for dormant J2s for decades.

1.8 Nematodes as model species

The phylum Nematoda is widely studied for its importance in ecosystems, medicine, agriculture, and its ease of use in a laboratory environment. The most well-studied nematode is *Caenorhabditis elegans*, a free-living nematode that feeds on bacteria. It has seen wide use as a model to study genetics and development due to its transparent nature in all life stages, relatively simple anatomy, being hermaphroditic, minimal nutrition requirements, high number of offspring, short lifecycle (few days), fully sequenced genome, and abundance of genetic tools. While there are some direct parallels between *C. elegans* and PPN¹³⁸, these comparisons are of limited value because they cannot include the host component. The optimal PPN model would have/be: 1) a host with a broad genetic toolkit; 2) various genetic resources; 3) easy to work with in laboratory conditions; and 4) an abundance of functional genetic tools. While there is no PPN that matches the above requirements, there are various species that make good parasitism models.

1.9 Current research and limitations

The closest to a model cyst nematode is *H. schachtii*, the beet cyst nematode, which can parasitise on the model plant species *A. thaliana in vitro*. Together with the broad genetic toolkit available for *A. thaliana*^{139–143}, these two species are attractive for studying nematode-host interactions^{69,70,144}. The transcriptional response to infection has been mapped in detail for various life stages of the nematode and is accompanied by a fully assembled genome of *H. schachtii*⁶⁸. Furthermore, large numbers of any life-stage can be obtained via axenic culture of infection of *Sinapsis alba*, which grows in the dark, allowing for storage of large quantities. Another crucial aspect for making this species suitable for laboratory research is the ability to induce hatching from the dormancy stage using zinc chloride¹⁴⁵.

While genetic resources are available for both sides of the interaction, there are currently no methods for assessing them efficiently. One of the most promising essays for determining the impact of host genetics on parasitism relies on axenic culture and manual quantification, which is limited in speed⁶⁹.

The lack of functional genetic tools also severely limits the study of PPN genetics. There is, to date, only one reliable functional genetic tool available to study PPN gene loss of function, RNA interference⁶⁸. Which is limited by nonspecific and off-target effects and only grants the ability to create knock-downs, no knockouts. There is currently no way to interrogate nematode gene gain of function.

1.10 Project overview

This introduction highlights a major constraint: the lack of tools and resources to study plant parasitic nematodes. This thesis aims to conduct a body of research that lifts the constraints by expanding on the tools and resources in the ‘plant-parasitic nematode genetic toolbox’. In the first experimental chapter of the thesis, I describe the first example of exogenous gene expression in any plant-parasitic nematode through delivery of marker gene encoding mRNA via liposome-mediated transfection. This work marks an essential first step towards stable transgenics as it overcomes one of the biggest hurdles: delivery of exogenous material to PPN¹⁴⁶.

The second experimental chapter focuses on a bottle neck on the plant side of the interaction: the speed of screening parasitism on plant genotypes. To screen for resistance or susceptibility, infection is typically compared between two host genotypes in a replicate of 30. The previous method would allow for the screening of three genotypes per day (one control and two genotypes of interest) and is mainly limited by the laborious nature of quantifying infection. In the second experimental chapter, I describe machinery and software that can

digitise the physical nematode infection assay. Recent years have seen rapid advancements in computer vision ¹⁴⁷, and thus we combine the digitised assay with computer vision software to improve infection quantification.

In the final experimental chapter, I provide a case study. Transcriptional analyses of the infection of *A. thaliana* by *H. schachtii* show that over the course of infection about 19,071 plant genes are differentially regulated. Any of these genes could be an S gene, but even with the improved screening method of the second experimental, this number of genes would be prohibitive to screen. In nature, cyst nematodes parasitise on roots; however, under laboratory conditions they can parasitise on leaves. I utilise this capability to generate a transcriptome of leaf infection and combine that with the existing root dataset to generate a tissue-independent response to nematode infection. I then combine this information with the novel screening capacity to interrogate plant genes of interest.

2 Chapter two - General materials and methods

2.1 Culturing nematodes

To culture *Heterodera schachtii* on *Sinapis alba*, seeds were surface sterilised with 20% v/v bleach (ThermoFisher) for 20 minutes and washed six times with sterile double-distilled H₂O.

The seeds were kept at 4°C overnight to improve and synchronise germination¹⁴⁸. The seeds were sown on sterile standard KNOP-medium (Duchefa Biochemie)¹⁴⁹ *in vitro* in a 150 mm sterile petri dish (SARSTEDT) for *S. alba*. The plants were grown on a 16-hour day at 21°C and 8-hour night cycle at 20°C in an MLR-352-PE growth chamber (Panasonic). Cysts were soaked in 3 mM Zinc Chloride (Sigma-Aldrich) to promote hatching¹⁵⁰ in a specialised hatching jar (Jane Maddern Cosmetic, 250mL) with two plastic rings 2.5 cm (alt-intech Tube Perspex) holding a 20 µm mesh (SIGMA-ALDRICH). Five days after hatching J2 nematodes that had passed through the mesh were collected by pipetting. Nematodes were washed five times with sterile double-distilled H₂O with 0.01% v/v Tween (Sigma-Aldrich) termed "nemawash". The density of nematodes was adjusted to 1 nematode/µL using sterile nemawash. Once *S. alba* reached an age of 14-21 days, the roots were inoculated with ~300 J2 nematodes by pipetting 300 µL of the suspension on the plate. After 10-12 weeks at 20-25°C in darkness, several generations of cysts had developed, and were ready for harvesting.

2.2 Arabidopsis thaliana growth

Seeds of *Arabidopsis thaliana* (Columbia-0, CS60000) were obtained internally and surface sterilised using the same methods as mentioned above. Sterilised seeds were sown on Gamborg b5 medium with vitamins (Duchefa), in 24-well plates (Sigma), or in 5 cm deep well petri dishes (Fisher scientific) under sterile conditions. Plants were grown under the same conditions as described above.

2.3 Inoculation of Arabidopsis thaliana with Heterodera schachtii in axenic culture

Nematodes were hatched as described above. Hatched J2 nematodes were collected by pipetting 5 days after hatching, and the concentration was adjusted to 1 nematode/µl with ddH₂O containing 0.01% v/v Tween (Sigma-Aldrich). At four weeks post germination, roots of *A. thaliana* were inoculated with 80 J2 nematodes by pipetting the suspension on the roots.

2.4 Nematode DNA extraction for PCR

Extraction from a pool of *H. schachtii* J2 nematodes was achieved with the methods below.

Roughly ~2000 J2 nematodes of *H. schachtii* were pipetted into a 1.5 mL microcentrifuge tube (Eppendorf). The worms were centrifuged at 13,200 rpm for 2 minutes in a 5424 R microcentrifuge (Eppendorf), and the supernatant was discarded. Using a micropestle, in a motion like screwing a screw with a screwdriver, the nematodes were homogenised. The genomic DNA was extracted using ChargeSwitch™ gDNA Mini Tissue Kit (Thermo-Fisher) according to the manufacturer's protocol.

2.5 Polymerase Chain Reaction

Amplification of a DNA sequence of interest was done using a polymerase chain reaction (PCR). Primers for amplification of genes were designed using the cloning function on the online software Primer3Plus¹⁵¹. The primers used for amplification are listed in Table 3.1 and Table 5.1, and the stock concentration was diluted from 100 µM to a 10 µM stock using nuclease-free water (Ambion). For ease of use, a MasterMix (MM) was made containing a final concentration 1x PCR buffer (Thermo-Fisher), 200 µM dNTPs (New England Biolabs), 0.5 µM of each Primer (Sigma-Aldrich) and 1.0 units / 50 µl Phusion DNA Polymerase (ThermoFisher). The MM was mixed by pipetting, and 49 µL was transferred to a 0.2 mL Dome Cap PCR Tube (StarLab). Finally, the genomic DNA template was added 50 µL of reaction mix. The PCR was carried out in a SimpliAmp™ Thermal Cycler (ThermoFisher) as described in Table 2.1.

The products were analysed by agarose gel electrophoresis, and the amplicon of interest was purified using a Monarch® DNA Gel Extraction Kit according to the manufacturer's protocol.

Table 2.1: Thermocycle program used in amplification of DNA.

Name of stage and frequency	Temperature in °C	Time in seconds
Stage 1 (1 times)	98	120
Stage 2 (40 times)	98	10
	TM of primer pair	10
	72	60
Stage 3 (1 times)	72	120
	4	Until collection of samples

2.6 Ligation into a plasmid

The amplified sequence of interest was given 3' A overhangs, using REDTaq® Genomic DNA Polymerase (Sigma-Aldrich) as follows; 30 µL of purified DNA was placed in a 0.2 mL Flat Cap PCR Tube (StarLab), added to this were 200 µM dNTPs (New England Biolabs), 13 µL of nuclease-free water (Ambion), 5 µL 5X REDTaq® polymerase buffer (Sigma-Aldrich) and 1 µL of REDTaq® Genomic DNA Polymerase (Sigma-Aldrich). The mix was incubated at 72°C for 30 minutes in a SimpliAmp™ Thermal Cycler (ThermoFisher). The DNA fragment was ligated into the pGEM-T easy plasmid (Promega) at 4°C for 1 hour according to manufacturer's protocol.

2.7 Transformation, blue-white screening, and plasmid isolation

To confirm successful ligation of the fragment, a blue-white screening was performed. The fragment was ligated into pGEM-T easy and transformed into chemo competent *Escherichia coli DH5alpha* and transferred to plates containing X-gal, IPTG and ampicillin according to the manufacturer's protocol (Promega). IPTG was used as an inducer for the lacZ gene¹⁵². The plates were then incubated overnight at 37 °C. White colonies were picked off the plates grown in LB overnight culture (10 g SELECT Peptone 140 (ThermoFisher), 5 g SELECT Yeast Extract (ThermoFisher) and 5 g Sodium Chloride (ThermoFisher)). DNA purification of plasmids was performed using the Monarch Plasmid Miniprep Kit (NEB) according to the manufacturer's protocol. To confirm the sequence of interest, the plasmid was Sanger sequenced using the service provided by Genewiz using the universal primers M13-40FOR and M13-40REV. The results were compared to the expected outcome using the MUSCLE alignment tool (EMBL-EBI).

3 Chapter three - Transient expression and genome editing in plant-parasitic nematodes

3.1 Introduction

A primary goal in the field is to understand nematode parasitism in enough detail to deliver routes to control. In other fields, investigation is accelerated by the abundance of available genetic tools ^{153–158}, only one of which is broadly available in plant parasitic nematodes (PPN); RNA interference (RNAi) ^{68,159}. Forward genetic approaches are mainly restricted to studies of natural variation in populations, essentially limiting research to a single reverse genetic approach. There is no method to express exogenous genes in any PPN, essentially eliminating the possibility of targeted genome engineering, and making both qualitative and quantitative studies via overexpression impossible.

3.1.1 genetic tools in nematodes

The most widely studied model species of nematode is the free-living *C. elegans* ¹⁶⁰. The field uses various genome engineering techniques such as CRISPR/Cas9 gene editing and RNAi gene silencing to study individual gene function ^{161,162}. The delivery of these techniques to the nematode is enabled by transfection.

3.1.1.1 Expression of exogenous genes

Transfection is the term that describes how foreign nucleic acids, including dsRNA, mRNA, and plasmid DNA (pDNA) are delivered into cells ^{163–166}. There are two types of transfections: stable transfection, and transient transfection. Stable transfection refers to long term expression, typically through extra chromosomal arrays ¹⁶⁷ or through integration into the genome ¹⁶⁸, which can lead to constitutive expression of the transfected gene ^{169,170}. Transient expression is typically performed via transfection of mRNA and is used to study the effect of a temporary knock-in or over-expression of a gene ^{171,172}. There are many techniques that can aid transfection. Some of the most utilised for DNA are: particle bombardment ¹⁷³, polyethyleneglycol (PEG) ¹⁷⁴, electroporation ¹⁷⁵, and lipid nanoparticles. In nematodes, exogenous gene delivery through pDNA, is predominantly achieved via micro-injection ^{156,176–178}. Often a gene of interest is co-injected with a reporter gene, for example the dominant roller phenotype *rol-6* encoding for a cuticle collagen ¹⁷⁹, or *myo-3::GFP*, a green fluorescent protein fused to myosin ¹⁸⁰. The injected pDNA typically assembles into heritable multi-copy extra chromosomal arrays ¹⁶⁷, producing stable expression in the offspring of the injected individual. Lipid nanoparticles are used as vesicles for delivery of proteins ¹⁸¹, small molecules, and nucleic acids (most notably mRNA based COVID-19 vaccines ¹⁸²). For nucleic acids, these

vesicles provide protection against nucleases, and facilitate entry into the cell predominantly via endocytosis ^{183–185}.

3.1.1.2 Targeted genome editing

Altering the genome of an organism through insertions, deletions, modifications, or substitutions of DNA nucleotide bases *in vivo* is referred to as genome editing. Since the 1980s, scientists have been able to alter the genome of an organism through homologous recombination using a segment of DNA including homologous arms, but the technique was limited by efficiency (few in a million cells), and by the random incorporation into the genome ¹⁸⁶. This limitation was overcome five years later by introduction of I-SceI, a rare cutting endonuclease (cut site: TAGGGATAACAGGGTAAT(-9/-13) ¹⁸⁷), into the mouse genome ¹⁸⁸, increasing the efficiency and targeting mechanism through introduction of a double stranded break. This discovery subsequently increased the efficiency of mutagenesis through the non-homologous end joining pathway ¹⁸⁹.

Targeted nucleases allow for more precise genome editing through modifying DNA binding recognition sites. In increasing order of feasibility, zinc finger nucleases (ZFNs) ^{190–193}, transcription activator-like effector nucleases (TALENs) ^{190,194–200}, and clustered regularly interspaced short palindromic repeats Cas systems (CRISPR/Cas) ^{201–208} are often used in genome editing. The difference between ZFNs and TALENs is the DNA binding domain. In ZFNs, an array of three to six zinc fingers, which each recognise approximately three base pairs bind to the DNA ²⁰⁹. In TALENs, the DNA binding domain consists of 33–35 amino acid repeats, each repeat can specifically bind to a single DNA base ¹⁵⁷. Fusion of the DNA binding domains of either of these tools to a Fok-I endonuclease can be used to induce targeted DSBs.

A more recently discovered RNA guided nuclease, CRISPR/Cas9 is increasingly popular due to its flexibility and ease of use ¹⁵⁵. In the active form, *Streptococcus pyogenes* Cas9 is bound to a guide RNA (gRNA). The gRNA consists of two parts, a tracrRNA (nuclease bound) and a 20-nt guide sequence called crRNA (complementary to target sequence of DNA). The crRNA and tracrRNA can be combined into a single guide RNA (sgRNA) via a linker loop ²¹⁰. The guide sequence binds the Cas9 nuclease to the target DNA via Watson-Crick base pairing ^{210–212}. The DNA is cleaved by the nuclease if the target DNA is preceded by the Cas9 protospacer adjacent motif (PAM) 5'-NGG ²¹⁰, resulting in a DSB. To induce genome editing, the DSB needs to be repaired.

There are two major DNA repair pathways, non-homologous end joining (NHEJ), and homology directed repair (HDR). While highly conserved in all three domains of life, there are some key differences between the repair pathways ^{213–215}, therefore the remainder of the introduction will focus on the nematode pathway. There is a balance in repair of DSBs in DNA

between accuracy and speed ^{216,217}. The first pathway, NHEJ, is error prone, but is very rapid and efficient ²¹⁸. The repair pathway begins by binding of the DNA ends of the highly conserved heterodimers of Ku70 and Ku80, protecting the DNA from resection, and blocking the repair of the DSB by other pathways ^{219–221}. Subsequent recruitment of DNA ligase 4 initiates the terminal ligation step which in turn repairs the DSB ^{215,221,222}. It is widely believed that the processing of the DNA ends causes the pathway to be error prone ²²³. Not all DNA repair pathways are active during every stage of a cell's life cycle.

The process of mitotic cell division can be subdivided by distinct intracellular events. Cells that can continue to divide but are not actively doing so are in a state of replicative dormancy, defined as quiescence (Gap zero (G₀)). Cells cycle during mitotic division through four distinct major phases: G₁, Synthesis, G₂, and finally mitosis. During the G₁ phase, the cell synthesizes mRNA and proteins required for the subsequent phases. Importantly, NHEJ is the only known DSB repair pathway in G₀ and G₁ cell lifecycle phases and is also active during G₂ ^{216,219,220}. Ultimately the G₁ phase transitions to the S-phase, resulting in DNA replication, histone synthesis, nucleosome replication and reestablishment of chromatin domains. Prior to mitosis, to prevent proliferation of DNA damage, the sister chromatids generated in the S-phase are used in the G₂-phase to repair damage of the replicated DNA via HDR pathway.

^{216,219,220}This repair pathway is only initiated at the site of a DSB during the S / G₂ phase, in the presence of a homologous strand of DNA, and unlike NHEJ, is essentially error free ^{224–227}. The pathway is initiated by 5'-to-3' resection of the DNA, which generates the required 3' single-stranded DNA overhang for HDR ²²⁸. A displacement loop (D-loop) is formed between the ssDNA overhang and the donor fragment ^{229,230}. Resolvases are involved in the termination of the repair process, integrating the sequence of the donor fragment into the genomic DNA ^{231,232}. Finally, the G₂ phase transitions to mitosis, leading to cell division.

3.1.2 Genetic tools in plant-parasitic nematodes

In plant-parasitic nematodes, RNAi is readily achieved via soaking in double stranded RNA. The ingestion of the RNA into the nematode is facilitated by octopamine, a pharyngeal neuro-stimulant that aids the uptake of solutions from the nematode's environment ^{91,159}. Unlike in *C. elegans* ^{233,234}, the exact mechanism for uptake of the genetic material into the cell remains unknown, but the effect is reproducible in most plant-parasitic nematodes.

3.1.3 Aims

Currently, elucidating true causal relationships between gene and function is held back by a lack of transformation; we are unable to express transgenes to test function, nor edit the genome of any plant-parasitic nematode.

The work in this chapter aims to design methods for: 1) transient expression of any gene in in plant parasitic nematodes; and 2) detect any genome modification because of CRISPR/Cas9 activity.

3.2 Materials and methods

3.2.1 Identifying genes of interest for targeting gene editing

Genes of interest were selected based on their expression level and/or putative function (assigned by sequence homology). Relative expression data for predicted genes was available through the lab in various life stages of the nematode *H. schachtii*⁶⁸. Putative functions were assigned by comparison to previously described genes of *C. elegans* and *Pristionchus pacificus* using the BLAST algorithm. Sequences of interest were aligned using MUSCLE²³⁵, and phylogenetic inference using TOPALi²³⁶.

A second batch of genes was selected that, when mutated, may result in a dominant and easy to score phenotype based on similar mutations in other species. Protein sequences of *P. pacificus* SQT-1 (PDM81196.1) and *C. elegans* PAT10 (NP_491501.1) were aligned to the *H. schachtii* transcriptome using the BLAST command line tool.

3.2.2 CRISPR Design

Virtually any locus can be targeted for CRISPR/Cas9 mutagenesis if it contains a PAM site. Potential gRNAs were designed using CRISPOR²³⁷, an online design tool, and picked by hand to find matching locations for the target sequence. Anti-parallel overlapping gRNAs have been shown in some cases to result in higher efficiency in HDR and NHEJ^{178,238}. The efficiency of the gRNAs is related to their off and on-target score, GC content and other parameters²³⁹. Off and on-target specificity could not be checked as an indexed reference genome of *H. schachtii* was required within CRISPOR, which was unavailable in the online tool. The gRNAs are listed in Table 3.1. Modification of the gRNAs (2'-O-Methyl at first 3 and last bases, 3'phosphorothiate bonds between first 3 and last 2 bases, Synthego) is indicated in the table. These modifications have been reported to increase editing efficiency, reduce immune responses and have reduced off target effects²⁴⁰⁻²⁴². The donor fragment required for HDR was designed to have ~50bp homology arms on both sides of the cut site containing an intended modification and can be found in Table 3.1.

Table 3.1: Guide RNAs. Modification refers to Synthego's chemically modified guide RNAs. Primers are listed below, and the TM was calculated using the NEB tm calculator. The lower case letter in the donor fragments indicate the base pair changed compared to the wild-type gene.

Guide RNAs	Sequence	Modified
Sg_TRINNITY_DN__25230_R	CACUCACAGCUCGUUGUAGA	No
Sg_TRINNITY_DN__25230_R2	AAUUGGGCAACUGAUCAGAG	No
Sg_TRINNITY_DN__25230_F2	GGCACUCGCCGUCGAUCACU	No
Sg_TRINNITY_DN__2433_F	UUUCGUAAAUGAACGUCUGC	Yes
Sg_TRINNITY_DN__2433_F2	AGAACACGGGAAUAACAAAU	Yes
Sg_TRINNITY_DN__2433_R	AAAUUGAUCCAAACUGAAAA	Yes
Sg_TRINNITY_DN__2433_R2	AGGGGGGAGGGGAGAGGGGU	Yes
Sg_TRINNITY_DN__15349_F	UCUUCUGUUCGGCUGCCAGC	No
Sg_TRINNITY_DN__15349_F2	AUUUCUGGACCUCUUUACCA	No
Sg_TRINNITY_DN__15349_R	AAGGAAGUGAUCUAGAAAUU	No
sg_TRINNITY_DN__1740_F	UUGAUUUAUCCAUGUUGGGG	Yes
Sg_TRINNITY_DN__10292_F	CAAUGGAACAAAGCAAAGGG	Yes
Sg_TRINNITY_DN__10292_F2	ACAAAGCAAAGGGUGGGGGG	Yes
Sg_TRINNITY_DN__10268_R	CUGAUUGUGAGCAUUUAAAU	No
Sg_TRINNITY_DN__10268_F	GAAAAGAGAGAAGGGACGCG	No
Sg_TRINNITY_DN__12736_R2	AGACGGAAUAUGC UAAAGGG	Yes
Sg_TRINNITY_DN__12736_R	AGGGGGGAAUCAAUUCUGGC	Yes
Sg_TRINNITY_DN__12736_R3	UGGACGGACGGAAACAAAAG	Yes
Sg_TRINNITY_DN__1231_F	UGUGAAGGGAAUUGGGGGGG	No
Sg_TRINNITY_DN__1231_R	UUUGAAUGAGAAUAGUUCGU	No
Sg_TRINNITY_DN__1231_F2	ACGGUGCCGUGCCCGUUGAG	No
Sg_TRINNITY_DN__1231_F3	GGGGGGAAUGACCAAAGUGA	No
Sg_TRINNITY_DN__2733_F	UGCAUUGGCAUUGCGCACCA	Yes
Sg_TRINNITY_DN__2733_R	UACUUUGGGCUGUUUCGCAA	Yes
Sg_TRINNITY_DN__2733_R2	UCCGCCUGGGAAAUGCUGGU	Yes
Sg_TRINNITY_DN__26019_F	CUAAAACUCAAAUAUGGUC	No
Sg_TRINNITY_DN__26019_F2	AUUAUGGUCUGGAACAGACC	No
Sg_TRINNITY_DN__26019_R	AAAUUUCACAAAUCCAAUCC	No
crRNAs	Sequence	Modified
Cr_TRINNITY_DN_10854_F	CAAUCCCGGCCGAAUACCG	No
Cr_TRINNITY_DN_10854_R	UGC UUACCGCGGU AUUCGGC	No
cr_TRINNITY_DN_14852_F	GUGAGACGUCAACAAUAUGG	No

cr_TRINNITY_DN_14852_R	CAUAUUGUUGACGUCUCACA	No
cr_TRINNITY_DN_4213_F	ACGAUAAAUACGACGUAUCA	No
cr_TRINNITY_DN_4213_R	AUACCACGAUAAAUACGACG	No
PCR primers	Sequence	TM
TRINNITY_DN_14852_Conf_F	GTGTACACCGCCACTTTTCCT	65
TRINNITY_DN_14852_Conf_R	GGTCCGTTTGTGTTGAATGCT	65
TRINNITY_DN_14852_Int_F	TTCCAACCGTGTGAGATGC	66
TRINNITY_DN_14852_F	CCTCGGCGTAATGAAAGTGT	66
TRINNITY_DN_14852_R	CTCAGCCCGATCGCTGT	66
TRINNITY_DN_4213_F	CTACCGCCACTTCAATCAAC	64
TRINNITY_DN_4213_R	CATCGCTCCAACCTGTGCC	64
TRINNITY_DN_8845_F	CGACGTGTTTCGAGCGCATTG	64
TRINNITY_DN_8845_R	ATTCGCGCGATGAGATG	64
TRINNITY_DN_25230_F	ACGGCATCGTCACCAACT	61
TRINNITY_DN_25230_R	ATGATTTGGGTCATCTGAAAAG	61
TRINNITY_DN_2433_F	CAGCAGAAGCACCAAACCTGA	66
TRINNITY_DN_2433_R	CCTCCCGCTTGTACTCCTC	66
TRINNITY_DN_15349_F	TACCATTTTTAATTCGTCTCAATTTT	59
TRINNITY_DN_15349_R	TTTCCGTTTTACCCAACA	59
TRINNITY_DN_1740_F	ACGGATACCCAAAGGGTTG	65
TRINNITY_DN_1740_R	ATTCCCATTAGTCAAAGTCTGTT	65
TRINNITY_DN_15452_F	TTTTGTAGAAAATGTCACCCAATG	61
TRINNITY_DN_15452_R	TTCGCCTAATTATATTGGTATATTGTG	61
TRINNITY_DN_10292_F	TAGCCGAATCAACGACTTTCA	65
TRINNITY_DN_10292_R	CCTTCTCCTCCTTCCTCTGC	65
TRINNITY_DN_10268_F	CTTCAGCCTCTCTTTTTCGCC	67
TRINNITY_DN_10268_R	CCGAATAGTACGGGTAAGCGT	67
TRINNITY_DN_12736_F	TTCATTCAATCCCTCGGTTT	62
TRINNITY_DN_12736_R	TCTTACGACACGCGGAATAC	62
TRINNITY_DN_1231_F	GGTCATTGAAATAGGCAAACG	63
TRINNITY_DN_1231_R	ACTTGGCTGCACTGGAAGAA	63
TRINNITY_DN_2733_F	TCCTATACTTTGGCGTATCTTTCT	64
TRINNITY_DN_2733_R	AAACCATGGCATTGAGGTGT	64
TRINNITY_DN_26019_F	TTTTTATTCCCTTAGAATTGGATTG	59
TRINNITY_DN_26019_R	GGCGGTGGAGCATGTAAAC	59

TRINNITY_DN_6558_F	TTTTCTCGCTGTATCTTTGACTCTT	65
TRINNITY_DN_6558_R	TCGACGTATTGTGGCACTG	65
TRINNITY_DN_21520_F	CGCTTTTATTGCCAACATGG	63
TRINNITY_DN_21520_R	ATTGGTCATTCATTAGCCCTTC	63
TRINNITY_DN_14852_F	CCTCGGCGTAATGAAAGTGT	66
TRINNITY_DN_14852_R	CTCAGCCCGATCGCTGT	66
TRINNITY_DN_4213_F	CTACCGCCACTTCAATCAAC	64
TRINNITY_DN_4213_R	CATCGCTCCAACCTCTGTCC	64
Donor fragments	Sequence	
DF_TRINNITY_DN_10854:	TCTGCCGCCCATTTGCCGCCTTTGGACAT TAACCAAATCCCGGCCGAAaggTACCGCG GTAAGCACAAGAAAAAAGCAATTTGGCCA GGCGAATAATAA	
DF_TRINNITY_DN_14852	GTTGATATGGTTAACTTGGAGCAGGAACC GCTTCCAACCGTGTGAGAtGcCAACAATATG GAGGATATGGAGCCACTGGTGTTCAGCCAC CAGCACCAA	

3.2.3 Soaking of J2 *H. schachtii*

Delivery of nucleic acids has been successful in PPN by soaking (based on delivery of dsRNA resulting in the reduction of gene expression via RNAi) and could be a low-tech solution for delivery of other molecules^{91,159}. In the experiments detailed below, the worms were soaked in a CRISPR or mRNA solution, containing a transfection reagent (Lipofectamine) and neuro-stimulant (octopamine) to facilitate uptake^{178,243}.

3.2.3.1 Soaking of CRISPR proteins

For each transfection experiment, at least three controls were performed: 1) treatment - containing all components of the CRISPR/Cas reaction and donor fragment for repair; 2) gRNA control – the same as 1) but replacing the gRNAs with those for a different gene; and 3) negative control - J2s without additional reagents. If necessary, gRNA was created from the two components crRNA and tracrRNA via hybridisation, annotated as crRNA:tracrRNA. To prepare the crRNA:tracrRNA, 3 µL Alt-R® CRISPR-Cas9 tracrRNA, ATTO™ 550 were added to 4 µL Nuclease-free Duplex Buffer and finally 1.5 µL of *each* Alt-R® CRISPR-Cas9 crRNAs (all provided by Integrated DNA Technologies (IDT)) was added to a 0.2 mL Flat Cap PCR Tube (StarLab) and incubated at 95°C for 5 minutes in a SimpliAmp™ Thermal Cycler (ThermoFisher).

The mixture was cooled down to room temperature, and 2.5 µL of either crRNA:tracrRNA or sgRNA was added to 2.5 µg Alt-R® S.p. Cas9 Nuclease V3 (IDT) and after 5 minutes a 100 bp long single-stranded PAGE purified DNA oligo (IDT) was added to a 1.5 mL Eppendorf tube (Eppendorf). The donor fragments and crRNAs sequences are listed in Table 3.1. The solution was diluted by adding 21.6 µL nuclease-free water (Ambion), and 3% v/v lipofectamine RNAiMAX (Invitrogen) or CRISPRMAX (Invitrogen) was added and incubated 20 minutes at room temperature to package the macromolecules into vesicles. Finally, octopamine (Sigma-Aldrich) was added to a concentration of 50 mM, and the mixture was combined with 2000 J2 *H. schachtii* and left to incubate at room temperature for eight hours.

DNA was extracted following the procedures in 2.4 of this thesis. Afterwards, the ssDNA oligo was digested by the addition of 3 µL exonuclease 1 (NEB) to 20 µL extracted DNA, 3 µL exonuclease buffer (NEB) and 4 µL nuclease-free water (Ambion). This was incubated at 37 °C for 15 minutes in an Eppendorf ThermoMixer® (Eppendorf) followed by an incubation of 80 °C for 15 minutes to inactivate the exonuclease. The remaining DNA was used to amplify fragments of the target site with PCR.

The Next Generation amplicon Sequencing service by Genewiz has some limitations. The maximum fragment size to be sequenced is 500 bp. This makes it impossible to sequence the entire gene, and separate primers were designed to amplify a region surrounding the target

site with the primers from Table 3.1. The amplicon was purified using the Monarch® DNA Gel Extraction Kit (NEB) according to the manufacturer's protocol. The concentration of the cleaned DNA product was determined using a NanoDrop (ThermoFisher) and the concentration was adjusted to 20 ng / μ L using nuclease-free water (Ambion). The samples were sent via courier to Genewiz UK, and then mailed to Genewiz Germany for sequencing.

3.2.3.2 *Delivery of mRNA*

Two fluorescent reporter genes (eGFP and mCherry) and one bioluminescent reporter gene (Firefly luciferase) were selected. Capped and poly-adenylated mRNA encoding these genes (Ozbiosciences) were used for transfection. Two different transfection reagents were used, CRISPRMAX (Invitrogen) and Lipofectamine RNAiMAX (Invitrogen) according to the manufacturer's protocol. Both lipofection reagents were optimised for delivery of different macro-molecules, while the manufacturer does not state the optimisations, CRISPRMAX is optimised for delivery of Cas9:sgRNA nuclease complexes, and RNAiMAX is optimised for delivery of dsRNA. Roughly 20,000 J2s of *H. schachtii* were pelleted in a 5424 R micro-centrifuge (Eppendorf) at 13,200 rpm for 1 minute. Nematodes were soaked in 12 μ g of mRNA; 12 % lipofectamine; 100 mM octopamine (Thermo-Fisher) for 12 hours.

3.2.4 *Detection of eGFP and mCherry*

Nematodes were immobilised on a 76 x 26 mm microscope slide (Thermo scientific) using a final concentration of 2 % sodium-azide and imaged on a Leica SP5 confocal system. The settings of the microscope are described in Table 3.2.

Table 3.2: Different excitation wavelengths were used to excite eGFP and mCherry respectively. The SP5 confocal used an argon laser set at 70% power.

Excitation wavelength in nm	Emission collection range in nm	Fluorophore	Gain
476	508-513	GFP	714
594	610-660	mCherry	851

3.2.4.1 Analyses of confocal images

From the confocal images the most in-focus optical slice of the z-stack was selected manually. For quantification, non-overlapping nematodes were cropped from the image and placed on a white background in Adobe photoshop 2020. Images were inverted and adjusted for visibility (Brightness -17%, Contrast + 71%, Intensity -27%). Any pixel in a nematode over 11 shades of variance from the background were counted using a custom script¹⁴⁶. The significance of the difference in the number of pixels per nematode between treatments was tested using an independent 2-group Mann–Whitney U test.

3.2.5 Detection of luciferase

3.2.5.1 Optimisation of detection methods

The most sensitive detection method for bioluminescence in house was experimentally determined. Three different methods were tested: 1) Amersham Hyperfilm ECL (GE Life Sciences); 2) G:BOX Chemi XRQ (Syngene) and; 3) CLARIOstar Plus plate reader (BMG Labtech).

A positive control of unknown concentration of Firefly luciferase was donated through the lab and was generated using TnT® Quick Coupled Transcription/Translation Systems (Promega) according to the manufacturer's instructions. Wells of 384 Deep Well Small Volume plate (Greiner Bio-One) were filled with 80 µL of PBS (137 mM NaCl, 2.7 mM KCL, 10 mM Na₂HPO₄, KH₂PO₄ 1.8 mM) and 10 µl of 100 mM VivoGlo Luciferin (Promega). A 10-fold serial dilution of luciferase was generated over 8 wells. The dilution series were immediately tested after mixing against the three detection methods. Both Hyperfilm and G:BOX Chemi XRQ (cumulative capture every 90 seconds) were exposed for 12 hours. The CLARIOstar Plus plate reader was exposed for 14+ hours for a range of PMT gain settings (1500, 2000, 2500, 3000, 3500, 4095 (maximum)). An additional range of nematode densities (50, 500, 1000, 2000, 2500 or 3750 *H. schachtii*) was trialled in the plate reader to test the interference of nematode density to luciferase signal.

3.2.5.2 Measuring luciferase in vivo and in vitro

The CLARIOstar Plus plate reader was used for the remainder of detections at the highest gain setting of 4095. Soaked nematodes were resuspended in 240 µL nuclease-free M9 buffer and distributed over 8 wells to generate technical replicates of measurement. A CAPP® 8-Channel Pipette (Starlab) was used to add 10 µl of 100 mM VivoGlo Luciferin (Promega) at the same time. The CLARIOstar plate reader was set up to vortex after each measurement at 300 rpm. The plate was sealed with a Corning® microplate sealing tape to avoid evaporation.

3.2.5.3 *Measurement analyses*

A non-linear model was created to compare luminescence as a function of time. The formula: $\text{Intensity} = a + b * 2^{(c * \text{time})}$ was used to describe the 16 time series (8 series for mRNA soaked, 8 for controls). In R the following command was used to fit the model: `'nls(y~a + b * 2^(c*time), start=list(a=1000, b = 1000, c = -0.0001))'`. The half-lives of the signal ($- 1 / c$) were used to compare between treatments using an independent 2-group Mann–Whitney U test.

3.3 Results

3.3.1 Expression of mRNA in plant-parasitic nematodes

Based on efforts within the field (personal communication) and efforts within the lab, microinjection in PPN remains prohibitively difficult. Typical macromolecule delivery to nematodes is achieved via micro injection, in which the cuticle is penetrated with a hollow needle containing liquid and payload. This liquid is then ejected from the needle with a pump to the target organ. In PPN, however, the cuticle is tougher, making penetration difficult. Furthermore, even if the needle is successfully injected through the cuticle, high internal pressure of the nematode makes release of the cargo practically impossible (personal communication). Together, this means another route for delivery of exogenous molecules is required. The established RNAi method in PPN relies on soaking of dsRNA to the nematode and the uptake thereof.

In other nematode species, transfection using liposomes increases the efficiency of delivery and spread of nucleic acids ¹⁷⁸. Liposomes are lipid bilayer structures that can carry molecules such as DNA ²⁴⁴ and RNA ¹⁷⁸ to cells by fusing the liposome with the cell membrane or through endocytosis. Transfection of mRNA is often desired over other genetic molecules due to its reliable nature and consistent expression kinetics ^{245–247}. Furthermore, it does not require nuclear localisation nor knowledge of promoters, terminators, etc. ^{248,249}.

3.3.1.1 *Expression of mRNA encoding for fluorescent proteins*

To investigate if transient expression could be achieved in PPN using a liposome-based method, two mRNAs encoding for different fluorescent proteins were packaged in liposomes. Screening for delivery of mRNA into the cell was done via detection of the protein as a proxy, with the motivation that a single molecule of mRNA could be translated into multiple copies of protein, resulting in amplification of the signal. Nematodes were soaked in the solution, and octopamine was added to facilitate uptake. After 24 hours, nematodes were imaged by confocal microscopy (Figure 3.1 A).

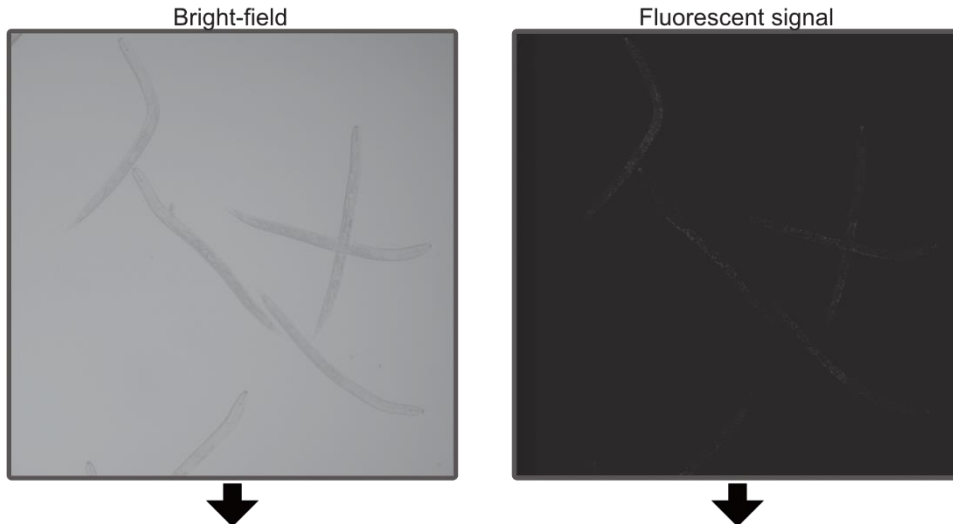
As a negative control, a mRNA encoding for a fluorophore in another emission spectrum was used. This negative control was chosen over the exclusion of any mRNA. If an increase in fluorescence was observed over a negative control without mRNA, then this could either be a product of the expression of eGFP or due to the act of transfecting mRNA (any mRNA might increase fluorescence). To eliminate the later possibility, mRNA is included in the negative control for a fluorophore outside the expected emission spectrum. Therefore, an increase in fluorescence in the eGFP spectrum is most likely a result of expression of eGFP, and not a result of the presence of mRNA.

Nematodes soaked with eGFP mRNA are brighter in signal than the negative control. However, *H. schachtii* has high levels of autofluorescence in the GFP spectrum (throughout, but predominantly in the intestine), complicating the assessment. To obtain a measurable metric, a computer algorithm was used to determine the intensity value of a pixel¹⁴⁶. A pixel is only counted if it is above an empirically derived intensity threshold. The threshold is set such that the background fluorescence (i.e., outside the nematode) is not counted. The expression of the fluorophore should increase the level of fluorescence above the background autofluorescence.

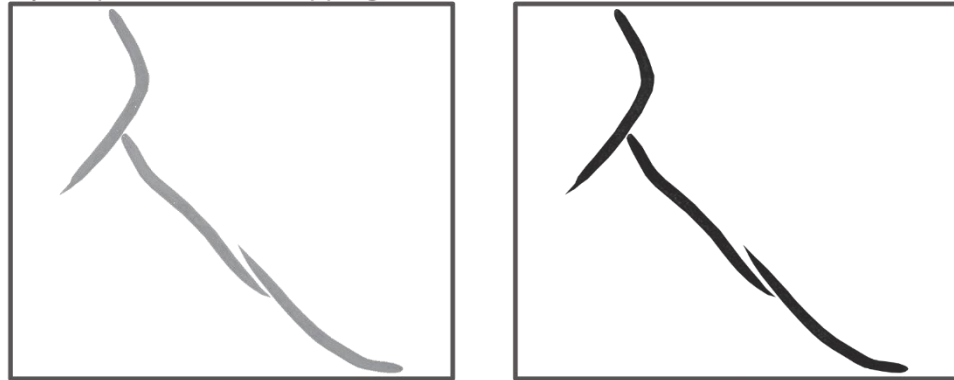
Before applying the threshold, nematodes were cropped from confocal images using the pen tool in Adobe Photoshop 2020 (Figure 3.1 B). The fluorescent channel is cropped out and placed, for both the positive and the negative in the same document. For clarity, the signal was inverted, brightness and contrast are adjusted, equally over the two conditions. From these images, pixels are assessed and quantified (Figure 3.1 C).

Pixels above the empirical threshold are labelled for localisation purposes (Figure 3.1 C). There is a clear difference in both fluorescence intensity and localisation between the control and the treatment. On average, nematodes soaked with mRNA encoding for eGFP were 3.9 times brighter than the control at 476 nm emission ($n = 21$ and 22 , respectively, Mann–Whitney U $P = 5.703e^{-11}$) (Figure 3.2 A). None of the above observations occurred using mRNA encoding for the fluorophore mCherry in its respective fluorescent range (data not shown).

A) Raw confocal images as input pipeline



B) Crop out non-overlapping nematodes



C) Invert fluorescent signal, increase contrast, quantify, and label

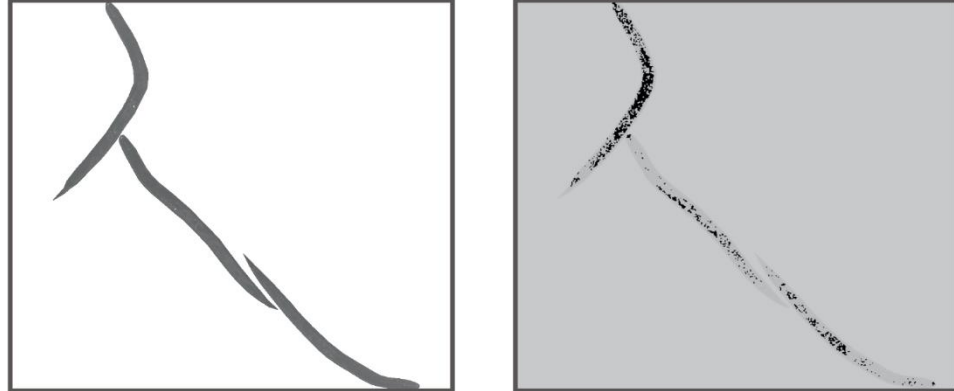


Figure 3.1: Pre-processing of confocal images for automatic fluorescence quantification and localisation. On the left a Leica PMT Trans image (similar to brightfield), and on the right the fluorescent image in gray scale. Step A) Images of nematodes are captured on a Leica SP5 confocal microscope. B) From the resulting 500x500 px images, non-overlapping nematodes are manually cropped out using the pen tool in Adobe Photoshop 2020. Both the treatment and control are positioned into the same photoshop document, and brightness and contrast are adjusted equally for all nematodes. C) A computer script is used to determine if a pixel meets a threshold requirement. The pixel is then counted, and an overlay is presented onto the image via a black pixel. The quantification is automatically saved to a notepad document. The localisation of fluorescence can be saved with a screen capture.

Various lipofection reagents available on the market are optimised for delivery of different molecules. To illustrate the effect of the transfection reagent, and subsequently find the best one in the range, CRISPRMAX (optimised for Cas-9 protein delivery), MESSENGERMAX (optimised for delivery of mRNA) and RNAIMAX (optimised for dsRNA delivery) were compared for delivery of eGFP encoding mRNA. Both MessengerMAX (n = 49, Mann–Whitney U P = 0.004996) and RNAIMAX (n = 32, Mann–Whitney U P = 0.03084) outperformed CRISPRMAX (n = 30) in overall fluorescence (Figure 3.2 B).

Comparing fluorescent encoding mRNA, and delivery reagents

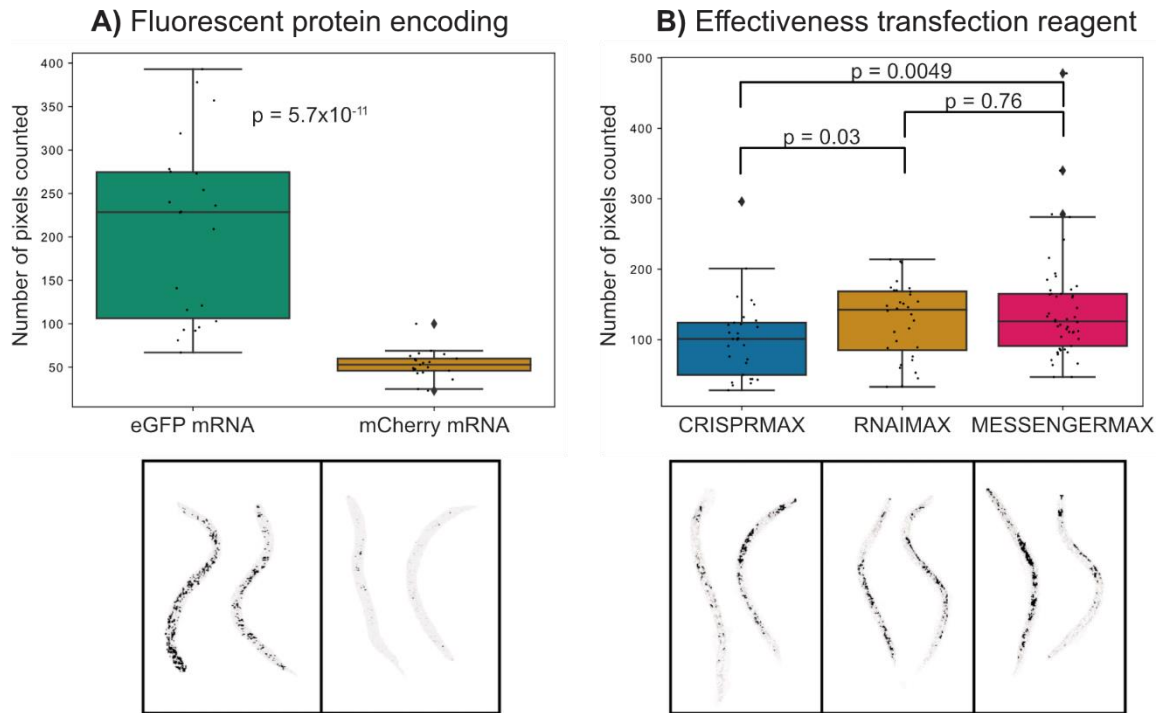


Figure 3.2: Expression of eGFP encoding mRNA in the plant parasitic nematode *Heterodera schachtii*. A) mRNA encoding for eGFP and mCherry were soaked in liposomes with J2 nematodes for 24 hours. The nematodes are imaged with confocal microscopy (ex 476 nm, emission capture 508–513 nm). From the resulting images fluorescence is quantified via a computer script. The quantified pixels are shown in the graph for both treatments, and their localisation is indicated with black pixels on the representative images below. The significance between the groups was assessed with a Mann–Whitney U test ($n = 21$ and 22 , $P = 5.703e^{-11}$). B) Side by side comparison of three different lipofection reagents, CRISPRMAX, RNAIMAX and MESSENGERMAX. The significance between the groups was assessed using a Mann–Whitney U test. Comparing to CRISPRMAX: ($n = 49$, $p = 0.004996$) and RNAIMAX ($n = 32$, $p = 0.03084$).

3.3.1.2 Expression of mRNA encoding for luminescent enabling enzymes

3.3.1.2.1 OPTIMISING THE DETECTION OF BIOLUMINESCENCE

Autofluorescence makes detection of a desired fluorophore time consuming due to the need of manual processing of the images, as described above. A method of detecting mRNA expression not relying on fluorescence is desirable. Luciferase is an oxidative enzyme, commonly used as a reporter. The enzyme produces light by oxidation of luciferin, referred to as bioluminescence *in vivo*, or chemiluminescence *in vitro*.

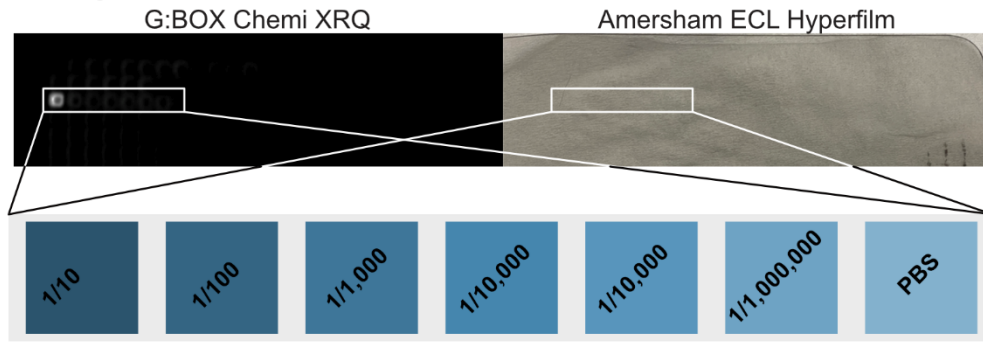
Various techniques were tested to find the optimal detection method for the experimental setup. A cell-free luciferase protein was used to compare three detection methods before proceeding to the mRNA soaking trials. The tested methods were: G:BOX Chemi XRQ (light sensitive camera), Amersham ELC Hyperfilm (Panchromatic black-and-white photographic paper) and the CLARIOstar Plus plate reader (photomultiplier tube amplified detector).

The first two methods are predominantly used where localisation of the chemiluminescent signal is crucial, like western blot detection. In Figure 3.3 A, both localised methods are compared side by side. A dilution series of luciferase (100 mM (1x) - 0.0001 mM (1/1,000,000x)) was added to a standard of luciferin. The chemiluminescent signal for 1:10 is only observed using the G:BOX Chemi XRQ, the same dilution is not observed on the Amersham ELC Hyperfilm.

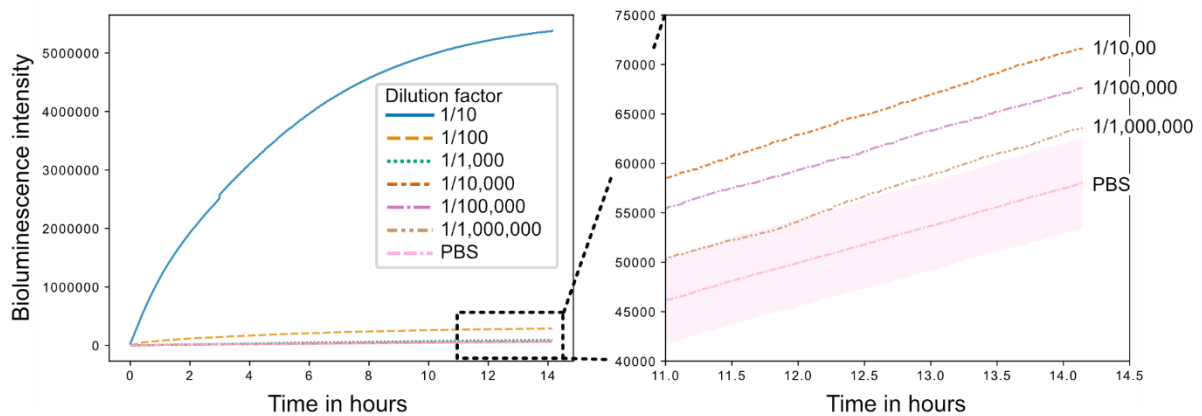
The localised methods are severely limited in sensitivity. A common technique to amplify lower intensity signals is through photomultiplier tubes (PMTs). These vacuum phototubes can increase the current produced as a result of light 100 million times, with detection essentially being limited to a single photon. The CLARIOstar plate reader uses PMTs for signal detection. A range of different gain (sensitivity of detector) settings was explored. In Figure 3.3 B, the cumulative luminescence for different dilutions series is plotted over time (hours). When signal is plotted cumulatively, the CLARIOstar plate reader can distinguish the 1/1,000,000 dilution using a maximum gain of 4095 after about 11 hours. From these three methods, the plate reader is most sensitive for chemiluminescence detection.

A too high density in nematodes may reduce the number of photons reaching the detector. A range of nematode densities were tested for its impact in detection of luciferase activity, the concentration of luminescence producing components remained the same. As shown in Figure 3.3 C, density starts to interfere with the signal > 2,500 nematodes per well.

A) Discovering detection limit localisation methods



B) Light detection for concentration of luciferase



C) Effect of nematode density on light detection

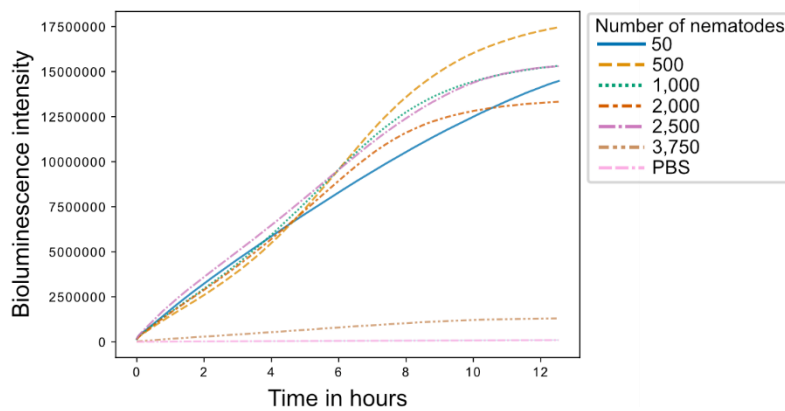


Figure 3.3: Detection of bioluminescence using various techniques. A) localised methods show both the intensity and location where luminescence originated from. On the left, a photo-sensitive camera was used. On the right a photo-sensitive film was used. Both techniques were exposed to a luciferase dilution assay for multiple hours. B) Using the same dilution series, lower concentrations of luciferase can be detected using a plate reader. After about 11 hours, the plate reader has detected enough photons to differentiate the background signal from the lowest dilution in the series. C) Photons need to reach the PMT in the plate reader for the detector to sense a signal. Nematodes start to interfere with the light path at a density >2,500.

3.3.1.2.2 DETECTION OF LUCIFERASE mRNA IN LIVE NEMATODES

The plate reader allows for rapid analysis of many samples as it does not require any manual post-processing of the data. Now that the protocol is optimised, the detection of mRNA encoding luciferase *in vivo* can be tested. To produce light, three components need to be present: 1) Luciferin; 2) Adenosine triphosphate (ATP); and 3) O₂. For this experiment, we assume cells in *H. schachtii* have adequate oxygen and ATP available for luciferase to oxidise luciferin. The mRNA was encapsulated in RNAiMAX lipofectamine and 20,000 *H. schachtii* J2s were soaked in the mixture, the negative control was soaked excluding any mRNA. After 24 hours, the nematodes were split over eight wells (< 2,500 nematodes per well), luciferin was added, and light was measured for multiple days.

Luminescence in wells containing nematodes soaked in liposomes containing mRNA encoding luciferase was, on average, higher than the negative control (Figure 3.4). The signal decreases over time and is most likely the result of degradation of the substrate. The average distance between the two conditions declines over time, and signals merge >20 hours after addition of luciferin, indicating either the substrate or the enzyme had depleted. The decrease in luminescent signal as a function of time can be compared between the two treatments as a scorable parameter using Mann–Whitney U test for unpaired data (p-value < 0.001).

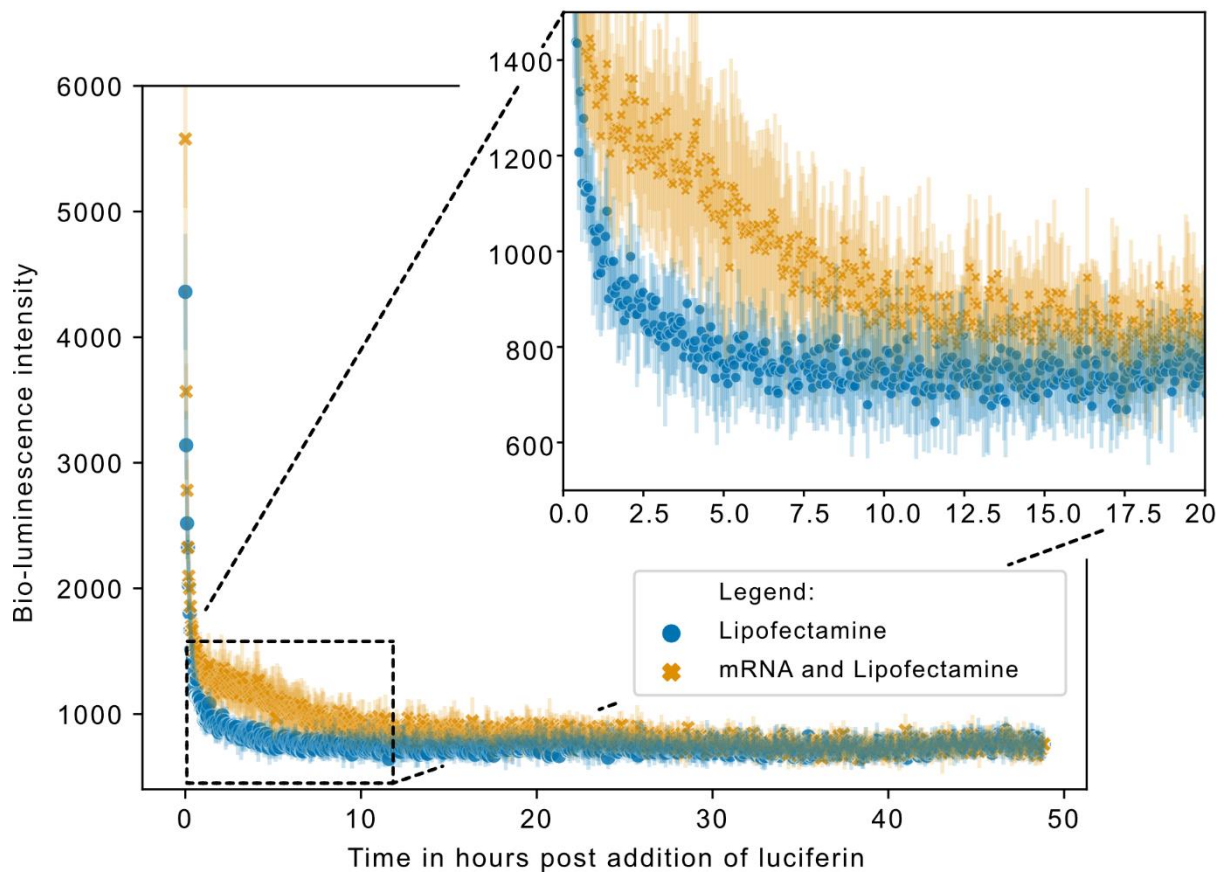


Figure 3.4: Detection of expressed luciferase from mRNA in the plant parasitic nematode *Heterodera schachtii*. Both signals start high, likely an artifact of the high gain setting or scattering of the light. The treatment signal remains visually separated until about 20 hours. The decrease in signal can be described as a function of time for every replicate. The decrease was compared (half-life time) with a Mann–Whitney U test ($p = 8.0e^{-4}$).

3.3.2 Genome editing in plant-parasitic nematodes.

3.3.2.1 Identifying a target gene

There have been no successful genome editing experiments performed on any plant-parasitic nematode. The first edit is a challenge because we know from other systems that some genes are easily editable, and others are not. Without a precedent, it is impossible to know which gene is which. Existing literature in other nematodes was used to prioritise target genes as best as possible. It is also known that some modifications to genes can produce scorable dominant phenotypes^{167,179} which may facilitate detection.

A conserved pattern of mutations in orthologous cuticular collagens produces a dominant rolling phenotype in *C. elegans*, and *P. pacificus* (*SQT-1* and *ROL-6*)^{167,250,251}. Given how universal these mutations and phenotypes appear to be, generating this genotype in plant-parasitic nematodes may produce similar phenotypes. To identify homologues of *SQT-1* and *ROL-6* in *H. schachtii*, a reference sequence is obtained from public resources (e.g., Genbank, publications).

These 'queries', are aligned to the *H. schachtii* transcriptome (at the time internal, now published⁶⁸) using a Basic Local Alignment Search Tool (BLAST). Sequences returned with the highest similarity will have the lowest E-value. The deduced amino acid sequence of these *H. schachtii* transcripts were aligned with the *C. elegans* and *P. pacificus* *SQT-1* and *ROL-6* peptide sequences. A phylogenetic tree was inferred from this alignment to identify the closest putative orthologues (Figure 3.5 A).

The *H. schachtii* transcripts TRINNITY_DN_14852, TRINNITY_DN_18898, TRINNITY_DN_33246, and TRINNITY_DN_33248, are grouped in a clade with *P. pacificus* *SQT-1* (PDM81196.1) and *C. elegans* *SQT-1* (NP_496421.1). From the three non-*H. schachtii* genes, *C. elegans* *ROL-6* (NP_495858.1) was the most distant sequence in the clade. Given that the *H. schachtii* putative *SQT-1* sequences are most sequence similar, the focus was directed to *SQT-1*.

Alignment of the *H. schachtii* *SQT-1* homologs revealed that transcripts TRINNITY_DN_14852 and TRINNITY_DN_18898 encoded identical protein sequences (data not shown). The same is true for TRINNITY_DN_33246 and TRINNITY_DN_33248 (data not shown). Duplicates were discarded, and only TRINNITY_DN_14852 and TRINNITY_DN_33246 were analysed further. To determine which of the remaining *H. schachtii* *SQT-1* homologues to target, the amino acid sequences of TRINNITY_DN_14852 and TRINNITY_DN_33246 were aligned to the region of the *P. pacificus* *SQT-1*. The third Arginine in the *P. pacificus* *SQT-1* motif, when mutated from a *RVRRQ* to *RVRCQ*, produces a rolling phenotype²⁵². The corresponding

positions in TRINNITY_DN_14852 (RARRD) and adjacent sequences were more similar than TRINNITY_DN_33246 (Figure 3.5 B-1). The sequence TRINNITY_DN_14852 was therefore characterised as an SQT-1-like putative ortholog.

The physical accessibility for editing machinery to a DNA region of interest is crucial in modifying a gene. In eukaryotes, gene expression is partially regulated by the wrapping of DNA around histones packed in nucleosomes²⁵³. Recent studies indicate that chromatin state can influence CRISPR Cas9 binding ability by restricting the accessibility to the DNA^{254–259}. Relative expression data were used as a prediction of the accessibility of a gene. This data was available internally and is now published⁶⁸. For the *H. schachtii* putative SQT-1, the relative expression in J2 was not the highest of all the life stages (6.16 ± 0.88), compared to the highest life stage (23150.80 ± 1274.36). Since there is some level of expression, and obtaining J2s is less time consuming and technically challenging, we continued the experimentation on the infective life stage.

3.3.2.2 Cloning and CRISPR experimental design

The genes of interest were cloned from gDNA and cDNA before CRISPR/Cas9 gRNA design and sequenced using the Sanger sequencing service provided by Genewiz. For the CRISPR experiments, two overlapping, antiparallel guide RNAs were designed to target the Cas9 endonuclease to the same locus for increased efficiency ²⁶¹. A single-stranded donor DNA fragment was designed to have homology arms with the genomic sequence of ~50bp on either side of the intended modification (to allow for homology directed repair) and encoded the mutated bases (RARCD as opposed to wild type sequence RARRD) as shown in Figure 3.5 B-2.

3.3.2.3 Delivery of CRISPR reagents to *H. schachtii*

3.3.2.3.1 Transfection of *H. schachtii* J2 with CRISPR solution

Through lipofection and a soaking based method, mRNA can be expressed in PPN. Ultimately, this technique may be used for genome editing facilitated through e.g., CRISPR/Cas9. However, there may not be any need to express exogenous genes. In a recent study a protein-gRNA complex of CRISPR-Cas9 was directly delivered via lipofection ²⁶². In this experiment, we test the viability of the soaking based method for delivery of functional protein via lipofection in somatic cells of *H. schachtii* J2s, and screen for both resulting repair pathways, homology directed repair (HDR) and/or non-homologous end joining (NHEJ).

All CRISPR components (protein, gRNA, ssDNA) were packaged into liposomes, and worms were soaked in the solution with the addition of octopamine ^{243,261} for eight hours. Soaking CRISPR reagents targeting HDR of the identified genes above did not produce any scorable phenotype. There is currently no confirmed distinct phenotype associated with a DNA mutation in *H. schachtii*. Furthermore, mutating similar motifs in putative orthologues may not result in an identical phenotype between species. To confirm if a mutation had occurred, DNA was extracted from the soaked nematodes, treated with exonuclease I, and amplified around the mutation regions via PCR and sequenced using Illumina technology. Three conditions were tested: 1) treatment with all CRIPSR components; 2) a treatment omitting the correct gRNAs; and 3) untreated nematodes. In all samples, the base pair changes exist; however, this is not expected in the untreated condition, which may have been contributed by a PCR induced error (Table 3.3). The frequency is higher for the samples where ssDNA is added. The reads in untreated could indicate the natural presence of the mutation in the tested population. Therefore, TRINNITY_DN_14852 is not further investigated. To understand why an increase is observed even with correct gRNAs omitted (false positive), further investigation was required.

Table 3.3: The number of observed nucleic acid changes compared to the reference genome for two different base pair locations based on the donor fragment.

	Base 202 (C>T)	Base 204 (T>C)
A (Correct gRNAs)	39.2%	39.1%
B (Incorrect gRNAs)	23.6%	23.5%
C (Untreated)	7.0%	7.0%

An experiment was conducted to investigate the origin of these false positive amplifications. Here we investigate if PCR can cross-amplify across two DNA fragments (template switching, Figure 3.6 A) by comparing three conditions added to *H. schachtii* J2: 1) CRISPR protein, correct guide RNAs and the donor fragment; 2) the same as the first, but guide RNAs targeting another gene (CRISPR event control); and 3) a negative water control.

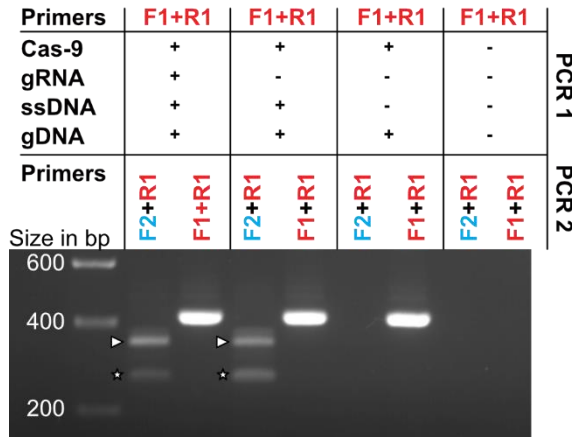
For this test a single ssDNA fragment containing an amino acid mutation targeting *H. schachtii* FAR-1 were encapsulated in CRISPRMAX lipofectamine. The complexes were delivered through the above described *in vitro* soaking methods. Two negative controls were used omitting: 1) gRNA(s); and 2) all CRISPR components. Post treatment, DNA was extracted from a pool of 20,000 J2s, ssDNA was digested, and 429 bp flanking regions of the target site were amplified by nested PCR (Figure 3.6 B).

In PCR 1: Primers were used that flank the homology region of the ssDNA. The product was used in the subsequent PCR 2. Here we re-amplify using the original primer set, and a set where the forward primer binds the mutation site, and the reverse primer binds flanking the homology region of the ssDNA (Figure 3.6 A). In both treatments with ssDNA, the PCR reaction yields a product regardless of the presence of gRNA, suggesting template switching (Figure 3.6 B). Based on NGS sequencing of the PCR product of the primers flanking the homology region from the second nested PCR, almost 30 % of the reads returned are a result of template switching between the gDNA and ssDNA (Figure 3.6 C).

A) Schematic of example of CRISPR experiment components and PCR



B) Template switching *in vitro*



C) NGS analyses of frequency edit

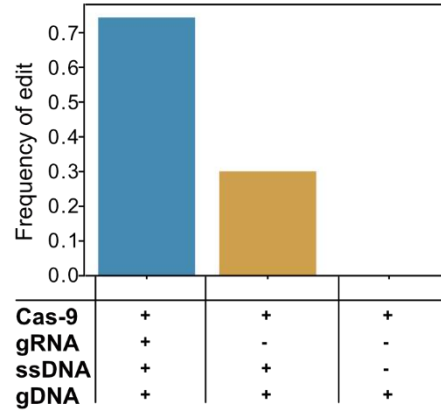


Figure 3.6: Identifying template switching using nested PCR. A) A schematic overview of the binding location of each primer, and the resulting fragment size. Flanking primers F1+R2 produce a product of 429 bp, where the same reverse primer with edit-binding primer F2 produces a product of 347 bp. B) The nested PCR. Four different combinations of reagents are tested. The first contains all the required CRISPR components for HDR. The second omits the gRNA, preventing targeted mutagenesis of Cas9. The third omits both the gRNA and ssDNA, preventing potential template switching. The last reaction lacks all components and is used as a negative control. All the combinations are first treated with exonuclease I, removing most of the ssDNA. A PCR is performed on this product with the flanking primers. The DNA is cleaned up and used in the second PCR. Here we amplify the template again with flanking primers, and the edit-binding primer combination. Both reactions with ssDNA, regardless of the presence of gRNA, amplify 347 bp fragments (arrow). Unspecific amplification of a smaller fragment is also observed (star). C) Visual representation of frequency of edited reads in the second nested PCR using the flanking primers. Almost 30 % of the reads are a product of template switching.

3.3.2.3.2 Challenges associated with lipofection-based delivery of CRISPR-Cas components to second stage juvenile *H. schachtii*

In all conditions containing ssDNA, the unique sequence to the donor was present, even in the negative control lacking gRNAs, minimising the possibility of integration through HDR. The introduction of the non-genomic sequence most likely occurred during PCR amplification via template switching, of which we confirmed the activity *in vitro* via a three primer nested PCR (Figure 3.6 B-C).

The following experiments focusses, therefore, on NHEJ, as the presence of ssDNA in HDR complicates the assessment through sequencing. At the time of the experiment, there was relatively little known about sub-optimal motifs in gRNA design. It was decided that for highest chance of success a range of targets that are highly expressed (likely accessible to CRISPR components^{254–259}) would be tested. In each case, multiple modified and un-modified gRNAs targeting the same area were designed. A total of 24 gRNAs were designed targeting eight genes (1-4 gRNA(s) per gene Table 3.1). The gRNAs for half of the genes were modified to increase endonuclease efficiency (2'-O-Methyl at first 3 and last bases, 3'phosphorothiate bonds between first 3 and last 2 bases, Synthego). The remainder of genes was targeted with unmodified gRNAs. For every target gene, primers flanking the target site were designed to amplify a 300-500 bp fragment (Table 3.1). Liposomes of RNAiMAX and CRISPRMAX containing ribonucleoprotein complexes were assembled and delivered to J2s using the soaking based method for every target gene. After 24 hours, DNA was extracted, amplified by PCR, and sequenced using 250 bp paired end Illumina sequencing.

Using a custom script, the frequency of indels and substitutions within the target region for every gRNA (1-6 bp upstream of the protospacer adjacent motif) was quantified. Overall, there are few reads containing indels and/or substitutions within the PAM regions. The only consistency observed between the treatments is for Gene 25230, which has consistently higher edited reads for both indels and base pair changes in the target region on the negative control (Figure 3.7 and Figure 3.8). For all the other guides and genes, no such pattern is observed. Taken together, the results show no convincing indication of genome editing through CRISPR/Cas9 complex soaking.

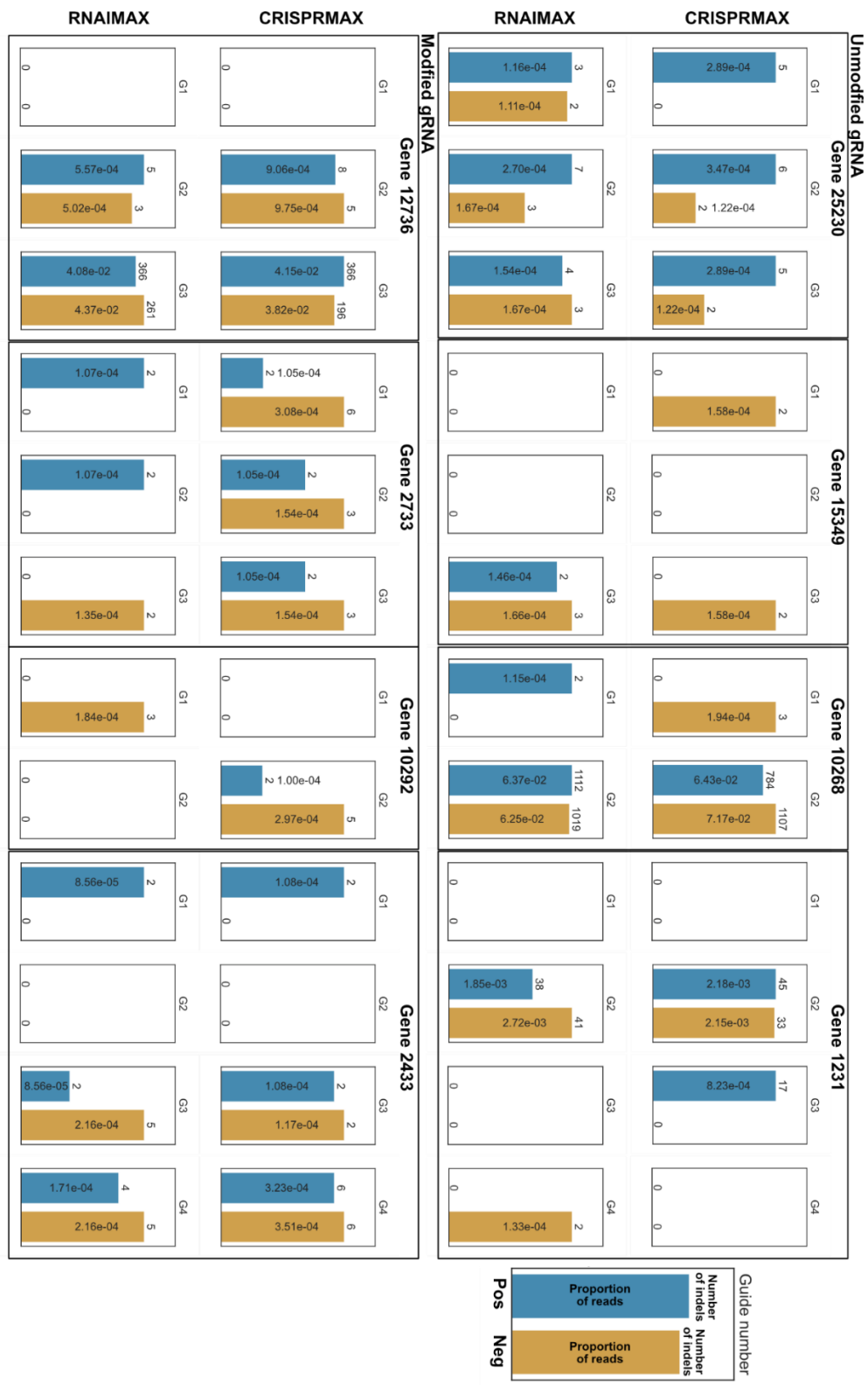


Figure 3.7: The frequency of insertions and deletions in the total number of reads is shown of the y-axis for every graph. In blue are the results for treatments with gRNAs, in orange are omitted from gRNAs. On the top of every bar, the number of reads is shown. Inside the bar, counterclockwise rotated the proportion of reads is indicated with scientific notation. If the bar graph was too small for the text, the notation is moved to above the read number. For any read count of zero, no proportion is given. Those soaked with unmodified sgRNAs (top) and modified sgRNAs (bottom) are shown. A variable number of gRNAs are used per gene, labelled as G(x) above the bar.

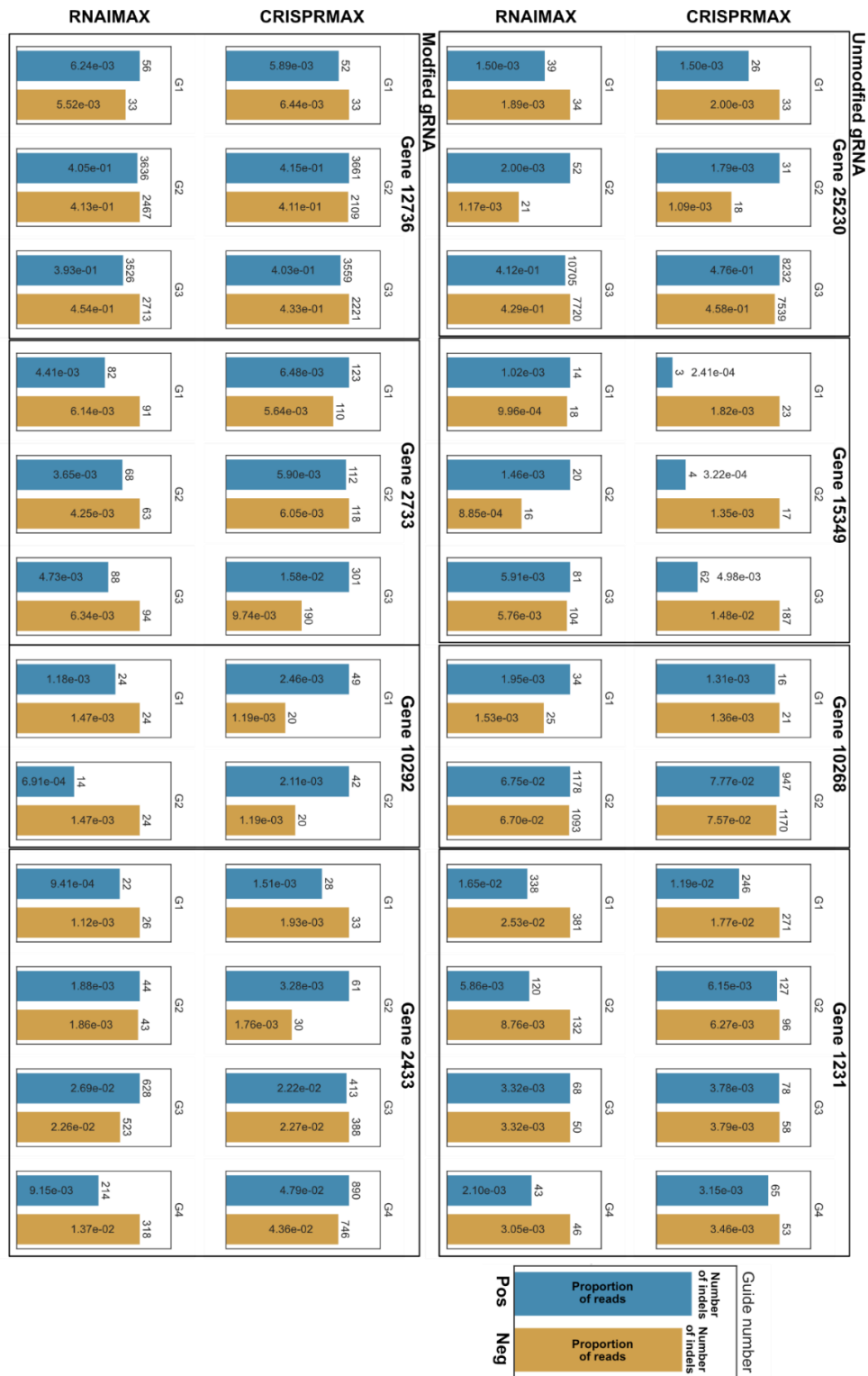


Figure 3.8: Next generation sequencing results. The frequency of base pair changes in the total number of reads is shown of the y-axis for every graph. In blue are the results for treatments with gRNAs, in orange are omitted from gRNAs. On the top of every bar, the number of reads is shown. Inside the bar, counterclockwise rotated the proportion of reads is indicated with scientific notation. If the bar graph was too small for the text, the notation is moved to above the read number. For any read count of zero, no proportion is given. Those soaked with unmodified sgRNAs (top) and modified sgRNAs (bottom) are shown. A variable number of gRNAs are used per gene, labelled as G(x) above the bar.

3.4 Discussion

The field of plant parasitic nematology is held back by the lack of functional genetic tools ¹⁴⁶. For the past 20 years, RNA interference has been the only tool available to researchers for reverse genetics in plant parasitic nematodes (PPN) ²⁶³. To expand the genetic toolbox, we aimed to develop methods for transgene expression and genetic modification.

3.4.1 Expression and detection of transgenes

In this manuscript we assess the viability to use lipofection as a mode for delivery of mRNA encoding for reporter genes. For the first time, we can express the exogenous genes, eGFP (*Aequorea victoria*, modified) and luciferase (*Photinus pyralis*) in the plant parasitic nematode *H. schachtii* through liposome mediated transfection. Both proteins require state of the art machinery to be detected, likely, due to low levels of expression.

3.4.1.1 Detection of fluorescent proteins

Confocal microscopy was used for detection of eGFP. One of the major challenges of confocal microscopy of plant-parasitic nematodes is autofluorescence, which is predominantly localised in the gut. For PPN, autofluorescence is lowest in the red spectrum, and high in the green spectrum ¹⁴⁶. Modern confocal microscopy techniques like fluorescence lifetime imaging microscopy (FLIM) and Förster resonance energy transfer (FRET) can separate fluorescent signal by analysing the time a fluorophore remains in an excited state before emitting a photon and measuring the lifetime changes of a particular fluorophore ^{264,265}. Without these tools, detection can only be achieved via quantification of increased fluorescence.

Transfection of nematodes with mRNA encoding for eGFP with lipofectamine RNAiMAX and MESSENGERMAX increased the overall intensity and localisation of fluorescent signal. A computer program is required for accurate quantification of increased fluorescence due to the small increase. Using the lipofectamine reagent CRISPRMAX, no increased fluorescence was observed. This likely means that for successful transfection a lipofection reagent is required that is optimised for the delivery of RNA. Given the similarity in performance of both MESSENGERMAX (optimised for delivery of mRNA) and RNAiMAX (optimised for delivery of dsRNA) suggests minor differences between the two reagents. The low increase in fluorescence may be explained by limited delivery of mRNA into the cell and may be directly linked to inefficient delivery of the exogenous molecules through liposomes.

The first development of liposomes started in 1965 ²⁶⁶. More than 10 years later, the technique was used for the first time to deliver mRNA ²⁶⁷. Another decade later, massive efficiency improvements were achieved using cationic lipid nano particles ²⁶⁸. Liposome mediated transfection is now used and trailed today in vaccines for influenza ²⁶⁹, cancer

immunotherapies²⁷⁰, protein replacement therapies²⁷¹, and most recently COVID-19 vaccines²⁷². Over the years, efficiency in delivery of mRNA using this technique has increased, it is expected that in the future liposome mediated delivery may further increase and therefore allow for higher expression of mRNA in PPN.

A similar increase in fluorescence was not observed with transfection of mRNA encoding for mCherry. This fluorescent protein emits about 2x less photons than eGFP^{273,274}, which may cause the intensity to be below our detection limit. Another explanation could be codon incompatibility of the mRNA with *H. schachtii*²⁷⁵. There is no information about the genetic sequence from the mRNA, as it is held as proprietary by Ozbiosciences. Future experimentation could focus on the codon optimisation of mRNA encoding for luciferase using the codon usage bias of the top highly expressed genes in *H. schachtii*⁶⁸. Furthermore, base pair modifications such as N6-adenosine methylation which can promote translation²⁷⁶, and combining these with a range of untranslated regions (UTRs) which play a role in the regulation of translation²⁷⁷, may increase the efficiency in expression to a detectable level. Lastly, detection may further be improved via condensing the signal through the attachment of a nuclear localisation signal²⁷⁸.

3.4.1.2 Detection of light-emitting enzymes

Low levels of protein expression may also be masked by higher intensities of autofluorescence. Therefore, a detection method that does not rely on fluorescence is attractive. When luciferin is oxidised by luciferase it emits light between 550-620 nm²⁷⁸. Three detection methods were trialled against a standard of luciferase. Chemiluminescent photo paper (Amersham Hyperfilm ECL) was not able to detect any luciferase activity. The photosensitive paper may not be sensitive to the ranges of luciferase, as it is similar to the wavelength of safelights (585 nm)²⁷⁹. The photosensitive camera on the G:BOX Chemi XRQ (Syngene) was only able to detect the highest concentration of luciferase tested. The last tested, CLARIOstar Plus plate reader (BMG Labtech) amplifies a signal through a photomultiplier tube (PMT) before reaching the detector. A PMT can detect single photons in wavelengths ranging from deep-UV to near-IR²⁸⁰. Cumulative visualisation of the data allows for separation of the weak luciferase signal over time, putting our detection limit below 1:1,000,000 dilutions of the standard.

In addition to a detection limit, the light path may interfere with detection of a signal. Imaging through more than 3,750 nematodes has a noticeable impact on the detected light. Any lower tested densities did not have the same effect. Based on these results, plate reader with no more than 2,500 nematodes per well would be most appropriate for detection of luciferase activity.

Detection was performed *in vivo*, via direct addition of membrane permeable luciferin ²⁸¹ to nematodes treated with luciferase encoding mRNA in RNAiMAX. The first reads in both the positive and negative start high. These are either artifacts or scattering of light from other wells introducing false positives. For this reason, the samples <1,000 seconds are ignored in the analysis. Over time, both signal decrease in intensity, but the negative decreases faster than the positive. This decrease over time is taken as a quantitative measure of decay of the signal and is significantly longer for nematodes soaked with luciferase mRNA.

From the plate reader experiment it is clear luciferase is expressed in PPN, however, the expression based on detection remains low. The current experimental setup could be a limitation to detection of luciferin oxidative bioluminescence. Luciferase requires ATP and oxygen to perform its enzymatic reaction ²⁸². The well of the plate is sealed using a plastic cover to prevent evaporation of the soaking reaction, but it also limits gas exchange. This could, over the course of the experiment, lead to the asphyxiation of the nematode, limiting oxygen and ATP availability. Gas permeable membranes may be used to overcome this potential problem.

Luciferase rate of reaction may be limited by temperature. The most often reported optimum temperature for firefly luciferase is 25 °C (ranging 20-28 °C) ²⁸³⁻²⁸⁶. The plate reader is kept at a constant temperature of 21 °C, which is below the optimum enzyme temperature. *Heterodera schachtii* can infect hosts optimally in a range between 20.5 and 27.8 °C ²⁸⁷, meaning a higher more optimal temperature for the assay is achievable.

Lastly, the current detection method does not allow for localisation of the expression as with the detection of fluorescent proteins. This limitation of the plate reader may be overcome in the future by setting the emission limits of a detector to 550-620 nm on a confocal microscope, without enabling the laser ²⁸⁸⁻²⁹⁰. Confocal microscopy uses PMTs to amplify the signal, making it similarly sensitive to a plate reader.

3.4.1.3 Current limitation of expression

Detection through a PMT (either confocal, or a plate reader) are one of the most sensitive methods for detecting photons. The main limiting factor in the current assay is efficiency of expression or delivery. Above we address some potential improvements for expression. For delivery, many parameters can be optimised: 1) Testing a range of lipofection reagents; 2) Soaking time; 3) Finding peak of expression (detection time); and 4) mRNA concentration.

Delivery of DNA may provide a more suitable alternative. In *C. elegans*, expression is routinely performed on plasmid DNA ¹⁵⁶. Inside the recipient cell, multiple copies of the DNA form large concatemers resulting in a structure called extrachromosomal arrays ¹⁶⁷. Expression of this

exogenous gene will typically stay for multiple generations ¹⁶⁷. Delivery of DNA is appealing because a single delivery event (1 molecule of DNA), could result in multiple molecules of mRNA essentially amplifying the resulting protein expression.

3.4.2 Genetic modification via CRISPR-cas9 protein transfection

The above-described method outlines the potential for delivery of genetic material to PPN through a cheap and accessible method. Expression of the mRNA, and/or the detection thereof remains prohibitive. A viable alternative to expression may be the direct delivery of proteins through lipofection ^{262,291}. Photon based detection methods will always give a summary of a signal (either number of scans per well for a plate reader, or resolution of an image on confocal). As an alternative, sequencing can be used, as its resolution is essentially limited to a single base-pair.

We performed a liposome based soaking method for delivery of CRISPR/Cas9 proteins to somatic cells of *H. schachtii* juveniles targeting both the homology directed repair (HDR) and non-homologous end joining (NHEJ) pathway. For both pathways, results are inconclusive. Detection of HDR through PCR is prohibited by template-switching. We focused on NHEJ events in a range of genes, for multiple modified and un-modified gRNAs, but were unable to detect consistency for modified reads between treatments.

Edit events are likely rare. For them to occur, a protein needs to get into the cell and the nucleus, induce a double stranded break, and trigger a repair pathway. Furthermore, the pathway needs to introduce a new variation in the sequence. If this happens it is likely only in a few cells, which can't be selectively amplified for via PCR as all events are independent and therefore are likely different in sequence. To our knowledge, there are no known dominant knockout phenotypes in PPN that results in a dominant scorable phenotype for use as a marker.

Like luciferase, *S. pyogenes* Cas9 (SpCas9) has an optimal temperature (37 °C). With protocol optimisation CRISPR efficiency may be increased to a detectable level in PPN, through heat-shock treatment ^{292,293}, or inducing 'open' chromatin states for increased accessibility to the genetic sequence of the endonuclease ^{294,295}. Finally, for a successful experiment: 1) all CRISPR components need to be delivered into the nucleus (aided by a nuclear localisation sequence, which was present for the experiments in this chapter); 2) The target gene needs to be accessible, and targetable by gRNAs; and 3) The detection method needs to be able to detect unknown, possible rare, sequence modifications. If any of these steps fail, so will detection of a successful experiment.

The mutagenesis induced by the repair mechanism is random. To be able to selectively amplify for edited events, the resulting sequence needs to be known. One such way is through the use of a donor fragment; however, we have shown in this chapter that this could result in false positives. Catalytically impaired CRISPR–Cas9 is unable to induce double stranded breaks, but can still target specific DNA sequences²⁹⁶. Fused with an adenosine deaminase, which converts adenine to inosine in approximately a five-nucleotide window, the ribonucleoprotein complex can be used to specifically convert bases within the target sequence²⁹⁶. This process also induces a nick in the opposite DNA strand, inducing a DNA repair mechanism that uses the edited strand as a template, thus resulting in a predictable DNA edit²⁹⁶. Since the resulting sequence is known, primers can be used to selectively amplify for the edited event. For example, a target wild type DNA sequence is ‘PAM...NNNAAAA’, which gets temporarily converted to ‘PAM...NNNIIII’ and repaired to ‘PAM...NNNGGGG’. The primer ‘...NNNCCC’ could be used to selectively amplify for the event. Importantly the last edited base is omitted from the primer to avoid PCR induced false positives.

3.5 Conclusion

This chapter describes the first steps in expanding the genetic toolbox for plant parasitic nematodes. Through the technically simple method of soaking, mRNA can be expressed in low amounts in the plant-parasitic nematode *H. schachtii*. Genome editing through CRISPR/Cas9 protein soaking using a similar method did either not result or was limited by detection of successful edit events. There is considerable scope for optimisation of expression through mRNA as discussed in previous sections. Once optimised, future studies may focus on expression of CRISPR/Cas9 proteins through mRNA.

4 Chapter four – Automating nematode phenotyping

4.1 Introduction

4.1.1 Nematode infection assays and their limitations

Cyst nematode parasitism is defined by the formation of a nematode specific feeding organ ²⁹⁷. It partially achieves the formation of this feeding site via the differential regulation of host gene expression ^{68,298–303}. A subset of re-regulated genes is important to nematode parasitism, and the absence of these genes (so called Susceptibility genes or “S” genes) has a negative impact on nematode parasitism ⁶⁹. On the other hand, the presence of certain genes (so called Resistance genes or “R” genes) can impair nematode parasitism by activating an immune response ^{65,304,305}. Identification of these genes is a major focus in the field because it has intuitive routes to impact.

The current method for identifying R genes and S genes is well established. The method compares infection of *H. schachtii* on *A. thaliana* knock-out mutants of a gene to a wild-type control, typically in a replicate of 10-30 per genotype. The number of successful infections (i.e., survival past 12 Days Post Infection (DPI)) is manually measured under a stereomicroscope ⁶⁹. Both males and females are scored as different parameters, however, due to their similarity, error/bias is common yet different between humans. These can be eliminated by scoring older females (~24 DPI). At this life stage females are much more pronounced, nullifying the biased in sex differentiation. However, at this time point, males have become migratory, complicating their quantification, thus eliminating the phenotype of male:female ratio from the assessment.

The main limitation to this assay is speed. In our hands, 90 replicates can be scored on a full working day (seven hours work – one hour break). An unbiased knockout screen of all estimated *A. thaliana* genes (~27,600 coding and 6,500 non-coding ^{306,307}), using the current assay with a replicate of 30, would take 11,366 working days to complete (~ 31 years). Screening of smaller libraries, such as the *A. thaliana* multiparent advanced generation inter-cross population ³⁰⁸, would take about 176 days to score (527 recombinant inbred lines). Manual phenotyping is a bottleneck in nematode resistance and susceptibility screening. In recent years, however, large scale, reliable, automated image analyses-based phenotyping in plant pathology has become increasingly viable ^{309–313}.

4.1.2 Advancements in computer vision

Traditionally, biologist use drawings and paintings to document species and their phenotypes. Features of the phenotypes, and variations within species are often curated manually. Today, in addition to the traditional methods, photography is used to accelerate digitalisation of

phenotypes. However, the increase in efficiency of digital data collection massively outpaces manual curation, introducing the need for alternative methods of classification.

The field of computer vision centres around techniques used to extract features and information from digital images. Various algorithms can be used to computationally define features in an image including but not limited to: edge detection ³¹⁴; object recognition; and object tracking ³¹⁵. Recent improvements in deep learning further improve the capabilities of object detection ^{316,317}. The field of plant biology is already making use of image analyses tools like Leaf-GP for measuring leaf growth ³¹⁸, phenoSEED for phenotyping seeds ³¹⁹, and AutoRoot for automatic phenotyping of roots ³²⁰. However, to utilise any computer vision tool an efficient method of collecting data is first required.

4.1.3 Low-cost computing and the Raspberry Pi

A Raspberry Pi is an affordable computer, characterised by its small footprint and various connectors on the board (Figure 4.1). The most up to date iteration at time of writing is the Raspberry Pi 4B and cost £55. The computer allows for integration with external components through general-purpose input/output (GPIO), has a camera serial interface for external cameras, and can be controlled via a graphical user interface.

Located on the 40-pin header are GPIO pins can be configured into two states, High (3.3 V) and Low (0 V). An external signal can be distinguished by the same pins between High (≥ 2.0 V) and Low (≤ 0.8 V) ³²¹. The header is used to send and receive signals between the Raspberry Pi and any external electronic components.

The Raspberry Pi houses in addition to GPIO, other ports for connecting specialised devices, like the Camera Serial Interface port. There are various camera modules available for the Raspberry Pi. Two types of cameras are supported. The most common and basic cameras are the Camera module, and the NoIR Camera module, with an 8-megapixel Sony IMX219 image sensor and a fixable lens. Compared to the standard Camera module, the NoIR is missing the infra-red filter, allowing the sensor to sense infrared light. The second type, the High-Quality Camera Module has an increased resolution of 12 MP and uses the Sony IMX477 sensor. Either a detachable 6 mm wide angle lens or a 16 mm telephoto lens can be mounted on the module. The wide-angle lens only has an adjustable focus, where the telephoto lens also has an adjustable aperture. The aperture is a hole that determines how much light can pass through and reach the camera sensor, this is denoted using the F-stop. The smaller the hole (the larger the F-stop), the less light can pass through, and the more objects are in focus (a large depth of field (DOF)). Larger holes (lower F-stops) let through more light but result in fewer objects in focus (small DOF). In addition to the native cameras, there are various third-

party modules available that can interact with the Raspberry Pi interface, which is further supported with the integration of Libcamera ³²².

Importantly, the above-mentioned interfaces can all be controlled simultaneously either via the Linux command line, or via the coding language Python. The flexibility makes the Raspberry Pi an ideal candidate platform for developing prototype machinery for image capture. Indeed, a Raspberry Pi based solution to measuring leaf surface area in a variety of environments, demonstrates this potential ³²³. In order to apply this low-cost hardware to the plant-nematode phenotyping problem requires engineering.

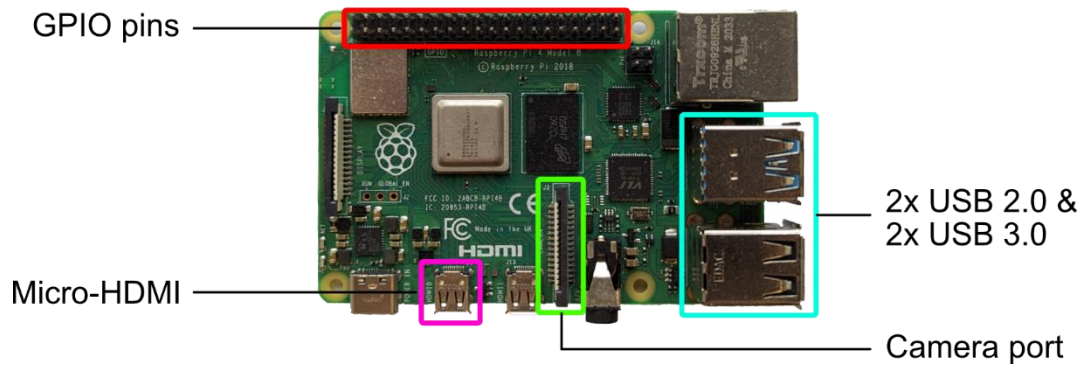


Figure 4.1: A Raspberry Pi 4B, and affordable small footprint computer. On the motherboard of the computer, various useful ports are found allowing for interaction with external hardware such as sensors. The most important for this project are marked. In red are labelled the GPIO pins. Most of these pins are used to send digital information between external electronics and the Raspberry Pi. In turquoise, 4x USB ports, allowing for expansion of storage, control via mouse and keyboard etc. Micro-HDMI in pink, allows for up to two 4K screens to be connected to the computer. And lastly, in green, the camera port, allowing for interaction with external camera boards, and image capture directly to the Raspberry Pi's internal storage.

4.1.4 Accessible 3D printing and design

A major bottleneck in product development is speed. Traditionally, production of an object was limited to subtractive manufacturing, involving cutting away material from a solid block to create a shape of interest. In 1986, Chuck Hull commercialised the first ever rapid prototyping technique, called stereolithography ³²⁴, which uses ultraviolet light to cure photopolymers one layer at a time, ultimately forming a 3D object. Importantly, this process is additive, removing the requirement of a block of starting material. In the mid-1980s, selective laser sintering was invented. A high-powered laser is used to fuse fine particles of powders into a 3-dimensional shape. Lastly, fused filament fabrication (FFF) was invented in 1988, and works by melting of a filament, building layer on layer to a 3D shape. The patent for FFF expired in 2009 ³²⁵ resulting in a 100-fold price drop for these types of printers. 3D printers are now extremely accessible, but require a custom digital design of the desired object.

A digital model of an object is created via extrusion of shapes using a computer-aided design software such as OpensCAD, SOLIDWORKS, Onshape and Fusion 360. For FFF printing the model must be converted to instructions for the printer, called G-code, using a slicer software (Cura, Creality, Chitubox). The object can then be printed in a range of materials like; nylon, polylactic acid (PLA), Acrylonitrile butadiene styrene (ABS), water-soluble Polyvinyl alcohol (PVA) and many more. These advancements in additive manufacturing allow for a rapid and flexible in-house prototyping workflow from design to product.

4.2 Aims

Manual labour is the main bottleneck in parasitism phenotyping. A solution may be found in the digitalisation of the assay, and the use of computer vision tools to automate quantification of parasitism. The highly versatile Raspberry Pi platform can be used to build specialised imaging equipment, made to capture components of the assay such as plant root and shoot, and parasitising nematodes.

4.2.1 Digitising the nematode parasitism assay

An important consideration in design is accessibility. It is important for tools to be usable and producible by people with no prior experience. However, electronics can impose a barrier of entry for some. Therefore, two versions of the imaging tower will need to be created; 1) a static manually operated imaging tower, and 2) a higher-tech semi-automatic imaging robot.

4.2.1.1 *Static imaging tower*

The imaging tower needs to be able to capture high quality images of the infection assay in axenic culture, and is: 1) affordable; 2) open source such that anyone can amend it for another purpose; 3) easy to build and operate so that a user with no prior experience in design or

electronics can use the device; and 4) capture nematode parasitism in high quality consistently.

4.2.1.2 Semi-automatic imaging robot

The above-mentioned static imaging tower requires a user to one-by-one place infected plants in axenic culture under a camera. Ideally, manual handling of plates is kept to a minimum.

To make a semi-automated robot scalable it is important that the machine can process petri-dishes for a given runtime without any user input. This will require hardware and electronics to communicate in such a way that the robot can: 1) hold many petri-dishes ready to be processed in a convenient format for the end user; 2) put a petri-dish one at a time under the imaging tower and trigger an imaging sequence; and 3) return the petri-dishes to a convenient format on a processed stack.

4.2.1.3 Normalising root surface area

Cyst nematodes are predominantly obligate root parasites. Their parasitism, amongst other factors, may be impacted by host morphology, such as root surface area. At time of writing, cyst nematode parasitism phenotyping does not account for phenotypic variation of the host.

Measuring root surface area manually is too time-consuming, therefore an automated method needs to be developed.

4.2.1.4 Counting nematodes from images

One major bottleneck in nematode phenotyping is counting of infection under the microscope. The technique requires expensive microscopy equipment, and time-consuming manual labour. Using the above-mentioned imaging towers we can digitise the infection assay. To be able to automatically process the digitised assay, a computer vision based method needs to be developed.

4.3 Materials and methods

4.3.1 Imaging of infection

Images of infection of *H. schachtii* on *A. thaliana* were collected via either a static imaging tower, or a semi-automated imaging robot.

4.3.1.1 Static imaging tower

The housing for imaging components was custom designed and 3D printed on a Ultimaker S3 printer. Files were sliced from STL format to GCODE using CURA (Ultimaker) with the following settings: infill: 20%, layer height: 0.15 mm, wall thickness: 1.2 mm with a printing speed of 40.0 mm/s. The printing bed temperature was set to 60 °C and the nozzle to 205 °C. The imaging tower was printed in two components. The main body was printed in PLA (Ultimaker) using an AA core (Ultimaker) and overhangs of more than 45 ° were supported with PVA (Ultimaker) in a BB core (Ultimaker). Both used cores were 0.4 mm in width. The support was dissolved in tap water via soaking for 24 hours at room temperature.

The 12 MP RPI-HQ-CAMERA (RASPBerry-PI) was directly mounted to the top part of the tower via M2 bolts (2 cm), nuts, and washers (RS components). For optics a 16 mm Telephoto Lens (RASPBerry-PI) was screwed onto the camera board. The camera module was connected to a Raspberry Pi 4B 8GB RAM via a 30 cm Ribbon Cable (THE PI HUT). Lighting was either provided via RGB 6400 K 12 V (V-TAC) for petri dishes containing food dye, and 4000 K white light LED strip 12 V (V-TAC).

4.3.1.2 Semi-automatic imaging tower

The same printing settings were used for printing the housing of the automated imaging machine, which was designed by Siyuan Wei and Sebastian Eves-van den Akker. The base of the machine was printed in Tough PLA (Ultimaker). The camera was mounted and connected to the Raspberry Pi using the same method as described above. A hall effect sensor (waveshare) was connected to the GPIO 23 (BCM). Permanent magnets (5 mm x 3 mm) (Deryun) were fixed into the holes on the indexing wheel, which was positioned such that when a magnet passes the hall effect sensor, the petri-dish was positioned under the camera. Detection of a magnet by the hall sensor set the value of the GPIO pin to HIGH. Once a high voltage was detected the relay connecting the motor and the relay connecting the LED switched to their Normally Open (NO) position. In parallel, the imaging sequence was triggered by starting the image capture command, 'raspistill -vf -hf -o %d.jpg -md 3 -dec -q 100 -ex spotlight -awb auto -ss 4000 -ag 1 -dg 1 -r -v -k'. The machine remained in this state until the image was fully written to the hard drive. After successful capture, the relays were reset to their original position. This process was repeated until either: 1) one of the proximity sensors

was triggered; 2) the user interrupted the script; or 3) the user interrupted the connection between the power source and the motor.

The Infrared Proximity Sensors (wavelshare) were mounted at the base of the feeding arm of the robot, and at the tail of the stacking arm. The default state at the base of the tower was HIGH, indicating there were still petri dishes in the tower, and the default state at the tail was LOW, indicating the arm wasn't full. Change in either of the sensor's states paused the machine. A flip switch connecting the motor and the power supply could also have been used to pause the machine.

Images were saved to SanDisk Extreme Pro USB flash drives 256 GB and converted from BMP to PNG using a custom Powershell script (Computer code 4.1, appendix). After conversion the same script copied the images three times independently to separate hard drives (Seagate 14 TB IronWolf Pro) using RoboCopy (Computer code 4.1, appendix).

The QR code was read from the images using a custom script, using partial code from Jie Zhou, Siyuan Wei, and Sebastian Eves-van den Akker (Computer code 4.2, appendix), for each copy separately. The information of the QR code was then included in the file name.

4.3.2 Infection assay of *H. schachtii* on *A. thaliana*.

Two infection trials were performed: 1) as described in chapter 2.3; and 2) as chapter 2.3, but with modified agar. The latter is described below.

To increase the contrast between female nematodes and the background, various food colouring (Limino, DYL-ghm-20210126-324) were added to the agar (Table 4.1). Two different concentrations were tested per colour. No dye was added to the agar for use in cyst quantification.

Two weeks post germination the roots were visualised using the static imaging tower. Quantification of infection was digitalised using the static imaging tower 21 days post inoculation for females, and 21+ days for encysted nematodes.

Table 4.1: Concentrations of used food dye in KNOP-medium. Amount of μL food colouring per 25 mL KNOP-medium. First column, name described by manufacturer (Limino). The second and third column describe the amount of dye used.

Colour	Dark ($\mu\text{L}/25\text{ mL}$)	Light ($\mu\text{L}/25\text{ mL}$)
Red	60	20
Orange	40	10
Lemon	30	10
Lime	70	5
Green	70	10
Teal	10	2.5
Blue	50	2.5
Navy	30	10
Grape	15	5
Black	60	20

4.3.2.1 *Ground truth by manual scoring*

The number of both male and female nematodes was quantified under a S9D Stereomicroscope (Leica). Size of females and cysts was determined from images taken using the static imaging tower as described above. Using the polygon selection tool in ImageJ, an outline was drawn around the nematode, and the total area in pixels was quantified using the measure function.

4.3.3 QR code automation

A Python script was made to rapidly generate QR codes and distribute them over an A4 page in rows and columns (Computer code 4.3, appendix). The layout was printed on Matt White Polyester Labels for Laser printers with marine permanent adhesive (BS5609), LP1/210 MWP (LabelPlanet). Manually using scissors, the QR codes were cut from the sheet, and applied to the bottom of the petri-dish. Each QR code contained information about a specific replicate like the target gene, T-DNA insertion identification number, date of inoculation, hatching jar number and replicate number.

4.3.4 Script-based counting and quantifiable traits

To quantify the number of nematodes, ImageJ scripts were used on the images taken using the methods described in the static imaging tower. A different script was used for counting cysts, and counting females. For females, the script was based on colour thresholding, which is sensitive to colour variation. The first script was used to isolate tanned cyst nematodes and the second script for quantifying female nematodes on coloured agar.

Script 1: Automated quantification of cyst nematode infection.

Using built-in ImageJ commands, the script sets a colour threshold for a brown (set by the user), converts the image to 8bit, removes outliers, watersheds the resulting mask, pauses while the user defines an area of interest, and analyses the resulting overlay.

Script 2: Semi-automatic quantification of females on coloured agar

Using MorphoLibJ ³²⁶, females were segmented from the background of the coloured agar, using both the segmentation threshold and the radius set to 5. Manual verification of the mask was performed using the catchment basin view. The size and number of nematodes was scored using the analyse regions function.

4.4 Results

Cyst nematode phenotyping is typically done via manual scoring of infection under the microscope. This technique has been the standard in the field for years and allows for accurate assessment of the susceptibility of the host. The technique, however, has some clear shortcomings: 1) it is labour intensive, limiting the throughput to about 90 plants per day (three genotypes, 30 replicates each). Importantly, nematode development is rapid. Therefore, spreading the phenotyping over multiple days would result in inaccurate assessment of infection; 2) it can be error prone. Nematodes are scored during their sex differentiation stage, during which it remains difficult to accurately distinguish some individuals; and 3) requirement of expensive laboratory equipment.

Labour is probably the highest barrier to high throughput forward genetic screens of nematode infection. There is to date no published alternative to nematode susceptibility screening that increases speed. For larger genetic screens the classical method would require an unmanageable amount of labour, essentially forcing research groups to narrow their focus to a small subset of potential candidates and/or timepoints.

In recent years, with the advancements in computer vision and machine learning methods, other fields have adopted image analyses-based solutions to automate phenotyping. An image-based nematode infection phenotyping platform that addresses the above-mentioned issues will be: 1) affordable and open source; 2) capture consistent images of nematode infection *in vitro*; 3) able to reliably count nematodes in an automated manner; and 4) increase the efficiency of screening.

4.4.1 The static device

A well-established axenic culture method to screen for susceptibility or resistance of the host to nematode parasitism is readily utilised. In short, a wildtype, and mutants of *A. thaliana* are grown in 5 cm petri dishes in sterile culture. The plants are inoculated with infective second stage juveniles (J2) of the cyst nematode *H. schachtii* after four weeks. The number of successful infections is scored under the microscope two weeks post inoculation. Typically, the assessment differentiates successful infection between female and male nematodes. While this technique is very powerful, it remains prohibitively time consuming. To address this constraint, an image-based analyses method was developed.

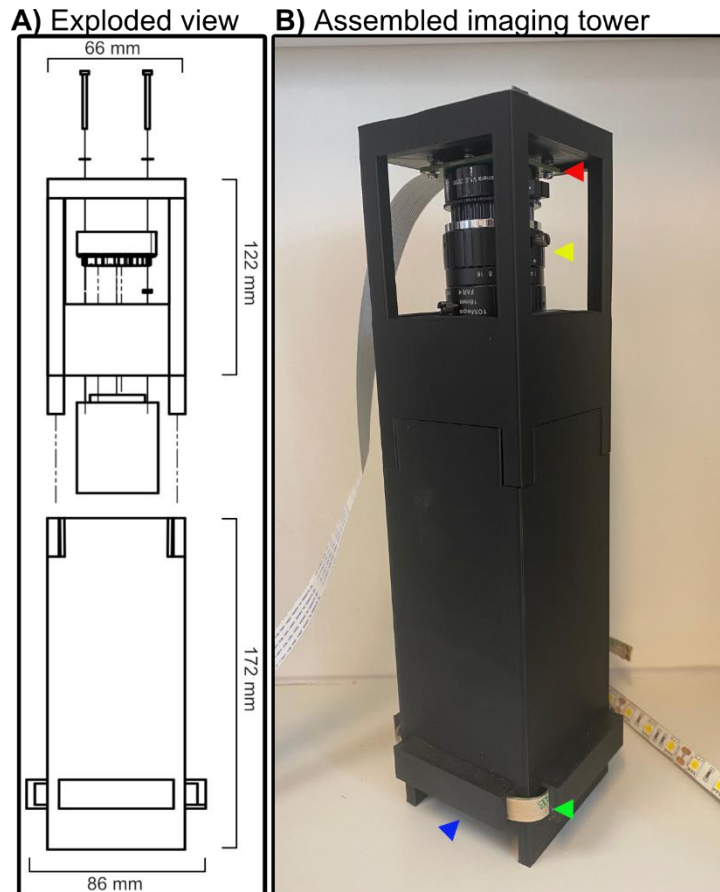
A crucial first step was to obtain consistent high-quality images of nematode infection. Images are required to have high resolution (i.e. large number of pixels per object of interest), high contrast (with the background and with the object of interest) and consistency in lighting. All these components are crucial for downstream applications using computer vision.

A Raspberry Pi was chosen to build the affordable open-source imaging platform. The housing was designed in two pieces due to printing height limitations of the Ultimaker S3 3D printer. The upper half of the housing mounts a 16 mm telephoto lens combined with the 12 MP High Quality Camera Module (Figure 4.2 B) facing down into the imaging tower. The lower half of the tower houses a flexible LED strip, and has a compartment for the petri dish (Figure 4.2 B). The feet-like extrusions on the top half, fit into the apertures of the corners of the bottom part, forming the imaging tower (Figure 4.2 A).

The printing process takes a total of 30 hours (on a Ultimaker S3, Ultimaker PLA with 20% infill). Assembly of the housing and the components takes about 30 minutes. The camera module is connected to the Raspberry Pi via a ribbon cable to the camera port. To get an object of interest in focus two parameters were adjusted on the lens.

For purposes of nematode phenotyping a narrow depth of field is crucial to minimise artefacts introduced by the background. The aperture of the lens was opened to the max setting (lowest F-stop) to provide us with the narrowest DOF. Background objects are more in focus when using a lower aperture (higher F-stop), and results in a relatively darker image.

On average, using this device, images of *A. thaliana* can be taken roughly every seven seconds. Importantly the state of nematode infection is captured rapidly (minimising the time a sample is outside the plant growth chamber) and is non-destructive (allowing for re-analysis of the same sample over an extended period). Together, this means that the state of the nematode infection is decoupled from the phenotyping event (i.e. we no longer phenotype the petri dish, we phenotype the image of the petri dish). This is important because imaging is fast and phenotyping is slow. Once the infection has been digitised, there is no more time constraint to phenotyping.



C) Manual quantification of infection

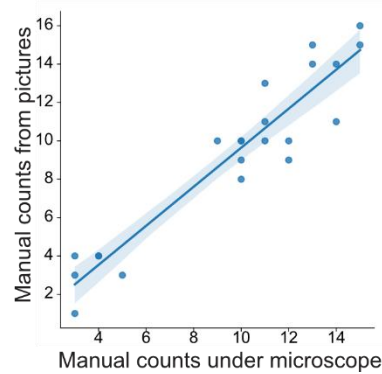


Figure 4.2: The static imaging tower. A) There are two printed components that make up the tower, a lower half, and an upper half. The lower half has an area cut out where the petri-dish can be slid into (blue arrow). Additionally, there are extensions on the side that allow for seating of a flexible LED strip, that is used as a lighting source for imaging (green arrow). At the top of the bottom half are intrusions that allow for the extrusions on the bottom of the upper half to be slid into. B) The upper half of the tower houses the camera board (red arrow), which is mounted to the tower via M2 nuts and bolts. A telephoto lens is screwed into the camera (yellow arrow). The camera board is off-screen mounted to the Raspberry Pi via the camera port. The LED strip is connected to an external 12V power supply outside the figure. C) Correlation between manual counting of female and cyst nematode under the microscope and from an image. For these counts, no distinction is made between a female before and after tanning. The counts correlate with an $R^2 = 0.94$, based on Pearson correlation.

4.4.2 Manually quantifying infection from images.

As a proof of principle that counting from images is roughly equivalent to counting under the microscope a small manual screen was performed. Counts between the two methods correlate with an $R^2 = 0.94$ (Figure 4.2 C). From the captured images, only the female and cyst life-stage can be consistently observed.

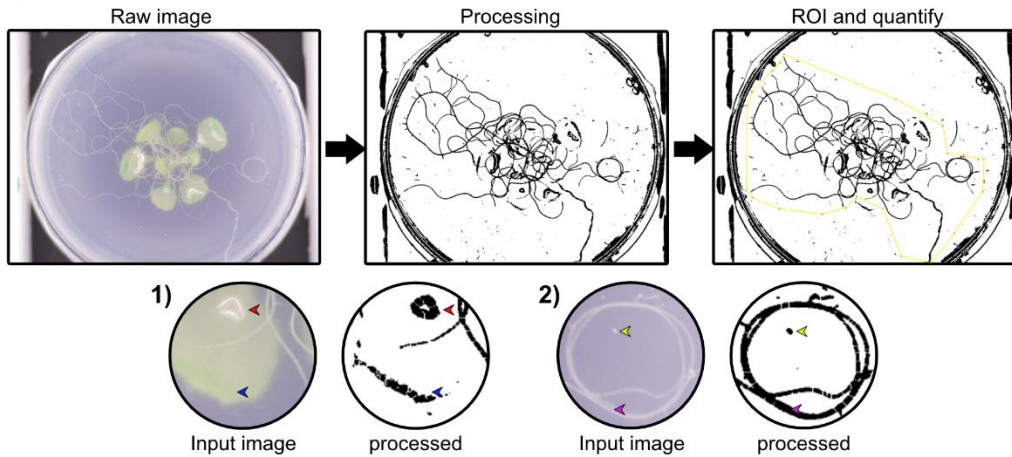
In general, in cyst nematodes, females are easier to detect than males. Females are larger, opaquer, and remain attached to roots for their entire life. Pre-emergence males (i.e. differentiated but not “hatched”) are very small, fusiform, and transparent. They have a narrow window for detection because they hatch and become migratory again.

4.4.3 The effect of root surface area on infection efficiency

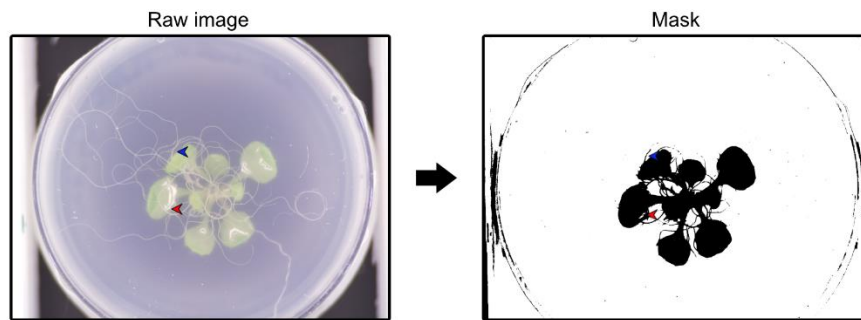
We hypothesise that the total number of parasites, at least in part, is dependent on the physiology of the root system. One of these parameters we can quantify for is total root surface area. Via thresholding of pixel values, a distinction can be made between objects on an image. A mask (a layer of pixels) can be put onto these objects, allowing for quantification of the entities. Built-in tools in ImageJ are used to extract root surface area (Figure 4.3 A). Artefacts introduced by folded leaves and air bubbles (Figure 4.3 A1), or specs of dust and joined roots (Figure 4.3 A2) are included in the total root surface area. The overall size of the artefacts is small, and is present in almost all petri-dishes, and is therefore not a major concern. The resulting mask overlaying the roots is counted in number of pixels. Using a similar technique, the leaf surface area can be calculated from the same images (Figure 4.3 B).

Two genotypes were selected, a T-DNA knockout mutant AT1G07540 (N804585), a plant gene highly expressed during nematode infection⁶⁸, and wildtype Columbia 0 (Col-0). The number of successful infections were manually counted for males and females under the microscope. The count was then normalised to the estimated root surface area. The resulting models describe the effect of root surface area to nematode parasitism at an infection density of 80 infective stage nematodes/plant (Figure 4.3 C). The general trend, independent of the genotype, is the number of parasites increases with root surface area before infection. In Columbia 0 wildtype, 4% of female, and 3% of male variation, and on the mutant line N804585, 10% of the female and 54% of the male variation is explained by root surface area before infection (Figure 4.3 C).

A) Feature extraction pipeline



B) Leaf surface area extraction



C) Models of effect of root-surface area on the number of successful infections

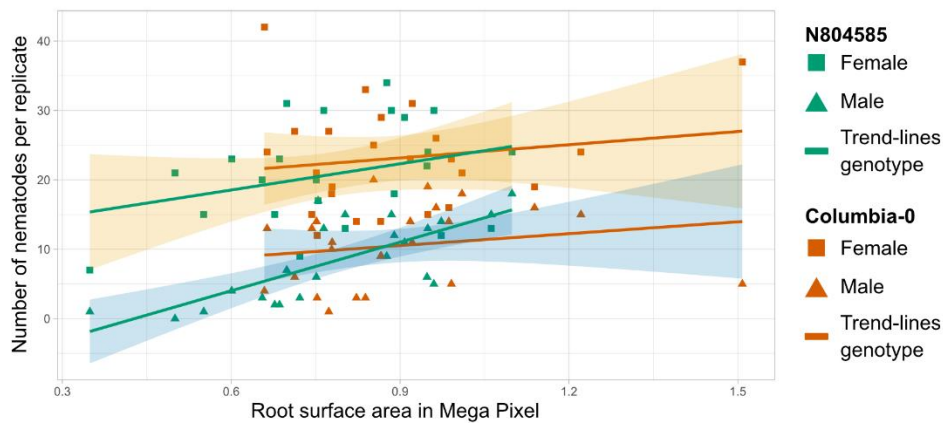


Figure 4.3: Quantifying root-surface area and visualising the effect on nematode parasitism. In A) The pipeline used to extract root surface area from an image. First, the background is removed, and a mask is generated of the roots. The mask is then segmented into smaller sections via water shedding. The user then defines an outline around the roots (ROI). The smaller sections are then quantified in ImageJ using the measure function. This process is not flawless. As shown in A1: air bubbles (red arrow) and folded leaves (blue arrow) can introduce artefacts. As shown in A2: artefacts can also be introduced by external factors, like specs of dust on the exterior of the petri-dish (yellow arrow). The pink arrow shows misrepresentation of roots, where two individual roots are grouped together into a single mask. The same masking technique can be used to quantify leaf surface area. Like above, artefacts can be introduced by air bubbles (red arrow) and roots (blue arrow). In C) effect of root surface area on nematode infection for two genotypes. On the left Columbia 0 ($n = 24$), and on the right N804585 ($n = 23$, Columbia 3 background). The y-axis show the number of successful infections, plotted against the root surface area in megapixel on the x-axis. Depending on the genotype, the effect of root surface area is more pronounced.

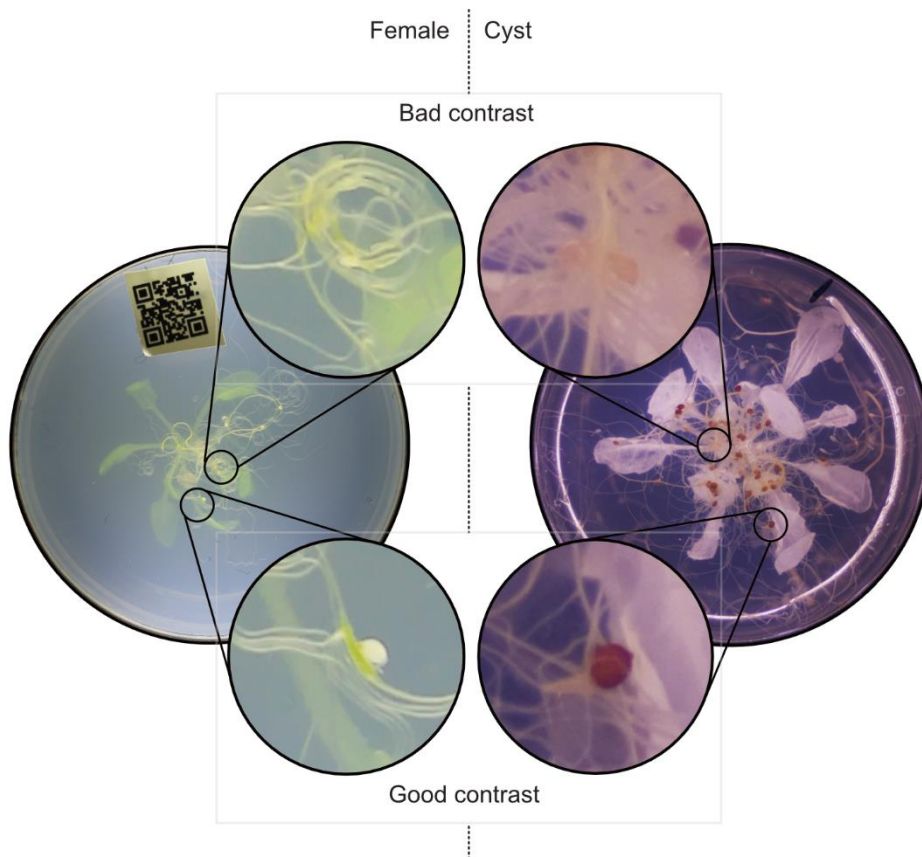
4.4.4 Automatically quantifying infection from images.

Females and cysts are clearly visible from the images of infection on petri-dishes. This is already a benefit as the phenotyping can be done at a later point manually. However, this process remains time consuming. Since the assay is effectively digitised, it may be possible to have parasitism quantification processed by a computer. It is expected a different technique may be needed to reliably identify the distinct different phenotypes between life stages of the nematode. We therefore generated two different methods for both female and encysted nematodes.

4.4.4.1 *Quantifying cysts*

In general, the better the contrast between features, the easier it is to distinguish them using threshold-based object segmentation. The best contrast between nematodes and background can be found in the cyst stage of the nematode (Figure 4.4 A). During this stage, the nematodes cuticle tans, and changes from white to brown. Empirically a colour threshold is defined for one of the images in a series that best performs in isolation of cysts (minimal false positives). Colour thresholding is sensitive to slight variation of the colour histogram between images. To minimise the effect, the histogram of each image in the series is normalised to the image used to set the threshold³²⁷. Using the thresholding method 147 cysts compared to the manually scored 230 (63.9 % accuracy) can be found. Additionally, to the correct identified cysts, 3 false positives were observed (1.3 %) (Figure 4.4 B). The resulting masks were counted, and their size was concurrently quantified. With only using colour thresholding, it remains inefficient to quantify cysts.

A) Contrast between life stages



B) Counting cysts

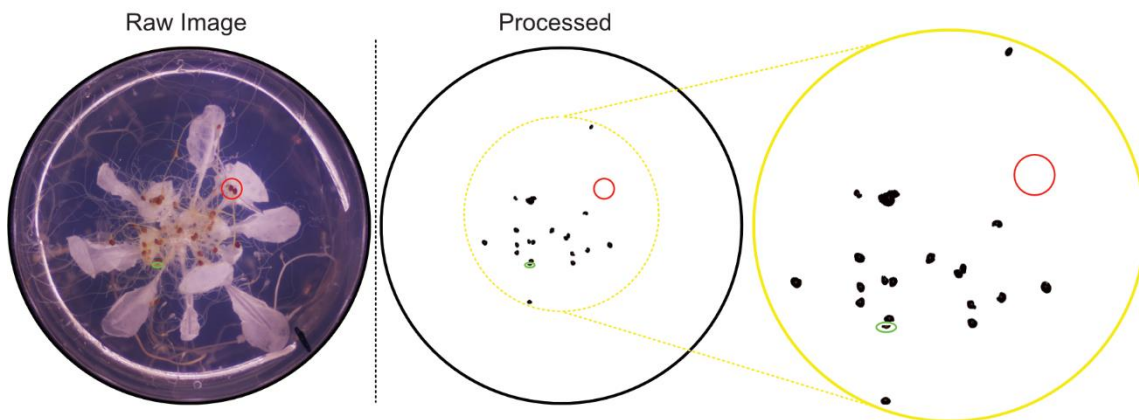


Figure 4.4: Comparison of contrasts, and quantification of infection on images taken using the static imaging tower. Images were taken during two distinct life stages of the nematode: female and cyst. In A) on the left is an image of the female life stage, and on the right during the cyst stage. In both cases, nematode visibility is variable. On the top section a zoomed in example can be seen of nematodes with bad contrast to the background. At the bottom nematodes can be seen with good contrast against the background. In B) the quantification using colour thresholding is visualised. Using a red circle, two missed nematodes are marked. With a green circle, a non-existent nematode is identified by the algorithm.

4.4.4.2 Quantifying females

The same thresholding technique used for cysts does not allow for isolation of females from images because females lack a distinct colour contrast with plant roots and senesced leaves. To increase the contrast, it was expected a modification to the protocol was required. By addition of food colouring to the axenic culture media, and illumination with red, green, or blue light, the contrast between nematodes and the background can be noticeably improved (Figure 4.5). Interestingly, depending on the light-dye combination, either the female or cyst life stage is highlighted. For example, the blue light with red dye combination highlights females, where under the same lighting condition with teal dye, cysts are highlighted (Figure 4.5). The translucency of the agar does not appear to change visually, minimising the impact on visibility of the nematodes. The greatest increase in contrast for female nematodes was found using a red food colouring (Limino, DYL-ghm-20210126-324) illuminated with blue light (380-500 nm, Figure 4.6 A). The illumination with other lights produces a similar contrast increase, but also highlights artefacts present on and in the petri-dish. Using the same colour threshold technique as before, however, still does not result in effective isolation of female nematodes. Morphological segmentation ³²⁶, a well-established ImageJ plugin, combines various morphological operations to separate object from an image. Using this tool, in addition to manual verification, 70 out of the 75 female nematodes can be isolated (93.3 % accuracy) (Figure 4.6 A). Through this technique, however, many false positives are introduced, requiring human characterisation of the masks.

In addition to the number, the segmentation also outputs size of each individually segmented object. Compared to manual measurements, size can be automatically quantified with an R^2 of 0.83 for females on red coloured agar, and an R^2 of 0.44 for cysts on un-dyed agar (Figure 4.6 B).

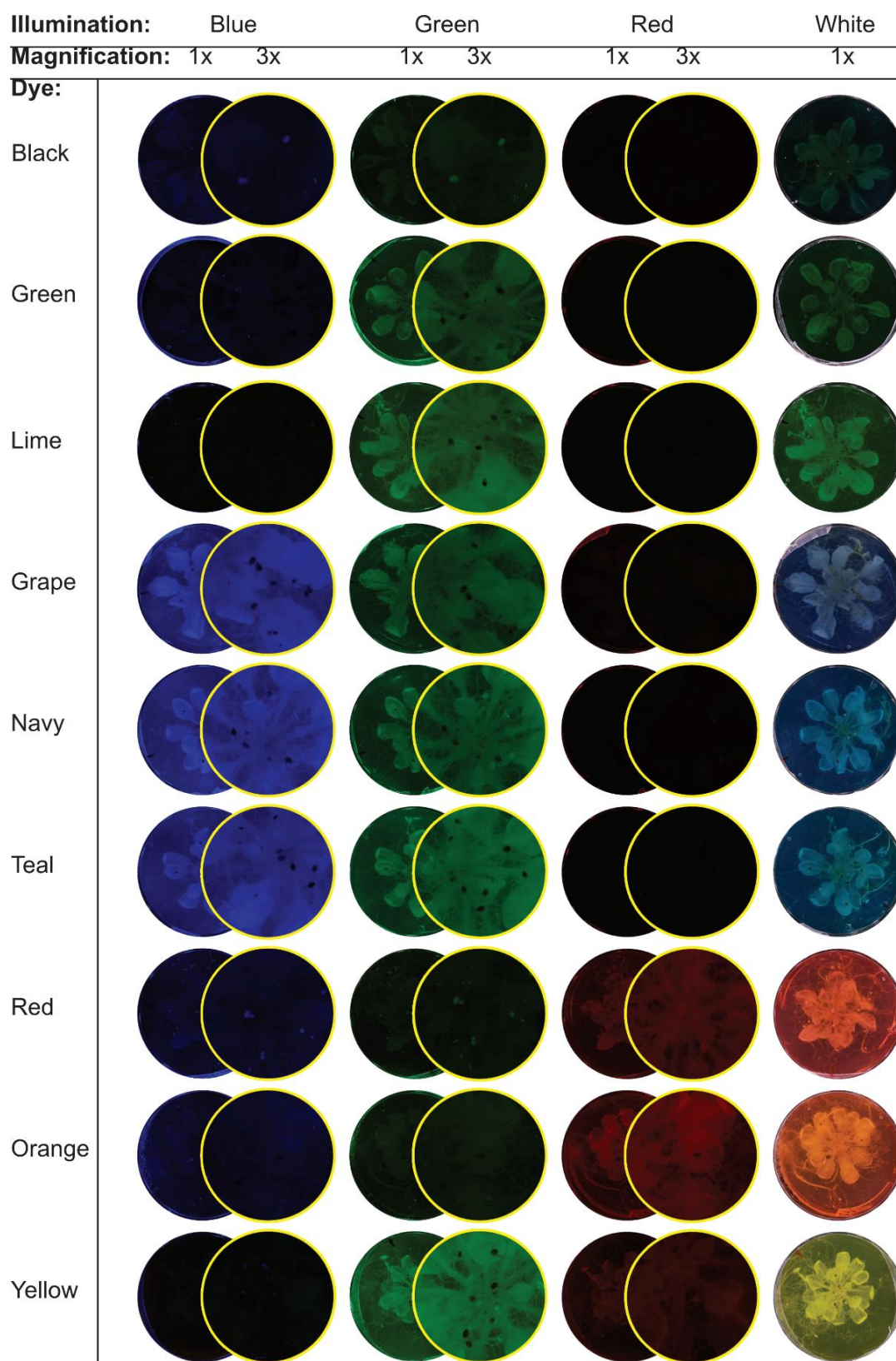
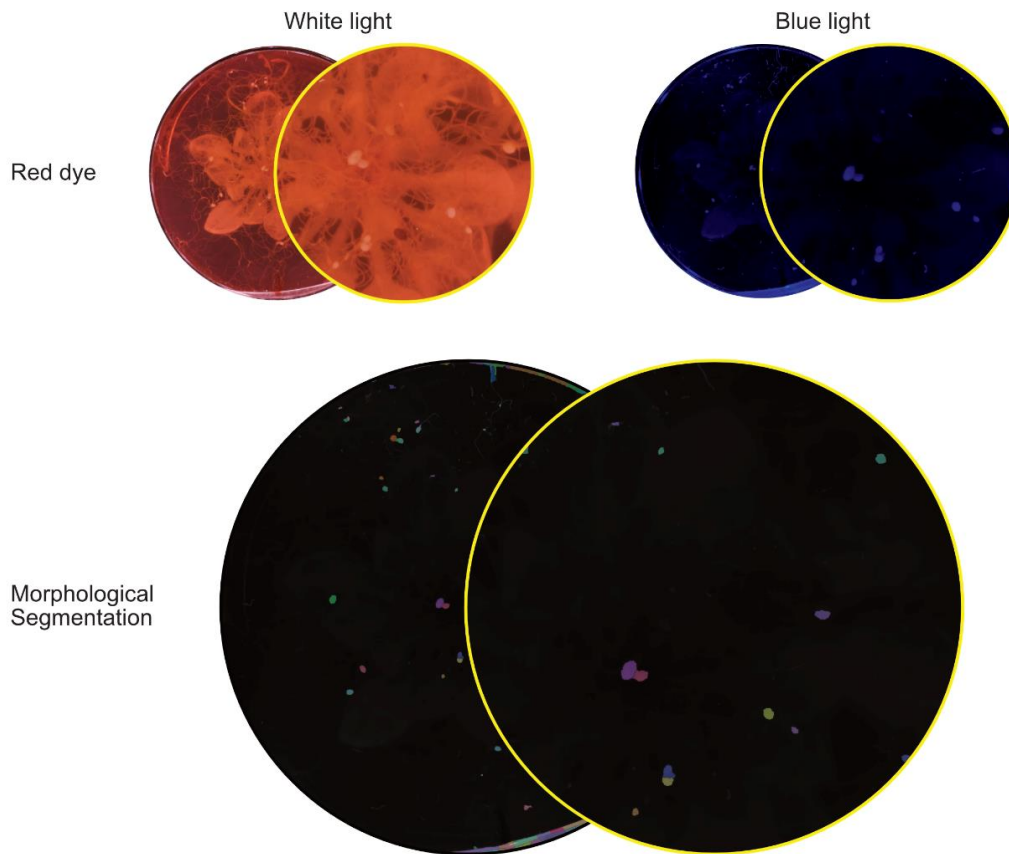


Figure 4.5: A visual representation of the effect of dye colour and light illumination on the visibility of *H. schachtii* on *A. thaliana*. The figure does not show any dyes that were lethal to the plant. From top to bottom the dyes used are: Black, Green, Lime, Grape, Navy, Teal, Red, Orange, and Yellow. From left to right, the colour of the illumination used is: Blue, Green, Red and White light. The yellow circles indicate a three times zoom.

A) Morphological segmentation



B) Size correlation manual vs Semi-Automatic

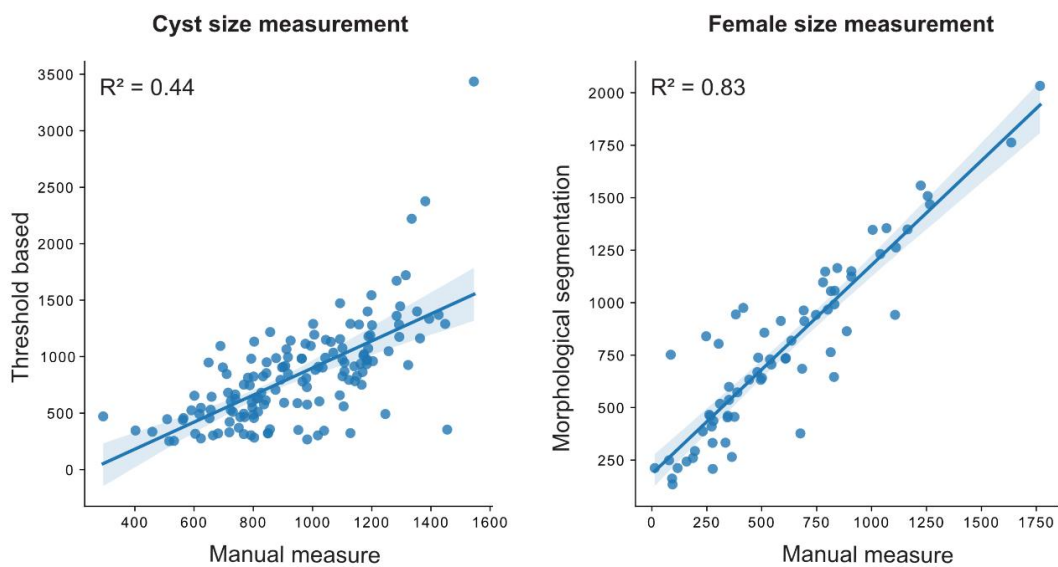


Figure 4.6: Quantifying female nematode infection using Morphological segmentation. A) The best contrast giving dye (red) is used here as an example. On the left is the petri-dish illuminated under white light, and on the right the same petri-dish under blue light. Below is the result of morphological segmentation on the red agar illuminated with blue light. The yellow outlined circles are a zoomed view of the same dish. In B) the correlation between human measured nematode size against either colour threshold based in cysts or morphological segmentation based for females. The correlation has an R^2 of 0.44 for cyst and 0.83 for female measurements.

4.4.5 Reducing hand-on time

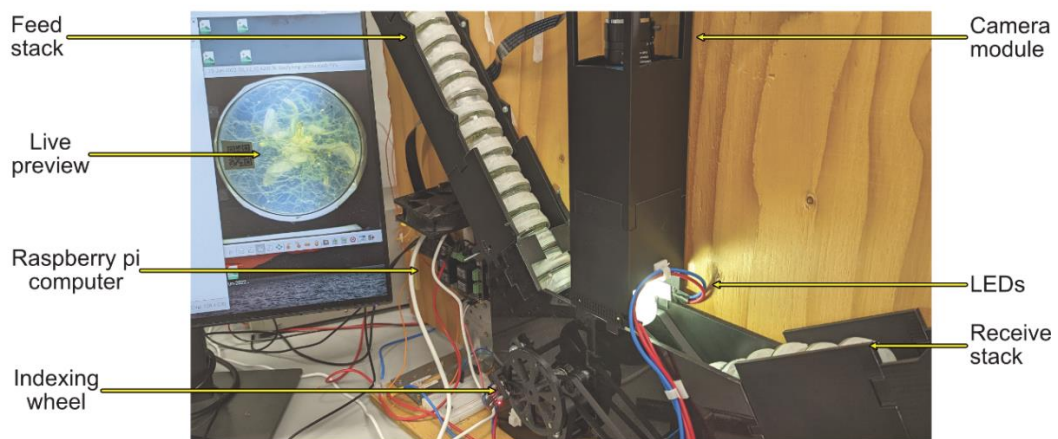
The main limitation to the well-established protocol ⁶⁹ is speed. The previously described attempts to automate phenotyping via image analyses are a step in the right direction, but suffer from limitations in inaccurate (when counting cysts) or require manual verification limiting speed of screening (when counting females). Recently, in collaboration with Ji Zhou, an expert in the field of plant disease phenotyping at Nanjing Agricultural University, China, we have been working on a deep learning AI model to detect female infection of *H. schachtii* on *A. thaliana* in axenic culture. As of date of writing the model predicts cyst nematode infection with ~90% accuracy, at an average speed of 11.92 seconds per image (based on a total of 5,000 images processed). Importantly, the model is on par with the morphological segmentation technique, does not require manual verification, and is more than 26 times faster than manual counting. This tool shifts the bottleneck from phenotyping to image capture. Using the static imaging tower, a capture of a petri-dish can be made roughly every seven seconds (loading of plate into the tower, capturing the image, and loading the next petri-dish). The scalability of the device is directly linked to the manual feeding of petri-dishes into the tower. To overcome this constraint, we designed and developed a semi-automatic imaging robot. The design of the machine was a collaborative process: the indexing wheel, imaging tower and electronic components/command script are part of this thesis; the motor mounter was principally designed by Sebastian Eves-van den Akker; other components were principally designed by Siyuan Wei.

The machine accepts stacks of petri-dishes on one end, and through a rotating feeding mechanism, loads a petri-dish from the stack into the tower (Figure 4.7 A). A hall effect sensor, attached to the Raspberry Pi, detects a magnet which is placed inside a revolver (Figure 4.7 A-B). The position of the magnet is linked to the feeding wheel in such a way that when the magnet passes the sensor, a petri-dish is directly under the camera. A custom Python script is used to control the image machine, and the logic. The hall effect sensor changes the output state, pausing the feeding mechanism, and triggering the image sequence (Figure 4.7 C). Based on observation, the capture time is highly variable. Additionally, calling the capturing command twice will cause the imaging command to crash, resulting in corrupted images (truncated sensor information written to a file). To avoid this error, the machine will pause and wait for image capture to be finalised before loading the next petri-dish. Once finished the feeding mechanism restacks the imaged petri-dish on the other side of the imaging machine. The above logic will repeat until either, the user stops the program or uses the manual switch to pause the machine. The feeding mechanism is also interrupted if the proximity sensor either detects no dishes in the feeding stack or too many dishes in the restacking side.

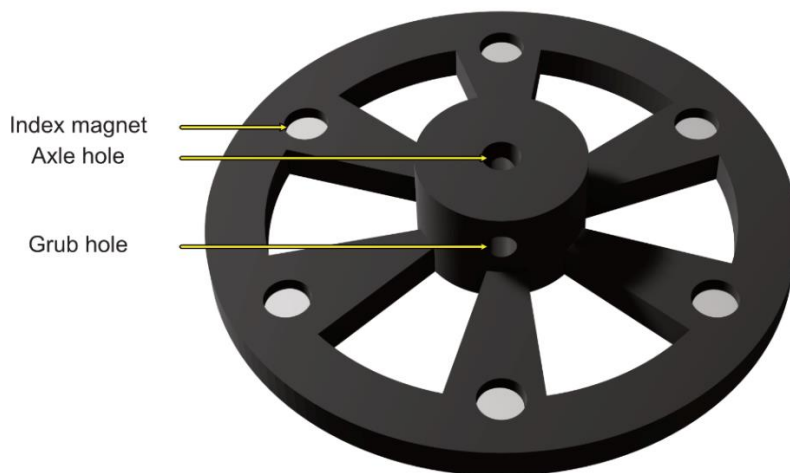
The new imaging robot allows for image capture of a petri-dish every six seconds. However, the robot allows for scalability, with a single person able to manage multiple machines. With only 6 machines, imaging time is down to one petri-dish per one second. In our hands, roughly three people are needed to manage six machines (imaging 10,000 Petri Dishes in four hours).

The AI and semi-automatic machine in tandem increase the efficiency of phenotyping 24-fold compared to the traditional assay, bringing down total time required to 12.92 (from 320) seconds per replicate (assuming six machines, and 11.92 seconds per image analysed). However, in practice, it's even more efficient. In a workday, one replicate can be captured every one second, that is 25,200 replicates (seven-hour work, one hour break). A large dataset like this would take about 84 hours to be analysed by the AI, but can do so tirelessly, and if needed, is scalable with more computing equipment.

A) Petri-dish imaging robot



B) Indexing wheel



C) Electronics logic workflow

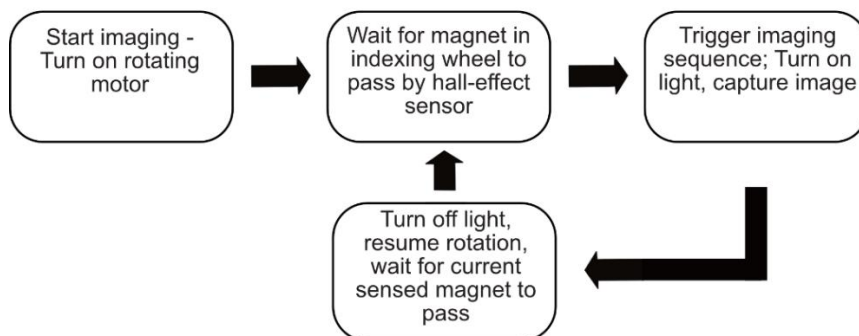


Figure 4.7: Overview of working operations of the semi-automatic imaging robot. A) components of the imaging robot, the feeding stack is filled with petri-dishes ready to be processed, once a plate is under the imaging tower, a picture is taken. The plate is then restacked on the receive stack. The LEDs embedded in the tower provide lighting for the camera module. The Raspberry Pi is connected to the camera and saves the camera to a hard drive after showing a preview on the computer screen. B) The indexing wheel consists of a 6 spoke wheel, with every spoke having seating for a small magnet. The wheel is fitted on the same axle as the rotating mechanism of the robot, and the grub hole is used to fix the position relative to the mechanism. C) Flow of imaging is controlled with the coding language Python, through the interface of the Raspberry Pi.

4.5 Discussion

Knowledge of resistance and susceptibility to plant parasitic nematodes remains scarce. A main bottleneck in identifying either resistance or susceptibility genes is the speed of phenotyping.

The well-established axenic *H. schachtii:A. thaliana* infection assay is readily used to screen for genes involved in nematode parasitism^{68,69}. The assay, however, has some clear limitations, as described in the introduction of this chapter. The most important is speed, and the lack of normalisation to physiologic variation of the host. Both constraints are limited by the laborious nature of the assay.

4.5.1 Automation of nematode parasitism phenotyping

4.5.1.1 Hardware considerations

A computer could be used to automate phenotyping. This essentially requires digitisation of the assay. The female and cyst life stage are visible with the naked eye and can easily be digitised via image capture. Small single-board computers, like the Raspberry Pi allow for an affordable digital camera solution. To use these components for digitalisation of the nematode infection assay, housing is required that consistently places the petri-dish in camera frame.

Very early preliminary experiments showed that the lower quality V2 Raspberry Pi camera (8 MP) lacked resolution to clearly distinguish features the size of nematodes on a picture (data not shown). Using the exact same imaging setup, but swapping out the camera, the features become clear. Compared to the High-Quality Raspberry Pi camera (12 MP), there are two main differences: 1) a non-detachable lens; and 2) a lower resolution. Unavailable at the time, the camera module V3 has been released. This camera uses a 12 MP sensor, and could be used to elucidate whether the optics, or the sensor make a bigger difference in generating contrast.

To accelerate the design process, and allow for ease of sharing the device, a 3D printed imaging tower was created. At time of writing, in house, the design can be printed for £10.87 (Ultimaker PLA, on an Ultimaker S3). However, acquiring a 3D printer can be costly. Online printing services allow for an ideal mid-way solution for those that need to print sporadically³²⁸, and the same print can be printed for only ~£67.56³²⁹.

A 3D printed solution is attractive as it allows for rapid global sharing of a physical tool. By making it open-source, any scientist anywhere has the rights to not only use, but amend the design to their specific needs. This means that the application of the tool is not limited to what its designed for, but may be used as a benefit to other research fields.

Other partially 3D printed designs exist for imaging of petri-dishes. A high quality, Raspberry Pi powered, imaging robot is available for tracking of *C. elegans*³³⁰. Importantly, to achieve the high quality images, this machine needs additional hardware to function. One big difference compared to our method is the price. Based on current prices of the components used, this setup would cost at least £546.

The global computer chip shortage of 2020 has severely limited the availability of the Raspberry Pi^{331,332}, and has led to an increase in price for all single-board computers. This may make cheaper alternatives attractive, such as Libre Le Potato, which is available starting at £35, compared to £55 for the Raspberry Pi.

4.5.1.2 Software limitations and solutions

The same imaging tower can be used at a later stage (21+ days post inoculation) to digitise nematode infection of both the female and the cyst stage. To quantify nematode infection from these images two different approaches were used for females and for cysts. Cysts are the only life stage where the nematode isn't either transparent, or similar in colour to the root or shoot. A threshold-based segmentation method can be used to isolate tanned cysts from images at 63.9% accuracy, 1.3 % false positive and 34.8% false negative. This error prone method is mainly limited by slight deviations in colour between petri-dishes. While colour histogram normalisation appears to help, it doesn't eliminate the problem. The threshold can be adjusted to reduce false negatives, but this generally increased the false positive ratio. To reliably capture most cysts, a separate colour threshold for each nematode may have to be defined. This would be undesirable as this would drastically increase manual labour.

The female life stage is similar in colour to *A. thaliana* roots. Adding red colour to agar, and illuminating with blue light (380-500 nm) increases the contrast of the female nematode with the background. While the exact reason for the increase in contrast is unknown it may have to do with filtering effect of coloured substances: red agar only lets through red light³³³. This can be observed under ambient light, where everything through the agar appears red (only wavelengths of the red spectrum can reach your eye from the other side of the agar). When illuminated with blue light, almost the entire background (plant shoot, and most roots) disappears. This is expected as most of the blue light should be adsorbed by the red agar. However, the same is not true for female nematodes. This suggest that reflecting light from female nematodes is at least partially enriched in longer wavelengths, which are able to pass through the agar and reach the camera. Females do not get a better contrast in blue light when in yellow agar (which absorbs light shorter than red). This could mean that the reflective light is predominantly red of female nematodes under blue light. The same effect can be observed for cysts in cyan agar under blue light, where the cyst appears as dark spots. This

could be explained by the cyst reflecting the light in any but blue light wavelengths. Taken together, using coloured agar and light, contrast can be dramatically improved. Morphological segmentation and manual verification of the mask from these images results in 93.3% accuracy with 6.7% false negative.

Use of the static imaging tower, with manual verification of the digital analyses and manual image capture, does not increase the screening speed compared to traditional phenotyping. However, once infection is digitised, quantification is not limited to a single day. Since taking the images is faster than quantification, the overall efficiency still goes up.

To minimise hands-on time required to analyse the digitised assay, in a collaboration with Ji Zhou and Jie Zhou from Nanjing Agricultural University, our groups have been working on developing a Deep Learning computer vision-based method for identifying nematodes. Using this tool, we can achieve ~90% accuracy in counting, and importantly it does not require manual verification of the counts (unpublished). This will solve many of the limitations of the threshold based-object detection described herein. This new invention essentially shifts the bottleneck from phenotyping to speed of digitisation.

To increase speed, a semi-automatic feeding mechanism was built. The new robot, when scaled up to six robots, allows for image capture every one second. Included in the continuous imaging robot are sensors to maintain correct operation between the imaging of every dish. The hall effect sensor, together with the software, have successfully worked at least 500,000 times. The proximity sensors, used to indicate whether either the feeding arm is empty or stacking arm full, only work in lower light intensity conditions. Under ambient light, the sensors behave as expected, however, in a green house, under growth light, the sensors were not able to reliably distinguish differences within the arms. Proximity sensors are sensitive for red light. Either the direct sunlight or the growth lights in the glasshouse cause the sensor to trigger. A sensor with more control over the sensitivity may be used in the future to avoid these issues.

To date, the method does not allow for quantification of male nematodes. Male nematodes are much smaller than females when attached to the root, do not emerge as much, and can't reliably be distinguished from artefacts. This may in the future be resolved with better lenses and higher-quality cameras, essentially increasing the number of pixels per nematode, increasing clarity.

4.5.2 Plant physiology in nematode parasitism

In the traditional assay, host phenotype is generally not considered when scoring the effectiveness of nematode infection. For example, knockdown of the PLC5 gene in *A. thaliana*

results in less root surface area³³⁴. We hypothesise that total infection is dependent, at least in part, on phenotypic variation of the host root system (even in genetically identical plants). It is therefore an important parameter to consider.

Given the available data, and the high variability in nematode infection efficiency, a good model that describes nematode infection based on root surface area remains difficult to construct. This indicates that root surface area alone is not the main impacting factor for nematode parasitism. In Figure 4.3 C, the relationship between infection and physiology is visualised for two different genetic backgrounds. Interestingly, infection appears to be less affected by root surface area in the Col-0 ecotype, compared to a mutant line from the Col-3 ecotype (N804585). Importantly, the overall root surface area in Col-0 was higher than in the Col-3 background. Therefore, the observed effect may be a result of overall root surface area, where a lower density has a larger impact on nematode number than a higher density.

Regardless, in both backgrounds, the number of nematodes is positively correlated with root surface area for both male and female nematodes, meaning lower root surface area, would result in fewer nematodes. This observation is likely not relevant to nematode control in the field, as a reduction in root surface area would likely have a negative effect on yield, but, the parameter is important in consideration for susceptibility screening.

4.6 Conclusion

Utilising the filtering capabilities of coloured agar under illuminated lights can be used to increase contrast for the female and cyst life stage on captured images. Females are easier to detect using computer vision in coloured agar, however, the cyst life stage remains difficult. Depending on the host genotype, root surface area is correlated with the number of nematodes. It may therefore be important to normalise for this factor. There is still much improvement to be made in automating of phenotyping in software. Preliminary data suggests that deep learning computer vision-based methods will massively improve the accuracy of automated phenotyping.

5 Chapter five - Identifying a tissue independent response to nematode parasitism

5.1 Introduction

Cyst nematodes parasitise on their host via a nematode-specific feeding pseudo-organ variously referred to as the syncytium or the syncytial feeding site. The nematode injects the host with secretions produced in gland cells through a needle-like stylet, which is inserted into a single host cell. Thought to be principally proteins, these secretions may alter enzymatic activity and/or gene expression, alone or by interacting with host proteins. The effect on plant transcription of nematode parasitism is characterised in detail for the model plant *Arabidopsis thaliana* infected by the cyst nematode *H. schachtii*⁶⁸.

Over the course of infection, 59 % of *A. thaliana* genes (19,071) are significantly differentially regulated. The transcriptome of infected tissue of *A. thaliana* is most dissimilar to the uninfected control at early stages (10 hours post infection) and converges with uninfected tissue over the course of the nematode's life cycle. The transcriptome of a male syncytium lies roughly in the middle of a syncytium and uninfected tissue. This is argued to be an indication of the male nematode halting the maintenance of the syncytial feeding organ prior to regaining mobility⁶⁸.

The vitamin B5 (pantothenate) biosynthetic pathway (apart from the pantothenate synthetase step) is up-regulated during parasitism. Pantothenate is an essential vitamin for which the biosynthetic pathway typically is absent in animals. *Heterodera schachtii* however, has two genes that are annotated to carry out the final step in vitamin B5 synthesis, which is hypothesized to be obtained via horizontal gene transfer of bacteria⁶⁸. A knockout of either the plant- or nematode encoded genes results in a reduction of infection efficiency⁶⁸.

A large proportion of the altered expression is likely an indirect consequence from the various alterations made to the host cell, and only a subset of the genes is important for establishing and maintaining parasitism. It is known that knockout mutations of some of these genes have a negative impact on infection^{68,69}, and are termed susceptibility (S) genes. There is a general interest in finding these genes as they not only enhance our insight into parasitism but may also lead to routes to control (especially considering CRISPR, and the increased ease of generating knockout mutants).

5.2 Screening for susceptibility genes

An infection assay is typically used to screen for putative S genes. In short, hosts with the functional version and hosts with a knockout/knockdown mutation of a gene of interest are

inoculated with nematodes. Various parameters can be scored to indicate loss of susceptibility, such as infection frequency, size of syncytium, male-female ratio, female and cyst size, number of eggs per cyst and viability of the eggs^{68,69}. If a reduction in infection is found, a complementation assay is then typically used by re-introducing a functional copy of the gene in the knock-out line. A recovery phenotype for susceptibility, together with a reduction in the knockout assay, form a strong base for a causal relationship.

To expedite screening, the broad library of transfer DNA (T-DNA) mutants available for *A. thaliana*, together with the SALK, GABI-KAT, SAIL, and WISC contain over 260,000 mutant lines, generating potential knockout mutants for almost any gene¹³⁹. However, screening for susceptibility, even with the newly proposed methods in this thesis, remains time-consuming. Typically, involvement in biological pathways or the magnitude of transcriptional change is used as a selection method for genes of interest. While proven effective, this method is biased by the assumption that S genes are either involved in characterised pathways or are highly differentially expressed. In this chapter, we explore a new, less biased method for selecting genes of interest and generate a dataset that may enhance our understanding of nematode parasitism.

5.3 Identify the core transcriptional response to nematode parasitism

In agriculture, cyst nematodes feed on roots. However, as demonstrated by Steele in 1981, the cyst nematode *H. schachtii* can parasitise aerial tissue in laboratory conditions³³⁵. As mentioned above, the transcriptional response to infection of *H. schachtii* on *A. thaliana* roots is well-characterised. However, for other tissues, the transcriptional response remains unknown. Later observations from Golinowski et al. (1996) confirm that syncytium in aerial organs is similar in ultrastructure and function to those found in roots, indicating a conserved physiological response to nematode parasitism between plant organs³³⁶.

Clearly, roots and aerial tissues have considerably different starting transcriptional states, and yet both can arrive at a functioning feeding organ. The current hypothesis is that multiple transcriptional routes could lead to the formation of a syncytium. However, a subset of the response remains conserved regardless of the parasitised tissue. The overlap between the responses potentially highlights genes involved in the core of nematode parasitism.

5.4 Aims

5.4.1 Develop and optimise the assay for shoot infection

Shoot infection of *A. thaliana* of the ecotype Landsberg erecta has been previously observed^{119,335}. The transcriptional response in roots is mapped in ecotype Columbia-0 (Col-

0) ⁶⁸. Based on preliminary experiments, inoculation of shoot tissue with *H. schachtii* on Col-0 rarely results in successful parasitism. It is expected that optimisation of the inoculation protocol would lead to a higher frequency of infection, which is crucial for the collection of adequate infected shoot tissue for RNA sequencing.

5.4.2 RNA sequencing of shoot infected tissue

The published root infection dataset maps the transcriptional response during various stages of nematode infection. Due to the laborious nature of sample collection, only one life stage is collected for shoot infection. Transcriptional data of any life stage will provide important biological information about nematode parasitism. However, this dataset will focus on female cyst nematodes as they are, compared to the other life stages, the easiest to collect due to their size and have the largest associated syncytium.

5.4.3 Identify key differences and similarities between tissues

It is expected that the transcriptional response between different tissues to nematode infection will not be the same but share a conserved 'core'. Identifying not only the conserved, but also the differentiating response will enhance our understanding of the processes involved in nematode parasitism.

5.4.4 Test the impact of the absence of core genes on nematode parasitism

Lastly, I perform a preliminary screen of knockout mutants of a subset of the identified genes from above using the developed machines in Chapter 4 of this thesis.

5.5 Materials and Methods

5.5.1 Collecting leaf samples

For the detached leaf assay, leaves were collected from two-week-old plants grown under the conditions as described in 2.2, and placed in the same medium as described in 2.2, with the leaf petiole touching the agar. Detached leaves were inoculated with 200 sterile *H. schachtii* J2s obtained as described in 2.1. Whole plant inoculation was performed 14 days post-sowing. Plants were submerged in 0.4% Dashin agar (Duchefa), or inoculated with a smaller drop (50-500 μ L) of the same agar concentration either with or without 1.5 mM zinc-chloride, with the number of nematodes ranging from 0.4-4 / μ L. Plants were returned to the growth cabinet under the conditions described above.

Two weeks post-inoculation, infected leaf samples were collected. Infected samples were immediately transferred to 2 mL Safe-Lock tubes (Eppendorf) submerged in liquid nitrogen. From the same plant, a leaf sample of roughly the same age and size was collected as the uninfected control. A total of 15 samples (for both infected and uninfected tissue) were collected per replicate for three replicates. The samples were homogenised by adding one 5 mm glass bead and two 2 mm glass beads in a TissueLyser (Qiagen) at 30 Hz for 1 minute at -196°C . From the homogenised samples, RNA was extracted using the RNeasy Plant Mini Kit (Qiagen) according to the manufacturer's protocol. Library construction of the extracted mRNA (150 bp paired-end RNAseq) and sequencing was performed by Novogene.

5.5.2 RNA-seq analysis

To analyse the sequencing, a well-established pipeline was used for the transcriptomic analysis of infected *A. thaliana* root tissue with *H. schachtii*⁶⁸. A description of the used tools and settings can be found below:

To spot potential problems with the sequencing, the Illumina RNAseq reads were analysed using FastQC v0.12.1 (<https://github.com/s-andrews/FastQC>), and reports were generated using MultiQC v1.14 (<https://github.com/ewels/MultiQC>). BBDuk from BBTools (<https://jgi.doe.gov/data-and-tools/software-tools/bbtools/>) were used for trimming the reads, removal of the Illumina adapter, and for quality filtering. For every read, the first and last ten bases were removed, excluding the adapter sequences. Kmer length was set to 23, and for any reads matching a reference set of Illumina adapters was removed. The hamming distance was set to one to allow for a single mismatch of a kmer. The minimum read length after trimming was set to 75, with a minimum Phredscore value of 20 (99.9% accuracy). The same quality analysis was performed as described above on the trimmed reads. The sequences were aligned using STAR v2.7.10b (<https://github.com/alexdobin/STAR>) to the *A. thaliana* TAIR10 genome³³⁷. The number of reads mapping to genes was counted using htseq-

count³³⁸. The differential analysis was performed using DESeq2³³⁹, using a significance threshold of 0.05.

5.5.3 Identify candidate genes based on root infection and leaf infection

The list of differentially expressed genes of shoot infection was compared to the published root infection dataset⁶⁸ using the Linux tool comm. From the conserved up-regulated genes, homozygous T-DNA knockout mutants were obtained from the European Arabidopsis Stock Centre where available (Table 5.1). All lines were selected for having associated polymorphisms for only one gene. The genotype was determined using wildtype (LP+RP, $T_M = 61.0^\circ\text{C}$, Table 5.1) and mutant (BP (ATTTTGCCGATTTTCGGAAC) + RP, $T_M = 59.9^\circ\text{C}$, Table 5.1) primer pairs and was amplified using Phire Plant Direct PCR Master Mix according to the manufactures' protocol in a Veriti thermocycler (Applied Biosystems) using the parameters described in Table 2.1. Amplified DNA was visualised on a 2% agarose (Sigma-Aldrich) gel containing 1/1000 x SYBR Safe DNA Gel Stain (Invitrogen) in 1X TBE buffer in a G:BOX imaging station after separation of the DNA using a Powerpack (Bio-Rad) at 100 V for 25 minutes. *Arabidopsis thaliana* CS60000 was used as a wild-type control for all primer pair combinations. Depending on the primer pair, a different temperature was used for annealing: LP+RP $T_M = 61.0^\circ\text{C}$, BP+RP $T_M = 59.9^\circ\text{C}$.

Plants of each genotype were grown in 5 cm petri-dishes, as described in 2.2, for a replicate number of 30. The roots of each plant were inoculated as described in 2.3. Two weeks plus post-inoculation, the plants were imaged using the machinery described in Chapter 4. The images were externally analysed using a deep learning algorithm for quantifying nematode infection (unpublished).

Table 5.1: Primers used for genotyping. The primer pair LP+RP was used to amplify for the wildtype allele, and the combination BP+RP was used for the mutant allele. Primers were selected for amplification around the polymorphism site for a given NASC number. The target gene highlights the location of the T-DNA insert in the genome if present.

Target Gene	GO Biological Process	NASC stock number	Polymorphism	Genotype primer forward (LP)	Genotype primer reverse (RP)
AT1G11580	cell wall modification, pectin catabolic process	SALK_121787C	SALK_121787.41.30.X	TGTCGT CGTTAG TGTGTC GAG	AACAC GTGCA ATAGG TCAAG G
AT1G19670	chlorophyll catabolic process	SALK_119134C	SALK_119134.41.00.X	TTTGTT AGTTCC TGCGA CTGG	AGAGA GAGAG ACGGA GGTTG G
AT1G75040	defense response	SALK_055063C	SALK_055063.43.20.X	CATTC ATTAAT GGCTC GCTC	ATTGC TGTTAT GGCCA CAGAC
AT2G30970	2-oxoglutarate metabolic process	SALK_082821C	SALK_082821.46.35.N	TGTTAA GCGGT CAACCT GTTC	CTTCC TTCTTC ATGCT TGTGC
AT2G37620	cytoskeleton organization, developmental growth, root hair elongation	SALK_056339C	SALK_056339.53.25.X	TGATAG GGTTG AAACCA GCAG	TTGGG TTAAAT TGAAT CCGTG
AT3G03640	carbohydrate metabolic process, glucosinolate catabolic process, response to salt stress	SALK_039327C	SALK_039327.55.50.X	GATCTT GAGCTT GAGCA ATGG	TCATG AACCA AGCTC CAATT C

AT5G07800	Unkown	SALK_1147 00C	SALK_1 14700.52 .75.N	ACGCA ATATCA TGCAG ATTCC	GATAT GAGGA GGTTT CCAGG G
AT5G24280	double-strand break repair via homologous recombination	SALK_0369 31C	SALK_0 36931.54 .70.X	AGTCG ACGGA GAAAG AGAAG G	CTGCA ATCTC TTTCAT CCAGC
AT5G56640	inositol catabolic process	SALK_0516 20C	SALK_0 51620.52 .50.X	GAATAT CTCCGT CGAAAA CCC	AGATT CATCA AATGC ACACC C
AT3G21500	1-deoxy-D-xylulose 5- phosphate biosynthetic process, chlorophyll biosynthetic process, terpenoid biosynthetic process	SALK_1127 62C	SALK_1 12762.41 .75.X	TCAAAG TTCTGC AGATTA TCCG	TTCCA CAATT AGATT GCAGC C

5.6 Results

5.6.1 Optimisation of shoot tissue infection

While infection of the shoot has been reported for *H. schachtii* on *A. thaliana*¹¹⁹, the protocol as described in the paper could not be replicated. The existing transcriptional dataset is generated on *A. thaliana* ecotype Columbia-0, highlighting a key difference from the published method, which performs leaf, stem, and root infection on *A. thaliana* Landsberg erecta. Furthermore, the published method does not report infection frequency, which could mean shoot infections are rare events.

To generate a shoot-specific transcriptional response, we need to develop a method that reliably results in infection of the shoot. Three setups were trialled:

1) Detached leaves

A detached leaf can generate entire root systems and repair the mechanical injury through tissue culture-mediated regeneration³⁴⁰, allowing it to survive for a relatively long time. Furthermore, detached leaves are utilised to study responses to pests³⁴¹. Infection of such detached leaves would massively simplify the collection of infected samples.

Leaves were detached from two-week-old *A. thaliana* grown in axenic culture, placed on a bed of ½ MS agar, and inoculated with 200 infective stage J2s. After three weeks, from the 50 detached leaves, only two successful infections were observed (Figure 5.1 A). Importantly, the leaves did not regenerate roots. The infection was only limited to detached leaves missing the petiole. Infection appears to be centred around leaf midrib vascular bundles. The nematodes appear to be arrested at the J3 stage¹²⁰. In axenic culture, nematode infection is most frequently observed near the plastic bottom of the petri-dish. The hard surface is believed to aid in migrating of the nematode (personal communication). To generate a surface, a droplet of nematodes was placed in between the adaxial side of two detached leaves. This additional surface, however, did not result in parasitism (0/50).

2) Shoot infection of submerged plants in agar

In the detached leaf assay, nematodes were pipetted on the detached leaf while submerged in a water droplet. Due to the evaporation of the droplet, there may be a time limit for the nematode to migrate into the leaf tissue. Furthermore, if a nematode does manage to initiate parasitism, the development appears to either slow down or is halted at the J3 stage. To circumvent both these potential issues, a three-week-old *A. thaliana* plant was submerged in a solution of water and low percentage agar containing 200 J2 of *H. schachtii*. The agar was added to simulate a solid surface which may aid in the migration of the nematode.

Plants submerged in the agar solution expressed elongated leaf petioles (Figure 5.1 B1). The phenotype is consistent with other observations of submerged *A. thaliana* and may be a result of accumulation of ethylene^{342,343}, which is associated with elongation of the leaf petiole³⁴³.

This setup allows for the development of late-stage females and the formation of a well-developed syncytium (Figure 5.1 B2). However, submersion of the host does not increase infection efficiency (1/48).

3) Aerial infection of attached leaves

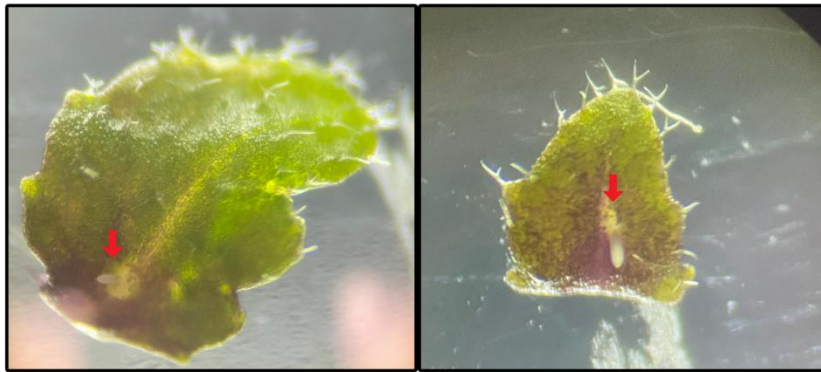
For all aerial inoculation, a droplet of liquid containing nematodes was pipetted onto a leaf. A low percentage of agar was added to prevent rapid evaporation of the inoculum. Varying numbers of nematodes were added to different droplet sizes, with only 50 µl with a density of 4 nematodes / µl resulting in shoot infection (Table 5.2).

The hatching of *H. schachtii* is accelerated by adding zinc chloride ($ZnCl_2$)¹⁴⁵. Based on personal observations, the movement of the J2 is higher in $ZnCl_2$ compared to water or tween, which are two common storage media for nematodes (data not shown). This suggests the further involvement of either zinc or chloride ions in the detection of the presence of a host. When a low concentration of $ZnCl_2$ is added to the inoculum, the infection efficiency rises to ~47 % (based on 48 inoculations). The increase in infection efficiency is accompanied by a systemic purple phenotype of the plant shoot (Figure 5.1 C). The same phenotype was observed with the same inoculum without nematodes.

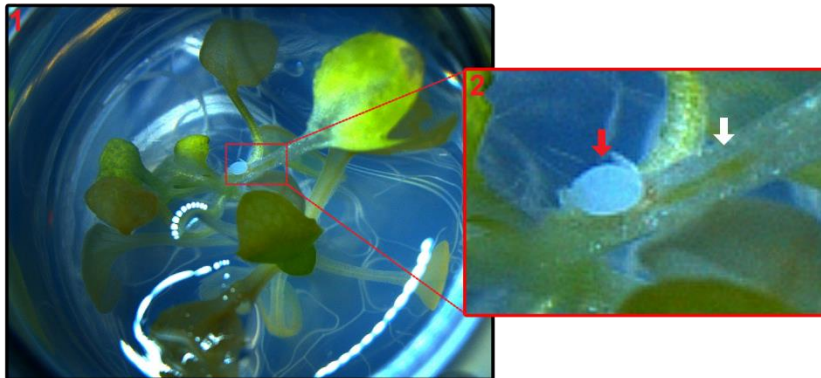
Table 5.2: The success rate of aerial infection of shoots of *Arabidopsis thaliana* with *Heterodera schachtii* for varying nematode densities and inoculum volumes. The count includes females only and indicates an infection rate of 40 inoculated plants.

Inoculum volume (μl)	Number of nematodes / μl	Infection rate
500	0.4	None
250	0.8	None
50	4	15 %
500	4	None

A) Detached leaf infection



B) Submerged shoot infection



C) Aerial infection



*Figure 5.1: Various experiments trailed for shoot infection. A) Infection of detached leaves. A leaf was detached from a two-week-old *A. thaliana* plant and placed with the leaf petiole touching the agar. Parasitism of detached leaves is rare and appears to arrest nematode development in an early stage. B) Plants are submerged in a low percentage agar solution with nematodes. Infection is observed mainly on the leaf petioles, where females appear to be fully developed (red arrow), the syncytium is clearly visible (white arrow). C) Aerial infection of shoot tissue. A droplet of inoculum containing zinc chloride was pipetted onto the leaf of the host. Infection is observed of various shoot tissues using this method and appears to allow for female development. The zinc-chloride treatment causes a systemic dark green-purple phenotype in the host.*

5.6.2 Shoot infection for one time-point

A total of 1,440 plants were grown for two weeks in 24 well plates with one plant per well and inoculated with 200 J2s in 50 μ l of 1.5 mM zinc chloride. Two leaves were inoculated opposite of each other, one with and one without nematodes. Two weeks post-inoculation, samples were collected from plants with infection. A leaf segment with the nematode and a corresponding segment of the other leaf of the same age were taken and immediately frozen in liquid nitrogen. The total collection took two hours for three technical replicates.

From the samples, RNA was extracted and sequenced. Reads are trimmed and mapped using an established pipeline ⁶⁸, mapping 135 million reads for infected tissue and 140 million reads to uninfected tissue. The differential gene expression analysis was performed using DESeq2 ³³⁹.

A principal component analysis (PCA) shows that one of the samples contributes to 97% of the variance in principle component 1 and 2% in principle component 2 (Figure 5.2 A). This sample was deemed an outlier, and removed from further analyses. The variance of the remaining samples was 54% in principle component 1, and 24% in principle component 2 (Figure 5.2 B).

The number of differentially regulated genes (Log₂FC > +0.5 or < -0.5 and adj. p value < 0.05) in shoot tissue is 178 (156 up, 22 down, Figure 5.2 C, Figure 5.3 A). The overall number is relatively low compared to the published root dataset. The overlap between the root and the shoot upregulated sets is 58 genes (Figure 5.2 C). Additionally, there are 91 genes uniquely differentially regulated during infection in the shoot compared to root tissue (Figure 5.2 C). Overall, root infection of 24 days post inoculation (DPI), correlates best with 12 DPI shoot infections ($r(8349) = 0.42$, P-Value < .00001, Pearson's Correlation Coefficient). Gene Ontology (GO) enrichment analyses reveal that most upregulated genes are involved in biosynthetic processes, such as carboxylic acid biosynthetic processes, including genes involved in the biotin biosynthesis pathway. Interestingly, there is a total of 23 genes that are antagonistically regulated. GO enrichment analyses predict that these genes are enriched for proteins interacting with the cell membrane (either embedded or attached).

Genes typically not expressed in either root or shoot tissue but turn on over the course of infection are interesting from a biological perspective, such as the well-characterised susceptibility (S) gene *MIOX5* ³⁴⁴, which typically is expressed in pollen ³⁰³, *EXPA8*, which is part of the expansin family, which are known to be specifically upregulated in the syncytium compared to surrounding tissue ³⁴⁵, and two known susceptibility genes, both involved in the B5 vitamin biosynthetic pathway ⁶⁸. Out of the top 20 most upregulated genes, eight are atypical in leaf or petiole expression and usually expressed in either flowers or seeds.

5.6.3 Analysis of the conserved response

From the identified conserved differentially regulated genes, three are known susceptibility genes (Figure 5.4). Various groups are identified in the dataset based on function; a few are illustrated by the STRING network in Figure 5.4. Based on databases of curated biological pathway knowledge (e.g., GO, KEGG, and Reactome) and experimentally determined interactions, a total of six clusters are identified (Figure 5.4).

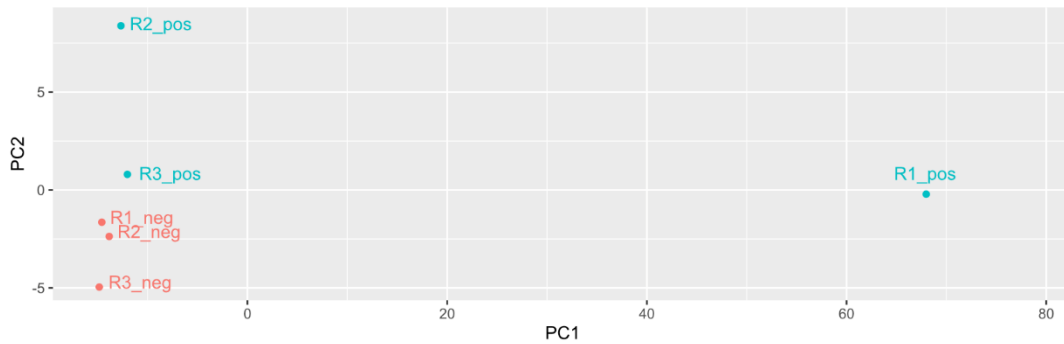
Cluster 1 consists of two genes involved in the B5 vitamin synthetic pathway⁶⁸, cluster 2 is involved in synthesis of biotin, cluster 3 in various parts of cell division, cluster 4 in the cell wall loosening, cluster 5 in seed germination, and cluster 6 contains genes involved in pathogen responses (Figure 5.4 1-6).

One gene was observed in the dataset which are involved in flowering time. Overexpression of *DXPS1* results in the accumulation of gibberellic acid, resulting in early flowering³⁴⁶.

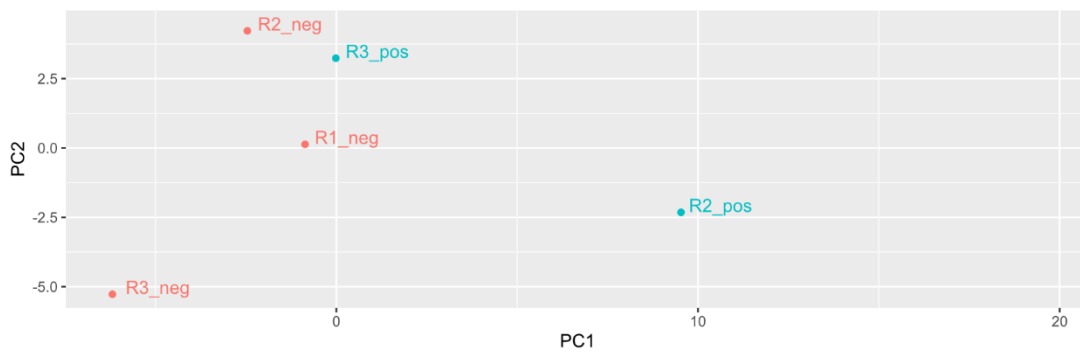
Another observed gene is involved in the Krebs cycle, *MDH2*, which catalyses the conversion of malate and oxaloacetate^{347,348}, which may be linked to the up-regulation of the glutamine synthetase *GLN1-3*, which is associated with a side branch of the Krebs cycle³⁴⁹.

Importantly, some genes that are differentially regulated during infection are typically not expressed in unparasitized tissue. Of the 58 conserved upregulated genes, two genes are typically expressed in the pedicel, 11 genes in roots, eight in seeds, 13 in leaves, 19 in flowers, and the remainder in multiple tissues.

A) Including all data



B) Excluding first replicate



C) Overlap of differential expression between host tissues

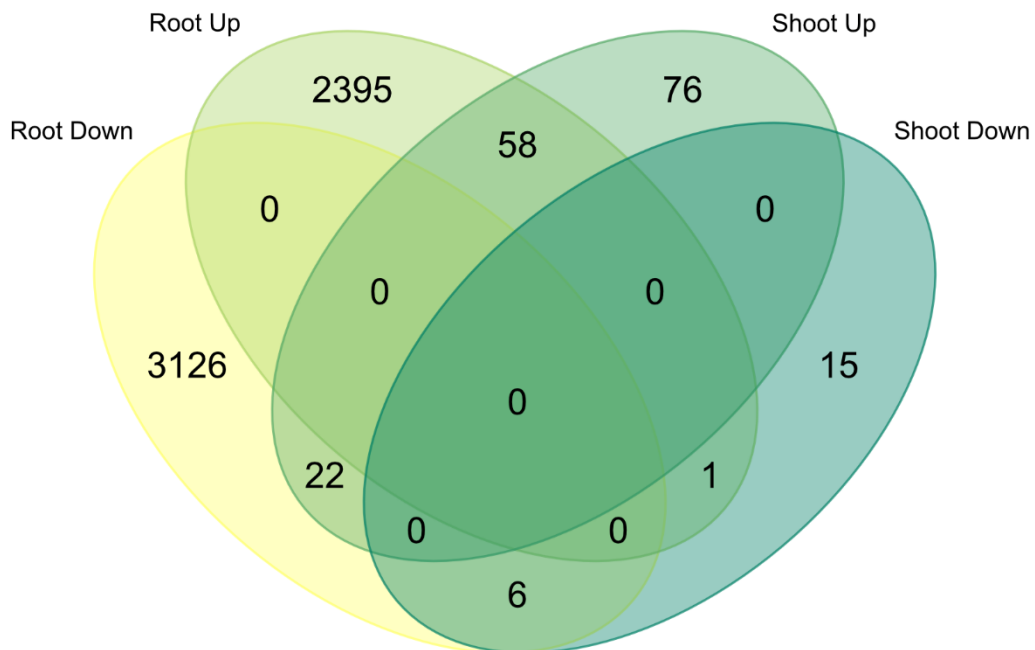
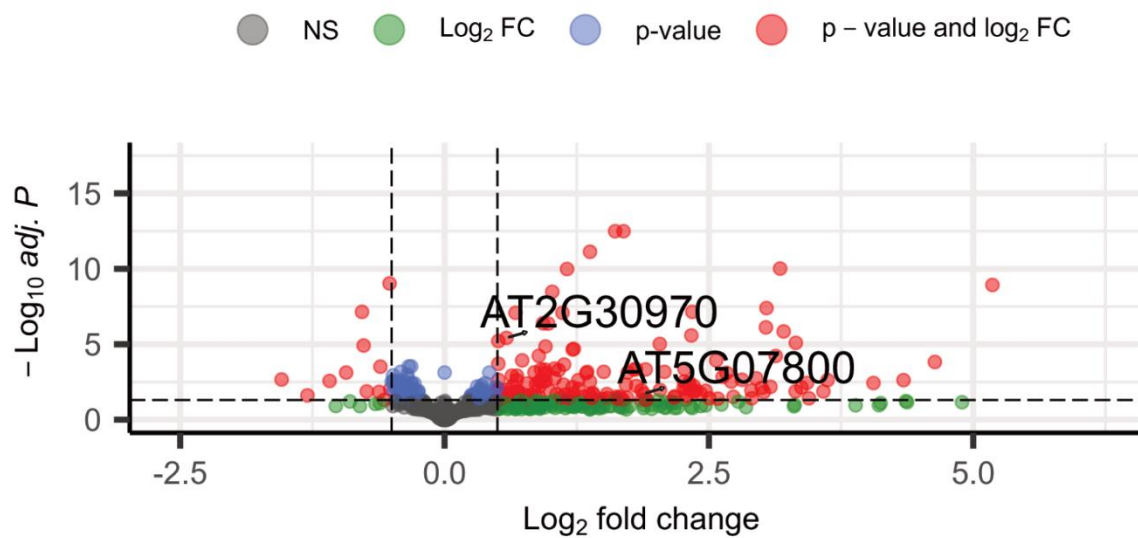


Figure 5.2: Summary of the RNA-sequencing results from shoot infection of *A. thaliana* with *H. schachtii*. A) PCA analysis containing all the technical replicates. One of the replicates accounts for almost all variability in the dataset. B) PCA analysis after removal of the highest variable data point. C) A Venn diagram comparing the observed transcriptional response of shoot infection to root infection. The number of genes that are contained within each quadrant are denoted with numbers.

A) Volcano plot of differential expression analysis aerial infection



B) GO-term analysis plot for conserved differential expression

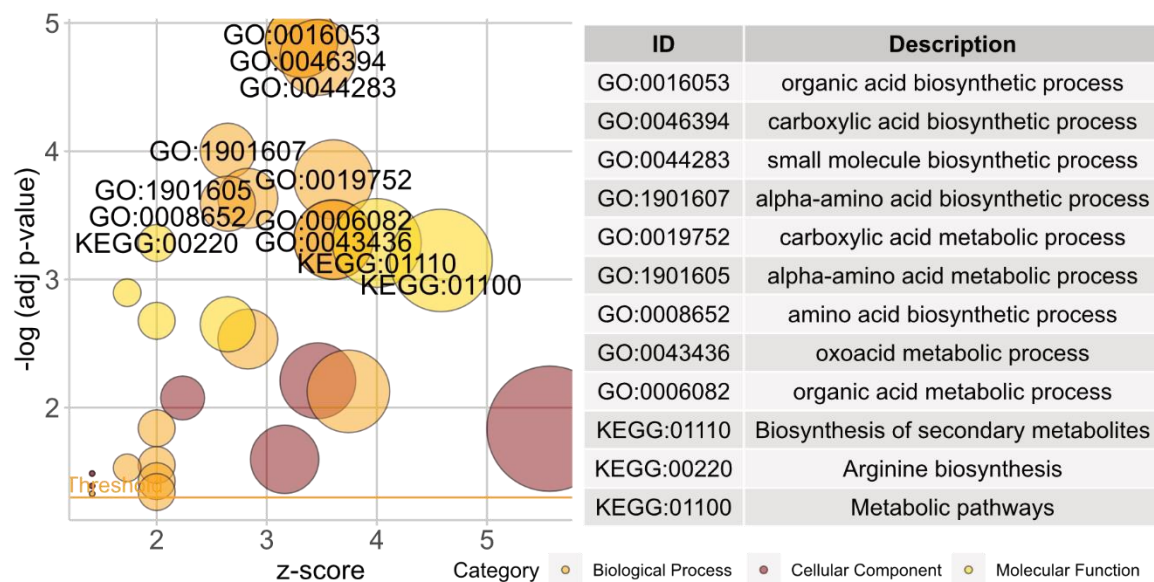


Figure 5.3: Results of RNA-seq analysis visualised. In A) the results visualised as a volcano plot for Log₂FC > +0.5 or < -0.5 and adj. p value < 0.05 in red. Highlighted are genes that are found in subsequent experiments to have significantly reduced nematode infection. In B) the Gene Ontology (GO) terms found for those differentially expressed shown as a go term plot.

There are no obvious patterns or groups present in the downregulated tissue-independent response. However, we do find a conserved downregulation of Transcription factor HHO5, which binds the WUSCHEL (*WUS*) promoter. Additionally, the transcription factor PHL2 is downregulated, which regulates the response to phosphate starvation.

Some genes are antagonistically regulated between tissues. There is one gene, AT4G26950, downregulated in shoot tissue, and upregulated in root tissue, which is a putative regulator for senescence. A larger number of genes are upregulated in shoot tissue, but downregulated in root tissue during infection. This set contains a pectinesterase-like protein (SKS4), pinorensinol reductase (PrR2), which are regulated by various cell wall related transcription factors, PHT1-1, an inorganic phosphate transporter, and HHO3, a transcription factor probably involved in phosphate signalling in roots. The set also contains Extensin-3 (EXT3) involved in strengthening of the primary cell wall, microtubule associated protein 18 (MAP18), which helps determine cell shape, NAC domain-containing protein 87 (NAC87) involved in chlorophyll catabolic processes, and various stress response genes.

While between tissues there is a conserved transcriptional response, there is little overlap between the most re-regulated genes between tissues. Based on top-20 differentially regulated genes, one is conserved for the most up-regulated genes, and none are conserved for down-regulated genes.

Known Interactions

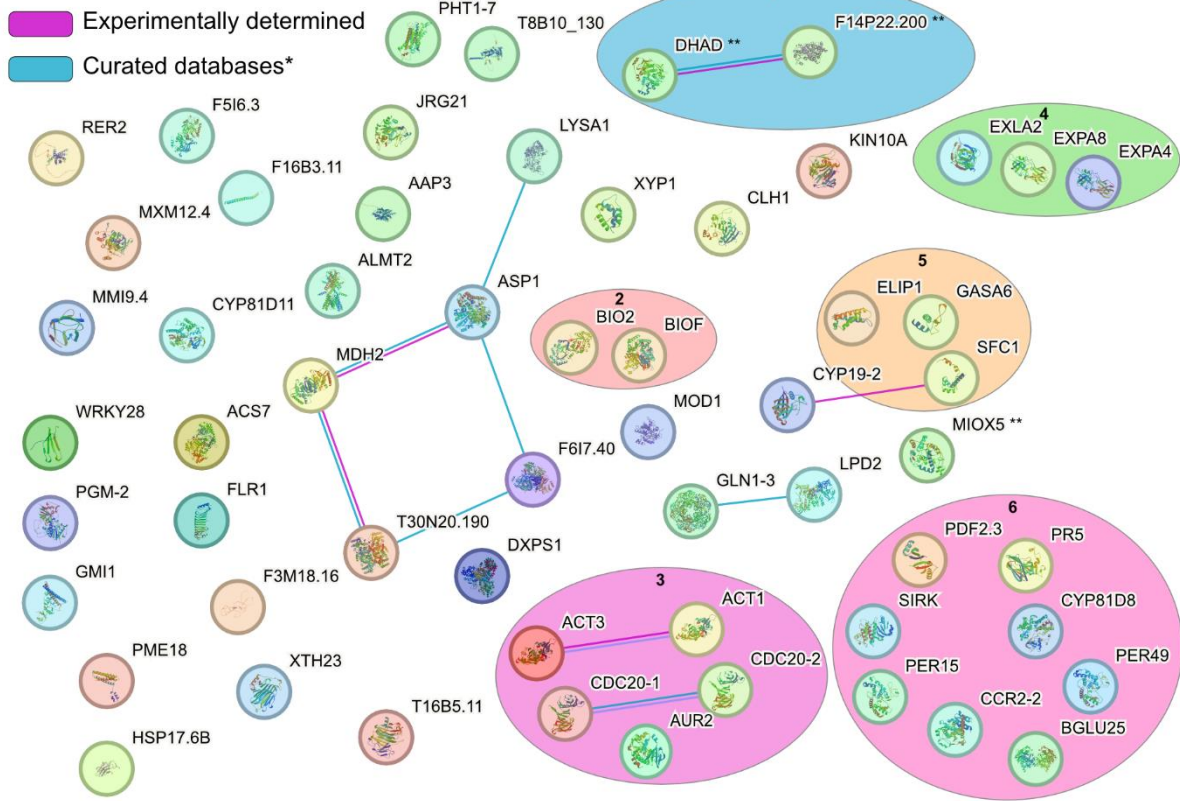


Figure 5.4: A STRING network of conserved upregulated genes during infection. Pink lines indicate experimentally verified interactions between the genes, blue lines indicate predicted interactions based on curated databases such as: Biocarta, BioCyc, GO, KEGG, and Reactome. Known susceptibility genes are indicated with a double asterisk. Experimentally determined indicates either: 1) Experimentally determined (e.g., protein kinase assay, affinity chromatography technology assay, tandem affinity purification assay, etc.); or 2) putative homologs were found interacting in other organisms based on experimental data.

5.6.4 Susceptibility to infection for conserved upregulated genes

A preliminary knock-out mutant screen was performed to determine the importance of a host gene in nematode parasitism. In short, *A. thaliana* is grown for two weeks in axenic culture (N=30) and inoculated with the same number of nematodes between replicates. The infection efficiency is quantified and compared between a knockout genotype (T-DNA SALK line) and a wild-type control (Col-0 CS60000). A reduction in efficiency could be an indication for an S gene. From the available T-DNA mutant lines 18 out of the 58 upregulated genes could be obtained with a potential homozygous knockout mutation for the gene of interest and were preferentially selected for insertions within exons if available. A schematic overview of the genes, and the insertions can be found in Figure 5.5. Small leaf samples were taken from 10 random plants per genotype to confirm the presence of the homozygous mutation.

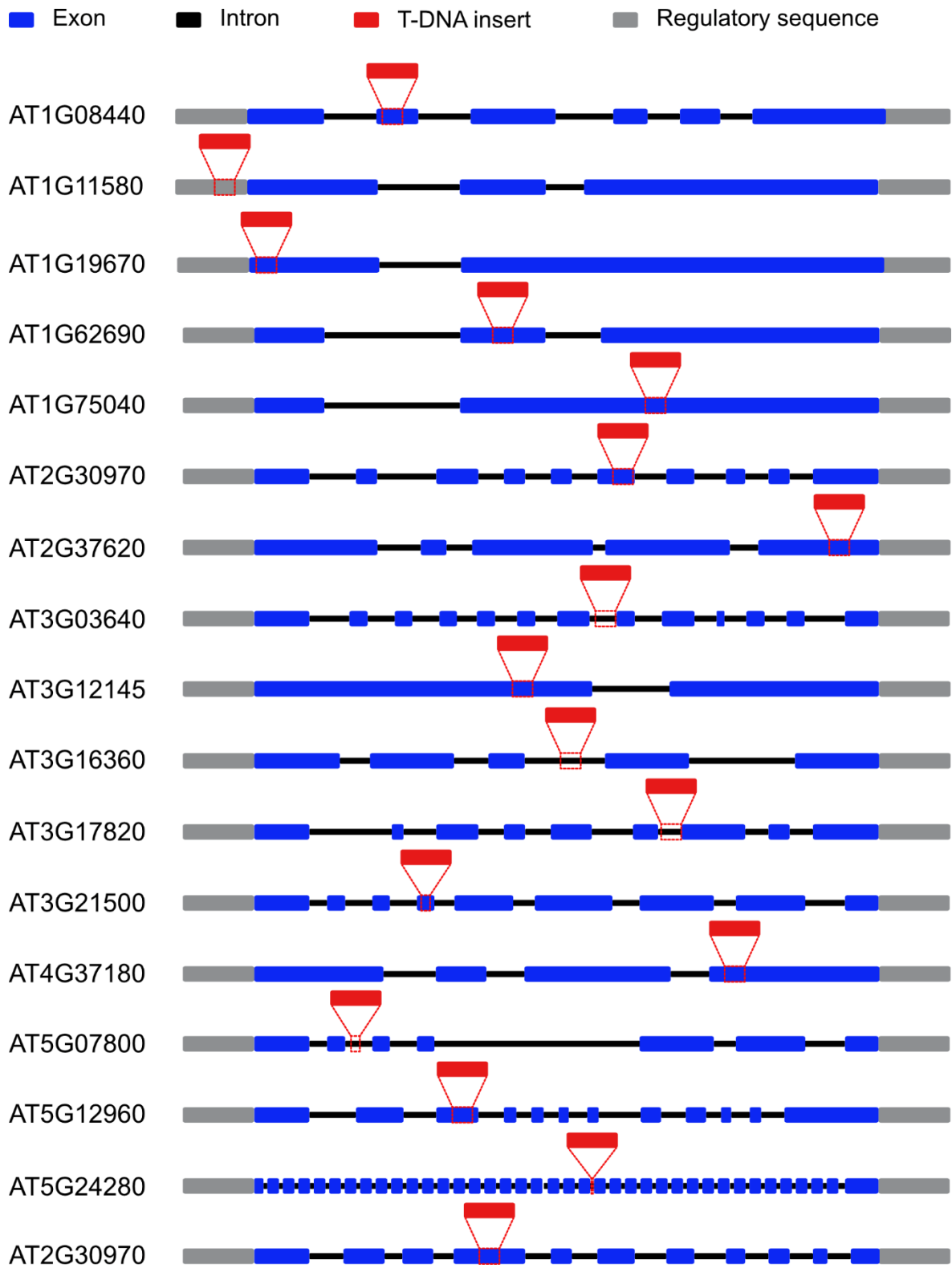


Figure 5.5: A schematic overview of the genes, and the locations of the potential T-DNA insert if present. Regulatory sequences are donated by a 100 bp region upstream and downstream of the gene. Exons and introns roughly represent their real relative size in the diagram and are separated by blue (exon) and black (intron) colours. The T-DNA site is roughly marked with a red marking.

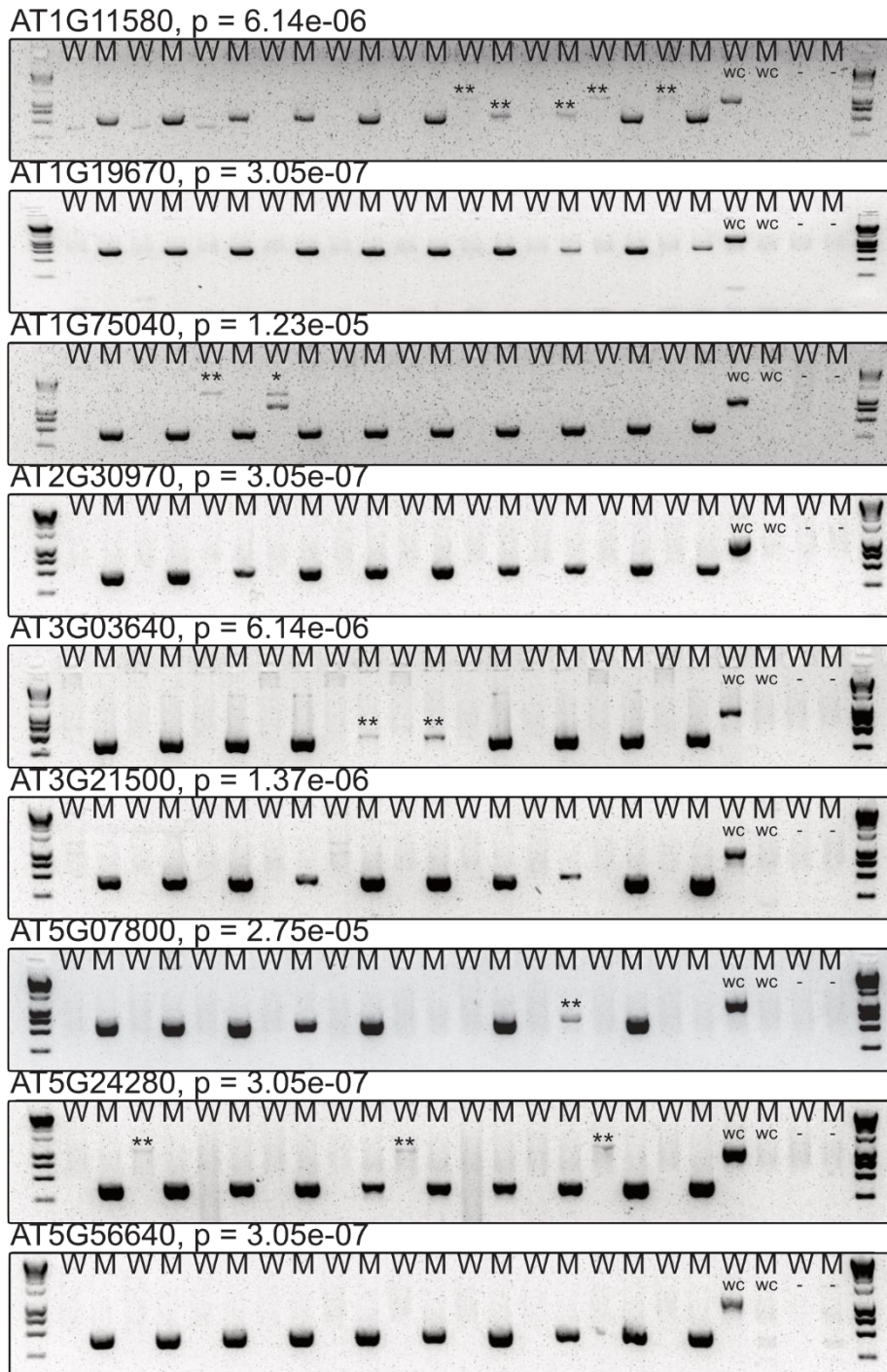


Figure 5.6: Genotyping of the confirmed homozygous lines. An unexpected result is denoted with a single asterisk. This only occurs once and is expected to be due to contamination, indicated by the p-value. A double asterisk denotes a low amplification event and is disregarded for the analysis. The p-value is calculated using a Chi-square test assuming the observed distribution for Mendelian segregation.

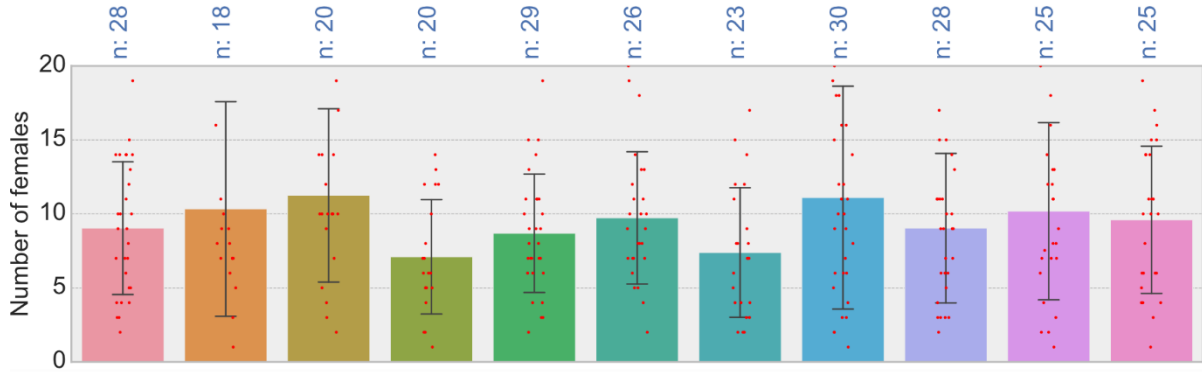
From the tested genotypes, ten are confirmed homozygous (Figure 5.6). The p-value indicates the chance of the observed results based on a Chi-squared test for N = number of amplification events (either WT, MUT or HET), assuming Mendelian segregation.

Two susceptibility parameters were scored: 1) female number; and 2) female size (Figure 5.7 A and 5.8 A). Hatching of the cyst nematode *H. schachtii* can be induced by ZnCl₂ inside specialised hatching jars. We utilise this capacity in the lab to obtain large quantities of J2 nematodes for the infection assays. To obtain enough nematodes for the experiment, two hatching jars were used. In almost all cases, the infection number is higher for plants inoculated with nematodes from hatching jar B (Figure 5.7 B) but seems to have little effect on nematode size (Figure 5.8 B). The Best Linear Unbiased Estimator (BLUE) is used to predict the effect size of the hatching jar and calculate an estimated mean to account for the variability introduced by the hatching jar. The estimated means are compared using Dunnett's test for comparing several treatments with a control (95% family-wise confidence level). A significant reduction in nematode number was found in two genotypes (Figure 5.7 C). A significant reduction in nematode size was not observed.

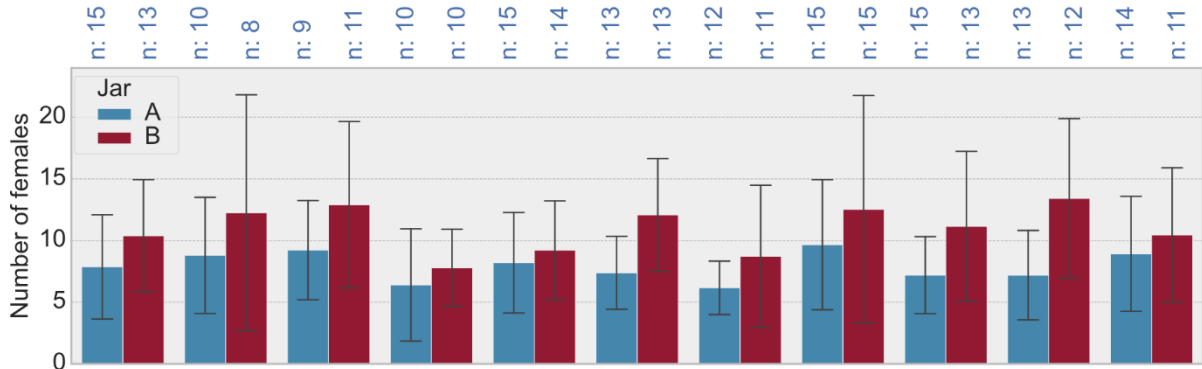
The putative susceptibility gene AT2G30970 encodes for an aspartate aminotransferase 1 and is involved in the reversible conversion of aspartate and 2-oxoglutarate to generate glutamate and oxaloacetate, and plays a role in the regulation of carbon and nitrogen metabolism³⁵⁰.

As of writing, there is not much published about AT5G07800. It is part of flavin-binding monooxygenase family protein, and contains three Pfam domains: 1) a Flavin adenine dinucleotide binding domain; flavin-containing monooxygenase domain, and a Rossmann fold oxidoreductase domain. Based on orthology databases, the function is the catalysation of methylthioalkyl glucosinolates chains³⁵¹.

A) Number of females per replicate



B) Number of females per replicate per hatching jar



C) Estimated mean normalised for hatching jar

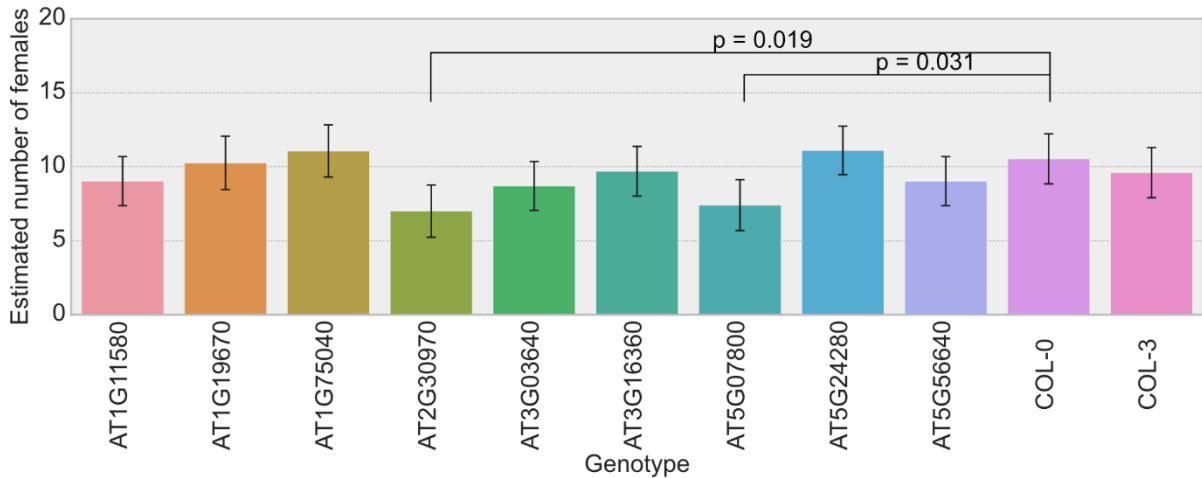


Figure 5.7: The observed number of infecting females per tested genotype. A) The observed number of females per genotype. The number of replicates is denoted above the individual bar graphs. B) The same counts as A, but separated by a hatching jar. The number of replicates is denoted above the bar plots. C) The best linear unbiased estimator (BLUE) means for the number of females per genotype. The genotypes are denoted by their target gene under each bar, and represent all the plots above.

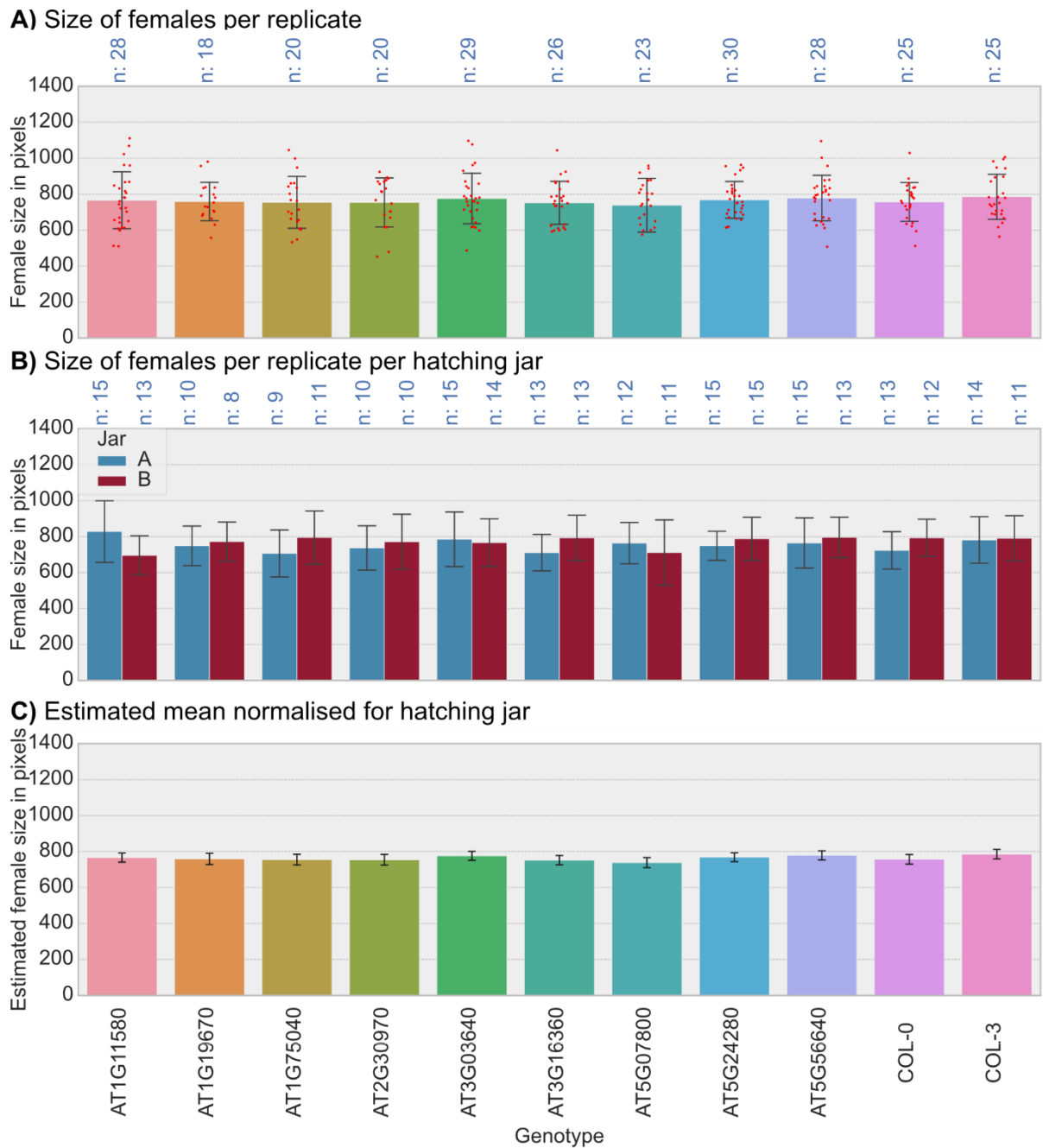


Figure 5.8: The observed female size per tested genotype. A) The observed female size per genotype. The number of replicates is denoted above the individual bar graphs. B) The same counts as A, but separated by a hatching jar. The number of replicates is denoted above the bar plots. C) The best linear unbiased estimator (BLUE) means for the female size per genotype. The genotypes are denoted by their target gene under each bar, and represent all the plots above.

5.7 Discussion

5.7.1 Mapping the transcriptional response to *H. schachtii* parasitism of *A. thaliana* shoot tissue.

The transcriptional response to cyst nematode infection of *H. schachtii* on *A. thaliana* roots is well described. As a result of parasitism, 59 % of *A. thaliana* genes (19,071) are significantly differentially regulated⁶⁸. Knockout mutants of a subset of the genes in this dataset will likely impair nematode parasitism and are, therefore of great interest in the field. The current state-of-the-art screening methods (manual and semi-automatic, as described in Chapter 4) do not allow for rapid enough screening to evaluate all differentially regulated genes without some form of selection (which may introduce bias in some form).

In agriculture, cyst nematodes predominantly parasitise on roots, but will, under favourable conditions, produce functionally equivalent syncytia in shoot tissue³³⁶. It was anticipated that there is a smaller conserved transcriptional response between different tissues than per tissue individually. To map this response, an adequate number of infected shoot samples needed to be collected. While reported feasible in literature³³⁵, a preliminary infection trial proved that shoot infection was far less common than root infection. Importantly, the reported parasitism was on *A. thaliana* Landsberg erecta ecotype. The root transcriptional dataset is based on infection of ecotype Columbia-0. While it is not experimentally validated, it may be that different ecotypes have ranging susceptibility in shoot infection. It is important to compare the same ecotype between the two infection datasets.

Three different set-ups were trialled, infection of: 1) detached leaves; 2) agar-submerged plant shoots; and 3) aerial tissue. All three conditions resulted in parasitism. However, efficiency remained low. Nematodes infecting detached leaves were only observed when the tissue near the leaf petiole was damaged or absent. This suggests that the mechanical disruption of the tissue may have aided in the entry of the nematode into the leaf. Importantly, nematodes appear arrested at a J3 stage¹²⁰. This could indicate inadequate nutrition provided by the syncytium in detached leaves.

Submerged splant shoot infection appears rare (1/48), while aerial infection using a small droplet of inoculum is more common (3/20). Either the inoculum volume or the nematode density appears to play a role in the success rate of aerial shoot infection. Interestingly the addition of 1.5 mM zinc-chloride ($ZnCl_2$), a commonly used hatching inducer of *H. schachtii*, increases the infection rate to ~47 %. Internally we have also observed an increase in motion of second-stage infective juveniles (J2) in the presence of $ZnCl_2$ when compared to water. This may indicate that the compound not only functions as a hatching factor, but also as a nematode stimulant.

Importantly, inoculation of plants with $ZnCl_2$ results in a systemic dark-green / purple phenotype of most of the host shoot tissue, reminiscent of induced anthocyanin production³⁵², which typically accumulates in leaves and stems³⁵³. Particularly in maize, the accumulation of anthocyanin in leaves has been observed under increased levels of zinc content in soils³⁵⁴. Alternatively, high levels of zinc may induce phosphate starvation by inhibition of root-to-shoot translocation of phosphate, which in turn could trigger an immune response leading to anthocyanin accumulation in leaves³⁵⁵.

While clearly not ideal, the increase in infection efficiency with the inclusion of zinc chloride makes the experiment possible. Regardless of the nature of the response, the phenotype is present in both infected and non-infected tissue. Therefore, the comparison between the two tissues should, in principle, still only highlight the transcriptional response of nematode infection. Given the success of the strategy (discussed below) to identify known S genes, it can be reasoned that the approach was not overwhelmingly confounded by this additional phenotype.

Samples were collected of two-week-old, infected shoot tissue. Non-infected tissue from the same plant of the same age was used as a negative control. Transcriptional differential expression analysis highlighted a total of 156 upregulated and 22 downregulated genes. Comparatively to the root dataset (2,454 upregulated, 3,154 downregulated), the overall number of differentially expressed genes is low.

Most of the infected samples collected were of infection on the leaf blade near the base. In this tissue, the syncytium is not visible, and thus the size of the sample surrounding the nematode was chosen broadly to ensure full capture of the syncytium. This inadvertently may reduce the size of infected tissue compared to the overall collected sample. The true transcriptional response may therefore be diluted by expression from uninfected tissue. The result would be that only the most highly differentially expressed genes would be identifiable. Furthermore, one of the replicates was an excessive outlier (alone accounting for >90% of variance between samples) and so was rightly removed but reduced the number of replicates remaining, and therefore the ability to identify differentially expressed genes. It could be that the shoot differentially regulated dataset only includes those with the strongest, and most robust, response. If this experiment were to be repeated, collection of hypocotyl-infected tissue might be desired, as the syncytium can be observed clearly (Figure 5.1 B). Regardless, the shoot infection dataset captures core components of infection illustrated by the presence of three known susceptibility genes. Furthermore, we find common differentially regulated pathways also observed in the independent transcriptional mapping of parasitism in root tissue. Based on this information, we can have good confidence in the dataset.

5.7.2 The tissue-independent response to nematode parasitism

There are four distinct transcriptional groups identified comparing shoot infection to root infection: 1) uniquely upregulated in shoot; 2) conserved upregulated in both shoot and root; 3) uniquely downregulated in shoot; and 4) conserved downregulated in shoot and root.

5.7.2.1 Conserved upregulated

There are genes involved in various pathways and functions observed upregulated during infection in both shoots and roots. Some link well with previously published work, such as the two susceptibility genes: *MIOX5* and a gene involved in the vitamin B5 biosynthesis pathway⁶⁸. We also observe genes involved in biotin synthesis (*BIOF*, *BIO2*) previously observed by Siddique et al. (2022)⁶⁸. Expansins, which are cell wall proteins³⁵⁶, previously found involved in syncytium formation by Wieczorek et al. (2006)³⁴⁵ are also found to be contained in the conserved response.

The conserved response contains two actin genes, *ACT1* and *ACT3*, which are both typically expressed in mature pollen. These genes encode almost completely identical proteins³⁵⁷. Despite this, these two genes lie on chromosomes two and three, respectively and have highly divergent intron and flanking sequences³⁵⁷. Analyses of these 5' flanking sequences revealed a number of short conserved sequences^{357,358}. Together there may be an indication of a conserved regulatory system that the nematode is manipulating.

Two genes of the transducin family proteins are also up-regulated (*CDC20.1* and *CDC20.2*). The anaphase-promoting complex is activated by CDC during early mitosis³⁵⁹, which may be an indication of cells dividing before incorporation into the syncytium³⁶⁰, or may be indicative of hypothesised mitosis within the syncytium³⁶¹. These hypotheses are further supported by the upregulation of *AUR2*, a gene involved in division plane orientation during mitosis³⁶².

One of the biggest clusters of genes found are involved in pathogen/stress responses, such as peroxidases, drought stress-related genes and various cell receptor-like kinases.

The rest of the dataset also highlights possible undermining of the plant's immune system via the upregulation of *MOD1*. This enoyl-acyl carrier protein reductase is involved in the negative regulation of programmed cell death. A deficiency in this gene leads to an accumulation of reactive oxygen species (ROS)³⁶³, resulting in programmed cell death³⁶⁴. The upregulation of this gene may reduce the accumulation of ROS and increase nematode survival chance.

Lastly, we find a conserved response between independent origins of biotrophy. The gene *AAP3* is conserved upregulated during parasitism of *H. schachtii* on *A. thaliana*. The same upregulation is found in parasitism of the root-knot nematode *Meloidogyne incognita*³⁶⁵. Together this indicates a crucial role of amino acid transporters in the facilitation of plant-

nematode parasitism in general. Further analyses of these datasets may reveal attractive targets for broad-range control of PPN.

5.7.3 Conserved downregulated

The subset of downregulated genes is considerably smaller than the upregulated conserved response. We addressed above that the small overall number may result from non-optimal capture of the feeding site, resulting in a relatively large ratio of non-infected and infected tissue. It is possible that downregulated gene analysis is more sensitive to dilution effect.

One of the downregulated genes in this dataset is the transcription factor *HHO5*, which is a repressor of *ULT1*, which is part of the pathway involved in floral meristem homeostasis. The support for interaction in this pathway, however is limited as the Log2 fold change for *ULT1* is only 0.54 ($p = 0.87$). However, *HHO5* is one of the homologues of *HRS1*, which, if overexpressed, hampers the development of syncytia³⁶⁶. It may be worthwhile further investigating these MYB-related transcription factors and their targets for their role in nematode parasitism.

5.7.3.1 Downregulated in roots, upregulated in shoots

An observed difference between syncytia in shoot and root tissue is small ingrowths of the syncytial cell wall between the interfaces of different cell types of neighbouring cells, typically absent in root syncytium³³⁶. Two genes involved in cell wall formation and maintenance are found up-regulated in shoot syncytia but are down-regulated in root syncytia (*PrR2*³⁶⁷, *EXT3*³⁶⁸). The difference in response between the two tissues may play a role in the differentiation of the feeding-site cell wall phenotype observed between the two tissue types.

5.7.4 Screening for susceptibility genes in the tissue-independent response to nematode infection

Typically, candidate susceptibility (S) genes are identified either by the differential regulation of a pathway⁶⁸ or through the magnitude of the re-regulation⁶⁹. However, it is important to note that transcriptional analyses of parasitism do not exclusively highlight S genes. Many physiological and transcriptional alterations happen to the host because of the invading pathogen. Furthermore, an S gene's biological function alone could already be crucial to nematode parasitism, regardless of differential expression. As such, any host gene could be important for nematode parasitism. However, expression magnitude and indicators of involvements in pathways have proven good primers for the identification of S genes.

In a preliminary screen of the conserved transcriptional response to infection, knockout mutants of these three genes result in an overall reduction in the number of infecting females. This could mean that the 'core' of conserved transcription is far more important to nematode

parasitism than previously thought. However, the true causal relationship between a host gene and nematode susceptibility needs to be further confirmed with the complementation of the knockout gene, which may result in a recovery phenotype.

None of the three putative S genes is typically expressed in the same tissue. The gene AT2G30970 may control for aspartate synthesis and may be involved in nitrogen transport ³⁶⁹. Given the current knowledge on these genes, there is too little published information to make a good hypothesis for the role of any of these genes in nematode parasitism.

5.7.5 Limitations in susceptibility screening

To minimise the time needed to perform initial screening for susceptibility genes efficiently, we utilise existing T-DNA mutant libraries. It is important to notice that this does not effectively cover any potential gene redundancy present in the host. Given the time-consuming nature of generating multiple knockout mutants, this is typically not done until later stages (personal communication). Given the above, it is crucial that the initial screen has as little experimental variation as feasibly possible.

Above, we have identified that the 'hatching jar' can play a significant role in nematode infection success. While we can account for these random variables using linear mixed-effects models (LMER), minimising natural variables at an experimental level is more attractive as it better represents the biological difference between the wild-type and the treatment.

A random variable which can't be accounted for using LMER is genetic variation between treatments. *Agrobacterium tumefaciens* T-DNA-induced insertion mutants have been created for almost any gene in *A. thaliana*. The T-DNA mutants screened for susceptibility are at least generation T3 or later, creating a relatively large genetic distance between the mutant and the wildtype control. This is further increased by potential chromosomal rearrangements that could occur in T-DNA mutagenesis ³⁷¹. These genetic differences could account for an increase in experimental variation.

To minimise this genetic distance, segregating T-DNA lines could be screened. Assuming Mendelian segregation, one would expect for 120 plants screened, 30 to be homozygous for T-DNA, 60 heterozygous, and 30 wild type. Through this method, all seeds will have come from the same parent, minimising the genetic variation between the homozygous mutant and the wild type. Furthermore, information would be obtained if susceptibility would behave in a dominant or recessive manner. Using traditional screening methods, in our hands, only 90 plants could be screened per person per day, making the segregating screen prohibitively difficult. However, with the improved screening methods proposed in Chapter 4, 7,248 plants can be screened daily.

Essentially, before genotyping, a distribution is observed based on infection efficiency. Any deviation from a unimodal curve could indicate a change in parasitism success (Figure 5.9). One could analyse the observed distributions and minimise the required genotyping experiments based on curve modality.

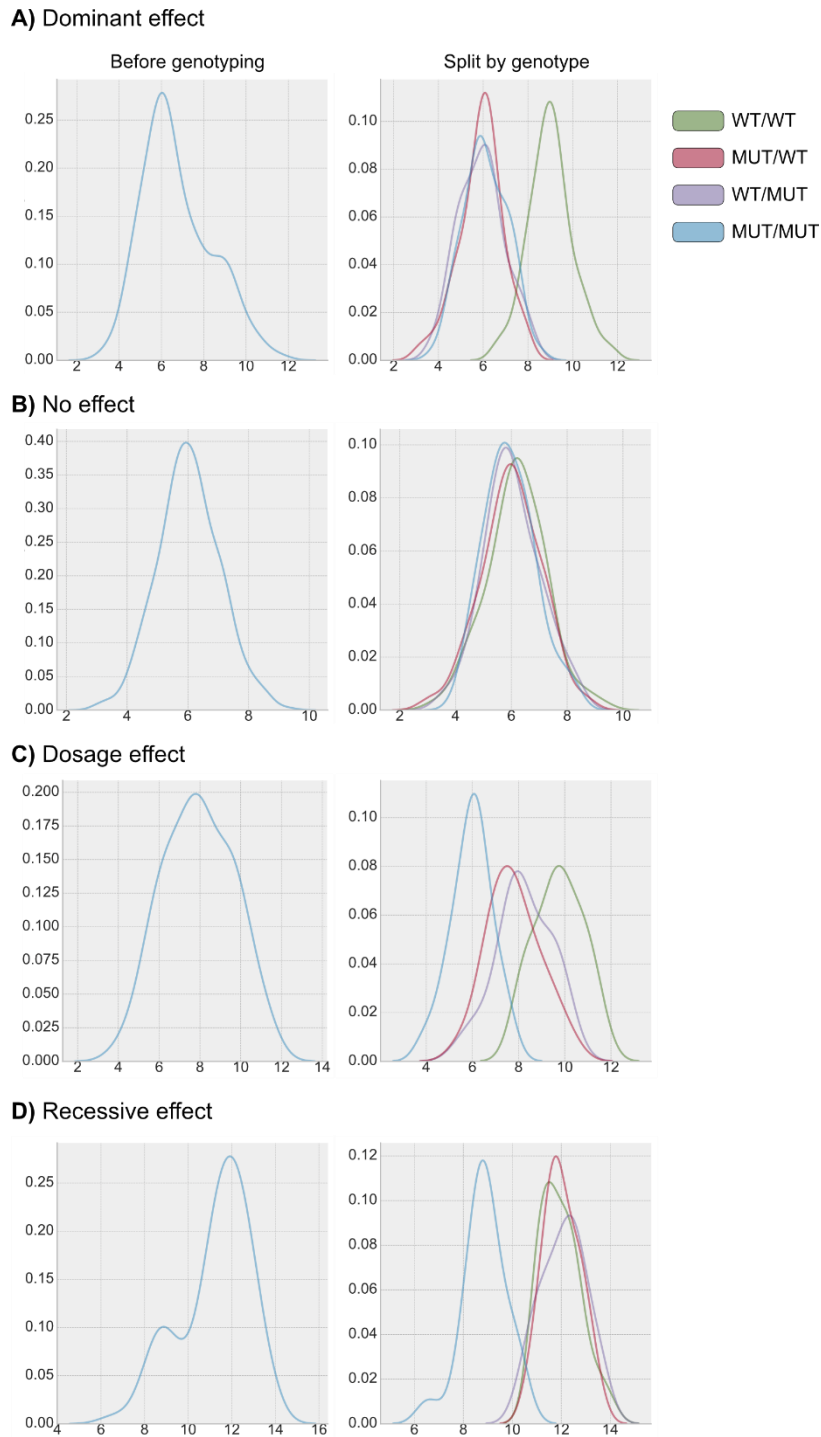


Figure 5.9: A thought experiment for use of segregating lines as a means of reducing the genetic difference between the treatment (T-DNA insertion) and the control (wild type parent). Based on the modality of the distribution one can observe a potential skew before genotyping (left graphs in blue). Three different effects can be observed, a dominant effect (A), no effect (B) and a dosage effect (C) and a recessive effect (D). The left distribution is made up of four smaller distributions containing all possible genotypes. The four smaller distributions can be seen on the right, and reflect the results obtained if genotyping was performed.

5.8 Conclusion

Over the course of the infection of *H. schachtii* on *A. thaliana* 19,071 host genes are differentially regulated. Using an improved shoot infection method, the transcriptional response to nematode parasitism in shoots is now known. We identify core processes involved in nematode parasitism regardless of the parasitised tissue by combining the new and published dataset. Based on a preliminary susceptibility screen, we also identify three new putative S genes.

6 Chapter six - General Discussion

Understanding the relationship between cyst nematodes and their host is difficult. These parasites require adequate equipment to be studied due to their microscopic size, compared to other fields there are relatively few genetic tools available on at least one side of the interaction, and high throughput screening methods are nearly absent. In this thesis we have discussed the first steps towards new tools and techniques to help overcome these limitations. In this final chapter we will discuss other constraints in the field and propose new methods linked to the developed tools in this work, that can help increase the depth of our understanding of nematode parasitism.

6.1 A genetic probe to study the social behaviour of cyst nematodes

Automation of phenotyping as described in this thesis has a major limitation, only one life-stage can be observed. Based on preliminary experiments, males are visible but appear as smudges on these images. They only become distinguishable when the population is observed over time (the smudges move, Figure 6.1-1). Around the tips of new roots J2s can also be observed (Figure 6.1-2). In its current state, the nematode is only observed in favourable conditions (when the background is not too complex). This is an important observation because it shows that there is potential for other life stages than just females to be analysed. However, due to their transparent nature, it is unlikely the current day optics are good enough to observe and track a population of nematodes reliably.

One potential method for visualisation of transparent life stages is the expression of a genetic component that increases their contrast, such as a fluorescent marker. However, the autofluorescence of naturally occurring structures (e.g., plastids or chloroplasts), can overlap with the spectrum of the chosen fluorescent marker³⁷². These structures may then obscure the visibility of the nematode. Methods based on excitation-emission time and signal decay can be used to separate fluorescent signals but are typically only available for high-end confocal microscopes³⁷³.

To circumvent autofluorescence issues all together, a non-fluorescent homolog of GFP could be used. These proteins are responsible for the colours of coral reefs and are referred to as chromoproteins³⁷⁴. Importantly, these proteins, unlike their fluorescent counterparts, absorb visible light, resulting in their distinctive colours under illumination of the visible spectrum. Recent synthetic engineering of chromoproteins has resulted in a palette of seven distinct colours³⁷⁴.

A) *Heterodera schachtii* male



B) *Heterodera schachtii* J2

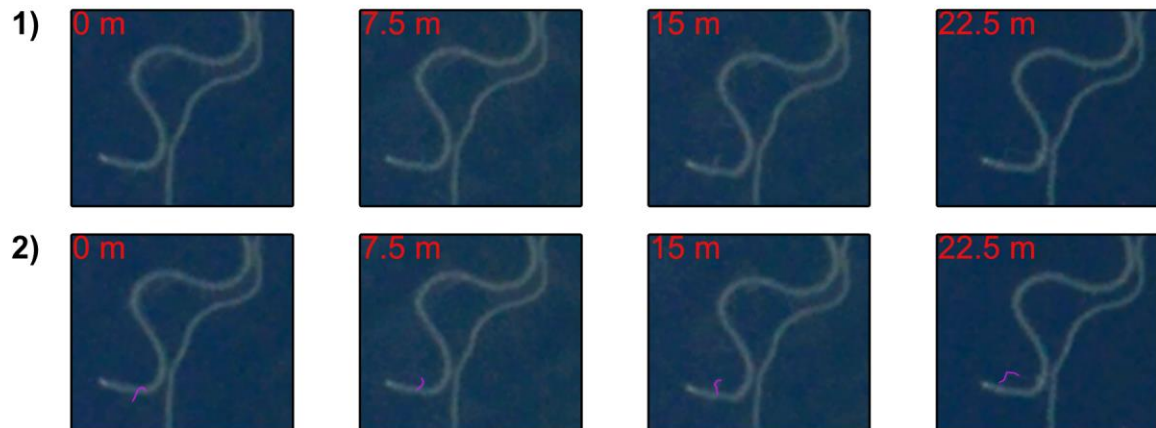


Figure 6.1: Observations of *H. schachtii* males and J2s on petri-dishes with *A. thaliana*. A) the male nematode (indicated with pink line) can be observed as it moves between two females (white globe in top left corner, one off screen). B) The J2 can be seen migrating around the tip of the root. In contrast to the male, the J2 is much harder to see.

Based on a published dataset, there are nematode genes which are uniquely expressed per life-stage⁶⁸. Given the number of synthetically engineered chromo-proteins³⁷⁴, there could be a specific marker for each life-stage. For example, the promoter of J2 specific gene *Hsc_gene_15196* (relative expression J2: 74.9, other life stages: 0⁶⁸), could drive an orange chromoprotein and the promoter of male specific gene *Hsc_gene_19274* (relative expression J2: 74.9, other life stages: 0⁶⁸) can be used to drive a pink chromoprotein. While smaller life-stages will still appear as a smudge on the image, they now have a distinctive colour that can be used to determine their location. If imaged over-time, however, we gain a new insight on nematode dynamics.

Based on personal observations, male nematodes sometimes swarm a single female, while others appear to be ignored. This could indicate that some females attract more males, a female becomes more attractive while mating, or that females become unattractive after they have been mated with. To elucidate the exact nature of mating of *H. schachtii* we could use the combination of the existing computer vision algorithm to locate females (unpublished) and use a new tracking method combined with chromoprotein expressing males to map the dynamics over time. Furthermore, if we can track J2s we could potentially determine from which parent the nematode hatched, allowing us to investigate dynamics at a population level.

6.2 A fingerprint for syncytia, the where and the when

As mentioned above, female nematodes can be automatically identified from images using artificial intelligence. There is scope to expand this to other life stages using various genetic markers. However, structures associated with nematode parasitism in the host are not identified as easily.

Syncytia are unique. The structure, function and gene expression patterns are unlike any organ normally found in plants. A closer look at the infection data reveals that genes are expressed in non-typical tissue (such as a flower gene expressed in the root)⁶⁸. Combinations of these differentially expressed host genes define a unique genetic 'fingerprint' of parasitism, highlighting nematode-responsive promoters. As shown by Phillip *et al.* these promoters can be used to drive multi-component systems to express exogenous genes induced by nematode parasitism, such as β -glucuronidase (GUS) or cytotoxic genes to disrupt nematode development³⁷⁵. A conditional expression system like this may also be used to uniquely highlight syncytia.

Cre recombinases are tyrosine site-specific enzymes, originating from the bacteriophage P1^{158,376}. Two loci of \times over P1 (*loxP*) sequences flanking a gene of interest are recognised by the recombinase, which could lead to deletion, inversion or translocation of the genetic sequence between the two sites, termed *loxP* flanked (floxed) DNA^{158,377,378}. Temporal control

in this system can be achieved via chemically inducible promoters such as tetracycline or tamoxifen^{158,379–382}, or through deactivation of a Cre blocker using UV light³⁷⁷. The system may also be controlled via fusing of the Cre recombinase gene to a tissue specific promoter³⁸³.

The split-Cre system is a two-component version of a Cre recombinase. This can be used to express two inactive fragments controlled under two separate promoters. Only if the two fragments are expressed in the same cell at the same time a functional Cre can be formed³⁸⁴.

To only express a marker in syncytia, one would need two promoters that are mutually exclusive in expression (never on in the same tissue in nature), and are ideally never expressed in the root (to avoid leakiness of the two-component expression). The system could then be used to activate expression of a marker gene³⁸⁵, e.g., a chromo or fluorescent protein. This would highlight the syncytium with a unique colour that could be separated using computer vision.

Furthermore, the exact same system may be used to differentiate between male and female syncytia. For example, *AT1G35750* is only expressed during female infection in roots, and is typically expressed in the 1st internode, and *AT2G38910*, typically only expressed in mature flowers⁶⁸. For males, *AT1G52940* and *AT2G04420*, which are typically only expressed in mature flowers and leaves respectively, get uniquely up-regulated during male parasitism. The expression of the above-mentioned genes, however, is relatively low. An additional signal enhancing logic component may be needed for adequate expression of the marker.

The system could be constructed as follows: In short, two promoters can be used to conditionally express Cre in the syncytium (Figure 6.2 A). The Cre has two functions: 1) re-orientate an inverse Cre gene to act as a signal enhancing component (Figure 6.2 B), and 2) re-orientate an inverse reporter gene (Figure 6.2 C).

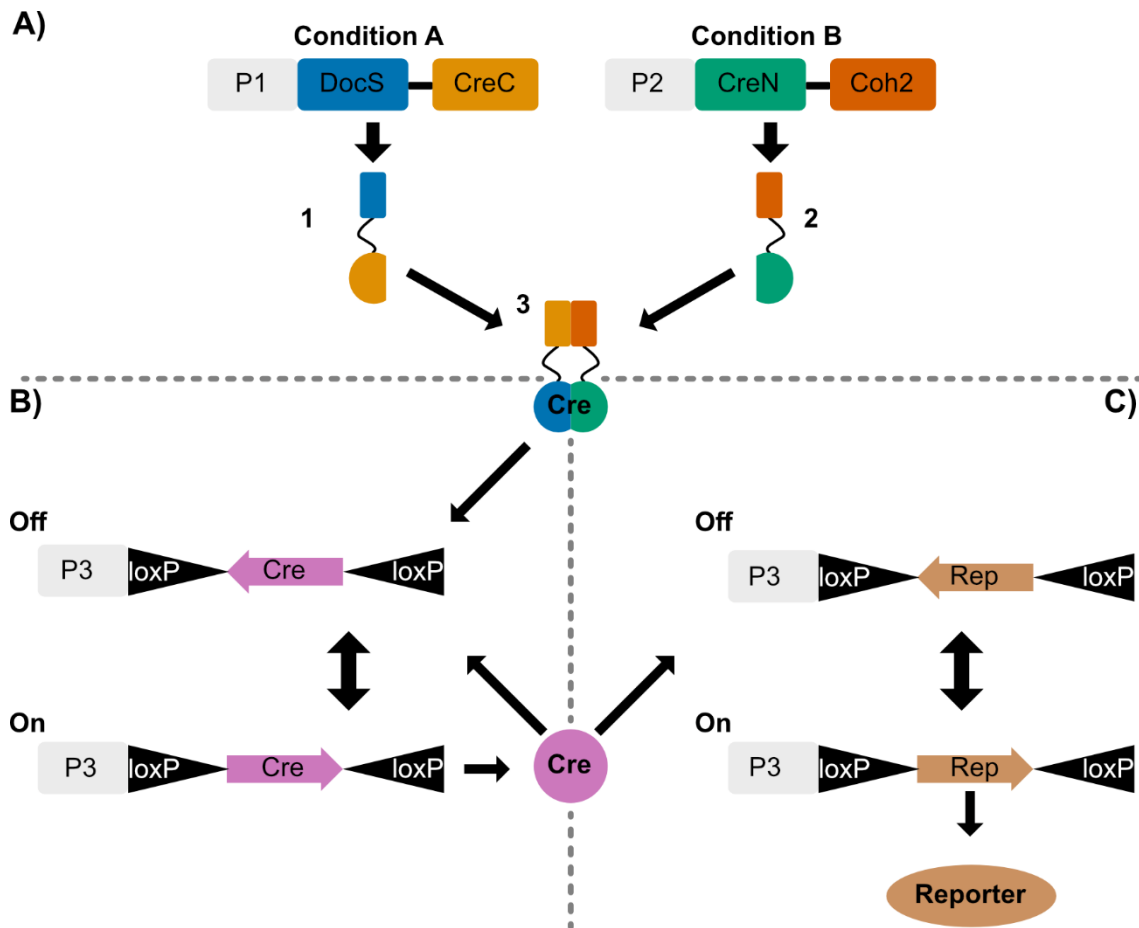


Figure 6.2: Adapted and adjusted from Wu et al. (2020)³⁸⁶. A two component system to induce marker gene expression in nematode syncytia. A) The two components of Cre are driven by two different promoters. Only if both are expressed, a functional Cre can be formed. B) The functional Cre is able to reverse and invert Cre gene, thus activating the expression resulting in an increase of overall Cre. C) Cre can also target and reverse an inverse marker gene, resulting in highlighting of the syncytia.

Once the signal enhancing component is activated, it will be controlled under a highly expressed gene promoter during infection, e.g., *AT1G12940* in females and *AT1G62510* in males (both highly expressed during infection, and typically not in roots) ⁶⁸. It is important to note, signal enhancing introduces leakiness to two-component systems. It is therefore expected that many different promoter combinations need to be tested, and that these type of circuits in this proposed form only work in a controlled laboratory environment which minimises undesired expression of control genes.

6.3 Screening parasitism genes through induced knockouts

In this thesis we describe the first steps towards transient expression in PPN. It is expected that this will eventually lead to stable transgenics including the ability to generate gene knockout mutants using tools such as CRISPR-Cas9 mutagenesis.

From the perspective of control, the most interesting nematode genes to study are parasitism genes. As demonstrated by Yadav *et al.* (2006), RNA interference (RNAi) knock-down of nematode genes is achievable through delivery of dsRNA originating from the host ⁹⁰. This can lead to almost complete depletion of target mRNA in the nematode. However, RNAi only requires 80% similarity with a target sequence to function ³⁸⁷, which could lead to an increase in off-target effects for both the host and the parasite. In a complex interaction such as PPN parasitism, unknown factors will massively complicate assessment.

A better way of studying gene function is by utilising a homozygous knockout, linked to a phenotype to indicate gene function. A homozygous knockout for a parasitism gene, however, would likely prevent the nematode from completing its lifecycle, making generation of a stable knockout population impossible.

The section above describes an example of inducible gene expression using the Cre lox system. Using the same technique, conditional knockouts for a gene of interest can be created ³⁸⁸. In short, a gene of interest is flanked with two *loxP* sites in the same orientation (floxed gene). These sites can be recognised by a conditionally expressed Cre recombinases, resulting in excision of the gene of interest. Importantly, in the absence of the Cre recombinase, the gene remains functional ³⁸⁸. Using this system, homozygous populations for floxed genes of interest could be generated, and the knockout could be induced during nematode parasitism, allowing for study of function of the parasitism gene.

6.4 Is susceptibility the right proxy for control?

In the field of plant parasitic nematology there is great interest in susceptibility genes^{68,69}. The potential to generate plant genotypes that are simply not-or-less susceptible to nematodes is appealing. Additionally, loss of susceptibility has been shown to be a more durable control measure than resistance in agriculture^{389,390}. However, a reduction in susceptibility is not equal an improvement in yield. Therefore, direct deployment of a knockout mutant of a susceptibility gene based on reduction in nematode parasitism may be prudent.

Yield in relation to nematode parasitism is closely linked with the concept of tolerance. In short, damage is dependent on: 1) nematode density; 2) nematode species; and 3) host genotype⁷⁰. The lowest nematode density for the first observable impact to the host is called the tolerance limit. It is crucial in a field to keep the nematodes below this damaging threshold to minimise yield loss. If a host lacking a susceptibility gene is deployed in the field where nematodes are already present in high numbers, then the reduction in infection may not be enough to reduce the nematode number under the damage threshold (Figure 6.3 B). A good loss of susceptibility line would over time decrease the nematode population in the field (Figure 6.3 C).

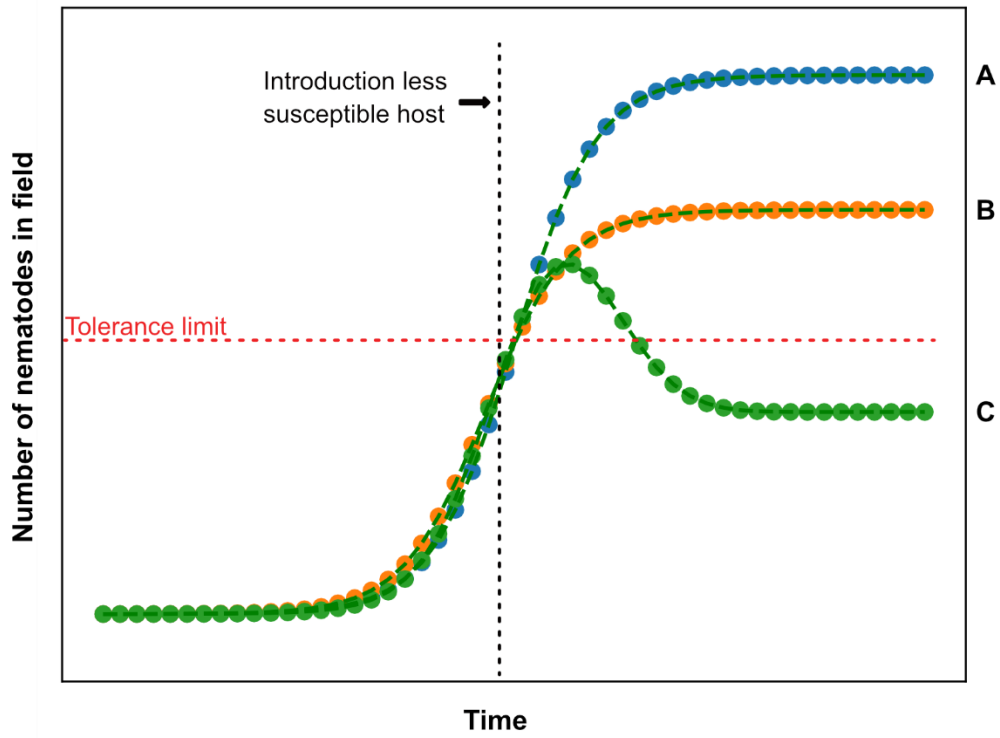


Figure 6.3: Thought experiment for number of nematodes in the field as a function of time for a given genotype of crop grown. A) is a susceptible host, B) is a host lacking a susceptibility gene, and C) is a non-susceptible host.

It is important to note that currently the only widely used parameter for impact of the population is egg count ⁶⁹, which may be an indicator of the effect on a population. A better study, with the focus of application in the field, would measure susceptibility over multiple generations. It may be that a single loss of susceptibility mutant is not enough to cause a reduction in nematode population. Stacking of multiple knockouts for susceptibility genes may be required to achieve this goal.

6.5 General conclusion

Biology is a rapidly evolving field. As shown in this thesis, there is good scope to adopt methods used to study other biological systems to plant-parasitic nematodes. It will be important for the field to adapt and develop these methods as a community to increase our understanding of nematode parasitism at a more rapid rate.

7 Appendix

Computer code 4.1: A Powershell language script that converts BMP to PNG. The converted images are then copied from 6 independent USB sticks to three hard drives independently. Code adapted and adjusted from Chad Miller

```
### making backup using robocopy and then mirroring to different disks
$Day = "{0:yyyy-MM-dd}" -f (get-date)

[Reflection.Assembly]::LoadWithPartialName("System.Windows.Forms") | Out-Null

### conversion function ###
function ImageRename{
    param ([string]$path)
        $path = $usb

foreach ($path in $paths) {

Get-ChildItem -File "$path\*.bmp" -Recurse | ForEach-Object {

$imageRead = [System.Drawing.Bitmap]::new($_.FullName)

$changeExtension = $_.FullName -replace '.bmp$', '.png'

$imageRead.Save($changeExtension, "png")

}};

### list of usbs to process ###
$usb1 = 'U:'
$usb2 = 'F:'
$usb3 = 'H:'
$usb4 = 'J:'
$usb5 = 'K:'
$usb6 = 'I:'

$usblist = $usb1,$usb2,$usb3,$usb4,$usb5,$usb6
```

```

foreach($usbs in $usblist){
$usb = $usbs
##### convert #####

ImageRename -path $usb

Start-Sleep -Milliseconds 1000

##### back up #####

Measure-Command { Robocopy /z /r:3 /w:3 /E "$usb" "U:$Day" *.bmp /S |Out-Null| Out-
Default }
Measure-Command { Robocopy /z /r:3 /w:3 /E "U:$Day" "X:$Day" *.bmp /S |Out-Null| Out-
Default | Out-Null }
Measure-Command {Robocopy /z /r:3 /w:3 /E "U:$Day" "Y:$Day" *.bmp /S |Out-Null| Out-
Default | Out-Null}

}

```

Computer code 4.2: QR code information was directly read from the image and the results was added to the name of the file. Finding a QR code in a complex image remains challenging. The code first utilised various methods to find the QR code. If found the text within the QR code was stripped from any illegal characters, and the result was added to the name of the file.

```

### snippet partially from Jie to find QR code location, and isolate it. Siyuan and Sebastian
made a part of the renaming script.
# make list of dirs you want to process.
dirs = [r'W:\Olaf\SegregatingBasedOnLeafInfection']
import time
import random

random.shuffle(dirs)
start = time.time()
# General libraries
import os
import cv2 as cv2

```

```

import numpy as np
import math
from scipy import ndimage as ndi

# QR Code reading
from pyzbar.pyzbar import decode

# Packages for image processing
from skimage import io, color, data, measure
from skimage.measure import regionprops
from skimage import exposure
from skimage.transform import rotate, hough_circle, hough_circle_peaks, rescale, resize
from skimage.filters import threshold_otsu
from skimage.util import img_as_ubyte
from skimage.morphology import binary_dilation, disk, binary_erosion, convex_hull_image,
erosion
from skimage import util
from skimage.morphology import remove_small_objects, remove_small_holes
from skimage import draw
from skimage.draw import circle_perimeter
from skimage.segmentation import clear_border
from skimage.filters import gaussian, unsharp_mask, threshold_local
from skimage.exposure import match_histograms

# Packages for displaying step result
import matplotlib.pyplot as plt
import matplotlib.patches as mpatches
import multiprocessing as mp
import warnings
warnings.filterwarnings("ignore")

'''
hsv based detection, return a binary mask
'''

def get_mask_hsv(image):

```

```

hsv = cv2.cvtColor(image,cv2.COLOR_BGR2HSV)
low_hsv = np.array([0,0,0],dtype = np.uint8)
upper_hsv = np.array([180,255,46],dtype = np.uint8)
mask = cv2.inRange(hsv,low_hsv,upper_hsv)

return mask

'''
Detect the petri dish, using mask instead of an RGB image to speed up the analysis
'''

def get_circle_mask(mask):

    # Modify the input mask
    mask1=binary_dilation(mask,disk(2))
    reserve_mask=util.invert(mask1)

    # label objects
    label_mask,num=ndi.label(reserve_mask)
    regions=regionprops(label_mask)

    # Find the petri disk object
    circle_mask=np.zeros(mask.shape).astype('int')
    max_region=0
    for region in regions:
        if region.area>max_region:
            max_region=region.area
            coords=region.coords

    circle_mask[coords[:,0],coords[:,1]]=1
    # get rid of small holes in the petri dish
    circle_mask=remove_small_holes(circle_mask,20)

    return binary_erosion(circle_mask,disk(3))

'''

```

```

Detect the petri dish mask, which shall be a circle
'''

def get_final_circle_mask(circle_mask):

    # Find edge mask use a morphological operation
    edges = np.logical_xor(circle_mask, binary_erosion(circle_mask, disk(2)))

    # set the radius of a circle
    # hough_radii = np.arange(1000, 1500, 10)
    hough_radii = np.arange(100, 150, 1)

    #hough circle detection
    hough_res = hough_circle(edges, hough_radii)
    accums, cx, cy, radii = hough_circle_peaks(hough_res, hough_radii, total_num_peaks =
1)
    # print(cx, cy)
    img_circle = np.zeros(circle_mask.shape)
    # detect a suitable circle object
    for center_y, center_x, radius in zip(cy, cx, radii):
        if radius>50:
            r, c = draw.disk((center_y, center_x), radius - 2)
            # print(min(r))
            draw.set_color(img_circle, [r, c], [1])

    return img_circle

'''
Display function for testing
'''

def display_object_from_original(img, label_img):

    mask = label_img > 0

    r = img[:, :, 0] * mask

```

```

g = img[:, :, 1] * mask
b = img[:, :, 2] * mask

img_temp = np.dstack([r, g, b])

return img_temp

"""
Rotate the image for automated trait analysis
"""

def rotate_image(image, angle):
    # use rotation matrix to fit the perti dish image
    image_center = tuple(np.array(image.shape[1::-1]) / 2)
    rot_mat = cv2.getRotationMatrix2D(image_center, angle, 1.0)
    result = cv2.warpAffine(image, rot_mat, image.shape[1::-1], flags=cv2.INTER_LINEAR)

    return result

"""
Adjust the image contrast and brightness for automated trait analysis
"""

def change_brightness(img, value=30):

    hsv = cv2.cvtColor(img, cv2.COLOR_BGR2HSV)
    h, s, v = cv2.split(hsv)
    v = cv2.add(v,value)
    v[v > 255] = 255
    v[v < 0] = 0
    final_hsv = cv2.merge((h, s, v))
    img = cv2.cvtColor(final_hsv, cv2.COLOR_HSV2BGR)

    return img

"""

```

Use exposure.adjust_gamma function for adjusting brightness

'''

```
def get_QRCode_use_exposed_method(img):
```

```
    for z in range (180):
```

```
        qrCodeDetector = cv2.QRCodeDetector()
```

```
        exposed_img = exposure.adjust_gamma(img, 0.3)
```

```
        rotated = rotate_image(exposed_img, z)
```

```
        rotated_ori_img = rotate_image(rotated, z)
```

```
        decodedText, points, _ = qrCodeDetector.detectAndDecode(rotated_ori_img)
```

```
        if decodedText != " or z > 90:
```

```
            break
```

```
    return z, decodedText, points
```

'''

Use cv2.convertScaleAbs function QR code adjustment

'''

```
def get_QRCode_use_convertScaleAbs_method(img):
```

```
    for z in range (90):
```

```
        qrCodeDetector = cv2.QRCodeDetector()
```

```
        alpha = 10 # Contrast control (1.0-3.0)
```

```
        beta = 0 # Brightness control (0-100)
```

```
        adjusted = cv2.convertScaleAbs(img, alpha=alpha, beta=beta)
```

```
        rotated = rotate_image(adjusted, z)
```

```
        # Detect QR code
```

```
        decodedText, points, _ = qrCodeDetector.detectAndDecode(rotated)
```

```
        if decodedText != " or z > 5:
```

```

        break

    return z, decodedText, points

'''
Clear image border
'''

def get_the_black_part(img):

    hsv = cv2.cvtColor(img,cv2.COLOR_BGR2HSV)
    low_hsv = np.array([0,0,0],dtype = np.uint8)
    upper_hsv = np.array([180,255,46],dtype = np.uint8)
    mask = cv2.inRange(hsv,low_hsv,upper_hsv)
    img_border_mask = clear_border(mask)

    return img_border_mask

'''
Clear image border
'''

def remove_the_border_black_part(mask):

    label_blob,num=ndi.label(mask)
    regions=regionprops(label_blob)
    result=np.zeros(mask.shape)

    for region in regions:
        perimeter=region.perimeter
        area=region.area
        diameter=region.equivalent_diameter
        pi = math.pi
        radio=perimeter*diameter/area
        minr, minc, maxr, maxc = region.bbox
        roundness = (4*pi*area)/(perimeter*perimeter)

```

```

# Hard coded, which will be replaced based on image resolution
if(100<area<8000 or area>40000):
    coords=region.coords
    result[coords[:,0],coords[:,1]]=1

return result

'''
Remove the QR code from the image
'''

def get_the_qr_hull(img, mask):

    img_ersion = binary_erosion(mask, disk(5))
    final_result = remove_small_objects(img_ersion, 200)

    hull_mask = convex_hull_image(final_result)
    invert_qrcode = util.invert(hull_mask)
    img_remove_qrcode = display_object_from_original(img, invert_qrcode)

    return hull_mask, img_remove_qrcode

# Read data from the QR code

def get_the_info_of_QRcode(mask, img):

    label_image_of_qrbg = measure.label(mask)

    for region in measure.regionprops(label_image_of_qrbg):
        # ignore small areas
        if region.area < 100:
            continue

        # get the bbox of the object
        minr, minc, maxr, maxc = region.bbox
        qrbg_only = img[minr-100:maxr+100, minc-100:maxc+100]

```

```

# Display the QR code only image

# Read information
z, decodedText, points = get_QRCode_use_convertScaleAbs_method(qrbg_only)
if decodedText == "":
    z, decodedText, points = get_QRCode_use_exposed_method(qrbg_only)

return decodedText

'''
Start reading an input image
'''

def rename_file(filename):
    print('the file name: '+ filename)

    try:
        test_img = io.imread(filename)
        path_bit = '\\'.join(filename.split("\\")[:-1])
        oldfilename = filename
        oldfilename = oldfilename.split("\\")[-1]
        filename_split = oldfilename.split("\\")[-1]
        #try:
        img_rescale = rescale(test_img, 0.1, multichannel=True)
        img_rescale = img_as_ubyte(img_rescale)
        img_remove_black_part = get_mask_hsv(img_rescale)
        img_circle_mask = get_circle_mask(img_remove_black_part)
        img_final_circle_mask = get_final_circle_mask(img_circle_mask)

        # All the image shall be resized to the following resolution
        # as the deep learning model and feature selection in the program based pixel-based
        final_circle_mask = resize(img_final_circle_mask, (3040, 4056),
                                anti_aliasing=True)
        dish_of_the_img = display_object_from_original(test_img, final_circle_mask)
        img_black_part = get_the_black_part(dish_of_the_img)

```

```

img_get_the_remove_border = remove_the_border_black_part(img_black_part)
    qqr_hull_mask, img_remove_qrcode = get_the_qr_hull(dish_of_the_img,
img_get_the_remove_border)
qr_info = get_the_info_of_QRcode(qqr_hull_mask, test_img)
print(qr_info)
qr_info = qr_info.replace("'", "") ## this is to remove illegal characters from filename
qr_info = qr_info.replace("\n", "") ## this is to remove illegal characters from filename
if (len(qr_info)) > 0:
    os.rename(path_bit+"\\"+filename_split, path_bit+"\\"+qr_info+'_'+filename_split)
    outputdata = oldfilename + ".t" + qr_info
    print(outputdata)
    return outputdata
else:
    #test_img = io.imread(filename)
    path_bit = "\'.join(filename.split("\\"[:-1])
    oldfilename = filename
    oldfilename = oldfilename.split("\\"[-1]
    filename_split = oldfilename.split("\\"[-1]
    os.rename(path_bit+"\\"+filename_split, path_bit+"\\"+'failed'+ '_' +filename_split)
    outputdata = path_bit+"\\"+'failed'+ '_' +filename_split
    print('failed')
    return outputdata
except Exception as e:
    print(e)
    try:
        #test_img = io.imread(filename)
        path_bit = "\'.join(filename.split("\\"[:-1])
        oldfilename = filename
        oldfilename = oldfilename.split("\\"[-1]
        filename_split = oldfilename.split("\\"[-1]
        os.rename(path_bit+"\\"+filename_split, path_bit+"\\"+'failed'+ '_' +filename_split)
        outputdata = path_bit+"\\"+'failed'+ '_' +filename_split
        print('failed')
        return outputdata
    except:
        path_bit = "\'.join(filename.split("\\"[:-1])

```

```

oldfilename = filename
oldfilename = oldfilename.split("\\")[-1]
filename_split = oldfilename.split("\\")[-1]
print('COULD NOT READ IMAGE, LABELING AS CORRUPTED')
os.rename(path_bit+"\\'+filename_split,
path_bit+'\\'+CORRUPTED'+_' +filename_split)

list_of_pngs = []
for work_dir in dirs:
    print(work_dir)
    list_of_pngs = []
    os.chdir(work_dir)
    for root, dirs, files in os.walk(work_dir):
        for file in files:
            if file.endswith(".bmp") or file.endswith(".png"):
                rel_dir = os.path.relpath(root, work_dir)
                #input()
                #print(rel_dir)
                if ',' in file or 'failed_' in file or 'CORRUPTED' in file or ';' in file or ':' in file:
                    pass
                else:
                    list_of_pngs.append(os.path.join(work_dir,rel_dir, file))
                    #print(list_of_pngs)
print(len(list_of_pngs))
z= 0

z= 0

n=0
random.shuffle(list_of_pngs)
number_didnt_process=0
if __name__ == '__main__':
    with mp.Pool(14) as p:
        try:
            p.map(rename_file, list_of_pngs)
        except:

```

```

        number_didnt_process +=1
    print ("done")

end = time.time()
time_took = end - start
string = 'I processed {} in only {} seconds! Averaging {} seconds per
image!'.format(str(len(list_of_pngs)), str(time_took), str(time_took/len(list_of_pngs)))
print(string)
print('Ammount didnt process= '+str(number_didnt_process))

```

Computer code 4.3: QR codes generated from a text file and distributed over A4 sticker sheets as required. The code leaves space as it distributes the QR codes over the page for ease of cutting out the stickers by the end user. The code is also capable of separating QR codes by group if required.

```

import qrcode
from PIL import Image, ImageDraw, ImageFont
import os
import glob
from natsort import natsorted
import time

#iterators
line_number = 0
tray_number = 1 # this will go till 84
layer_number = 1 # can be either 1 or 2

#logic:
"""
1. as we iterate we are going to check which layer we are in and which tray
2. if either the layer or the tray has changed, add a row of empty spaces on the paper ## a
row is 16 blocks long
"""
page_number=0

```

```

number_rep = 15 #how often do you want the same thing in the out_list.txt file

### the csv is layed out like this:
# "", "bench", "tray", "layer", "plots", "treatments", "reps"
dir_path = r'C:\labbook\All_scripts\QR-codes\making QR codes\ForManualCutLayout'
os.chdir(dir_path)

ListOfQRcodesAndNumberSplitters = [] ### this is a list of all the images to be made
including the qr codes and the numbers of the tpye e.g. col-0 rep1 == type 1 col-0 rep2 ==
type 1 but col-3 rep 1 == type 2 etc

typeCounter = 0
with open('input.txt','r') as f:
    for lines in f:
        ListOfQRcodesAndNumberSplitters.append(typeCounter) ## creates a divider to keep
the qr codes linked to the same genotype
        typeCounter+=1 ## adds to the counter for the next genotype
        for reps in range(0,number_rep):
            ListOfQRcodesAndNumberSplitters.append(str(reps)+' '+str(lines))

os.chdir(dir_path)

### removes any old made files from the working dir
for file in os.listdir(dir_path):
    if file.endswith('.bmp'):
        os.remove(file)
    elif file.endswith('.tiff'):
        os.remove(file)

qr = qrcode.QRCode(
    version=10,
    error_correction=qrcode.constants.ERROR_CORRECT_H,
    box_size=10,
    border=4,
)

plakken_timer = 1 ## if is 3 it will go next page

```

```

n=0
splitter_number =1
font = ImageFont.truetype("arial.ttf", 40)
for i in ListOfQRcodesAndNumberSplitters:
    if isinstance(i, int):
        splitter_number +=1
        length_string = len(str(i))
        img = Image.new('RGB', (50*length_string, 50*length_string), color = 'white')
        d = ImageDraw.Draw(img)
        d.text((0, 0), str(i), font=font,fill=(0,0,0))
        img.save(str(n)+".bmp")
        n+=1
    else:
        #print(i)
        img = qrcode.make(i)
        type(img) # qrcode.image.pil.PilImage
        img.save(str(n)+".bmp")
        n+=1

### defining an A4 page
width, height = 4961 , 7016
"""
max that would fit in the page:
width = 4961/236 = 21
height = 7016/236 = 29
"""
images= []
for file in natsorted(glob.glob("*.bmp")):
    images.append(file)
size =236,236
# to middle circle of sticker sheet
# top 16.75 mm = 396 Pixel
# side 19.75 mm = 467 Pixel
# between top to bot : 15.5 mm 366 Pixel
# between left to right 15.5 mm 366 Pixel

```

```

top=100
side=100
between=236
t=0
l=0
list_images=[]
for image in images:
    imagez = Image.open(image)
    imagez.thumbnail(size, Image.ANTIALIAS)
    list_images.append(imagez)

import matplotlib.pyplot as plt

n=0
print(len(list_images))
repCounter = 0
number_of_stickers_done = 1
columns = 28
rows = 20
number_of_Stickers_on_page = columns*rows
### pasting the previously made images onto the pdf
i=0
while len(list_images) > n:
    print(n)
    i+=1
    page = Image.new('RGB', (width, height), 'white')
    for l in range(0, columns):
        for t in range(0, rows):
            if len(list_images) <= n:
                #print('if')
                pass
            elif number_rep+1 == repCounter: ### if we have done all the reps, set the breaker
                #print('elif')
                repCounter = 0
                #n-=1

```

```

        break
    else:
        #print('else')
        repCounter+=1
        page.paste(list_images[n], box=(side + (t * between), top + (l * between)))
        n += 1
page.save((str(i)+'page.tiff'), interlace=False)
imgplot = plt.imshow(page)
plt.show()

### removes any old made files from the working dir
for file in os.listdir(dir_path):
    if file.endswith('.bmp'):
        os.remove(file)

```

Computer code 4.4: QR code information was directly read from the image and the results was added to the name of the file. Finding a QR code

```

run("Set Measurements...", "area mean standard modal min centroid center perimeter
bounding fit shape feret's integrated median skewness kurtosis area_fraction stack
redirect=None decimal=3");

// the macro
folder_loc = "/home/ok297/color plates testing/DarkRed/blue/color_transfer/result/"

dir = getFileList(folder_loc);
Array.print(dir);

// make out dir
outdirname = folder_loc+'_outdir'
File.makeDirectory(outdirname);

for (xx=0;xx<dir.length;xx++){
    file = getFileList(folder_loc+dir[xx]);
}

```

```

open(folder_loc+dir[xx]);

run("Duplicate...", " ");

run("Select None");

// Color Thresholder 1.53k
// Autogenerated macro, single images only!
min=newArray(3);
max=newArray(3);
filter=newArray(3);
a=getTitle();
run("HSB Stack");
run("Convert Stack to Images");
selectWindow("Hue");
rename("0");
selectWindow("Saturation");
rename("1");
selectWindow("Brightness");
rename("2");
min[0]=110;
max[0]=195;
filter[0]="pass";
min[1]=0;
max[1]=255;
filter[1]="pass";
min[2]=70;
max[2]=255;
filter[2]="pass";
for (i=0;i<3;i++){
  selectWindow(""+i);
  setThreshold(min[i], max[i]);
  run("Convert to Mask");
  if (filter[i]=="stop") run("Invert");
}
imageCalculator("AND create", "0","1");

```

```

imageCalculator("AND create", "Result of 0", "2");
for (i=0;i<3;i++){
  selectWindow(""+i);
  close();
}
selectWindow("Result of 0");
close();
selectWindow("Result of Result of 0");
rename(a);

run("8-bit");

run("Remove Outliers...", "radius=5 threshold=50 which=Dark");

waitForUser("Please draw a ROI on the area of interest. Please exclude the edges of the
plate including bits of parafilm and click 'OK'.");

run("Analyze Particles...", "size=250-5000 circularity=0.65-1.00 show=[Outlines]
summarize add");

name_string = dir[xx];
tiff_string = '.tiff';
outname = outdirname+'/' +name_string+tiff_string;
saveAs("Tiff", outname);
outname_csv = outdirname+'/' +name_string+tiff_string+".csv";
saveAs("Results", outname_csv);
close();
close();
close();
  run("Clear Results");
}

```

8 References

1. Systematic Position and Phylogeny. *The Biology of Nematodes* 1–30 (2002) doi:10.1201/B12614-1.
2. Aguinaldo, A. M. A. *et al.* Evidence for a clade of nematodes, arthropods and other moulting animals. *Nature* 1997 387:6632 **387**, 489–493 (1997).
3. Barnes, R. D. *Invertebrate Zoology*.
4. Seymour, M. K., Wright, K. A. & Doncaster, C. C. The action of the anterior feeding apparatus of *Caenorhabditis elegans* (Nematoda: Rhabditida). *J Zool* **201**, 527–539 (1983).
5. Hasna, M., Insunza, V., Lagerlö, J., Rämert, B. & Hasna, C. M. Food attraction and population growth of fungivorous nematodes with different fungi. *Wiley Online Library* **151**, 175–182 (2007).
6. Moens, T. & Vincx, M. Observations on the feeding ecology of estuarine nematodes. *Journal of the Marine Biological Association of the United Kingdom* **77**, 211–227 (1997).
7. Bedding, R. A. & Akhurst, R. J. A simple technique for the detection of insect parasitic rhabditid nematodes in soil. *Nematologica* **21**, 109–110 (1975).
8. Yeates, G. W., Bongers, T., De Goede, R. G. M., Freckman, D. W. & Georgieva, S. S. Feeding Habits in Soil Nematode Families and Genera—An Outline for Soil Ecologists. *J Nematol* **25**, 315 (1993).
9. Wilecki, M., Lightfoot, J. W., Susoy, V. & Sommer, R. J. Predatory feeding behaviour in *Pristionchus* nematodes is dependent on phenotypic plasticity and induced by serotonin. *J Exp Biol* **218**, 1306–1313 (2015).
10. Nöckler, K., Reckinger, S. & Pozio, E. *Trichinella spiralis* and *Trichinella pseudospiralis* mixed infection in a wild boar (*Sus scrofa*) of Germany. *Vet Parasitol* **137**, 364–368 (2006).
11. A worm's world. <https://www.rsb.org.uk/biologist-features/this-is-a-worm-s-world>.
12. Blaxter, M. & Koutsovoulos, G. The evolution of parasitism in Nematoda. *Parasitology* **142**, S26 (2015).
13. D., L. P. J. Recent developments in marine benthic biodiversity research. *Oceanis* **19**, 5–24 (1993).

14. Blaxter, M. L. *et al.* A molecular evolutionary framework for the phylum Nematoda. *Nature* 1998 392:6671 **392**, 71–75 (1998).
15. Chitwood, B. G. The designation of official names for higher taxa of invertebrates. *Bulletin of Zoological Nomenclature* **15**, 860–895 (1958).
16. Chitwood, B. G. A revised classification of the Nematoda. *A revised classification of the Nematoda.* (1937).
17. Chitwood, B., parasitology, M. C.-J. of & 1933, undefined. The characters of a protonematode. *library.wur.nl*.
18. Holterman, M. *et al.* Phylum-Wide Analysis of SSU rDNA Reveals Deep Phylogenetic Relationships among Nematodes and Accelerated Evolution toward Crown Clades. *Mol Biol Evol* **23**, 1792–1800 (2006).
19. HODDA, M. **Phylum Nematoda: a classification, catalogue and index of valid genera, with a census of valid species**. *Zootaxa* **5114**, 1–289 (2022).
20. Maizels, R. M., Smits, H. H. & McSorley, H. J. Modulation of Host Immunity by Helminths: The Expanding Repertoire of Parasite Effector Molecules. *Immunity* **49**, 801–818 (2018).
21. Stepek, G., Buttle, D. J., Duce, I. R. & Behnke, J. M. Human gastrointestinal nematode infections: are new control methods required? *Int J Exp Pathol* **87**, 325 (2006).
22. Pullan, R. L., Smith, J. L., Jasrasaria, R. & Brooker, S. J. Global numbers of infection and disease burden of soil transmitted helminth infections in 2010. *Parasit Vectors* **7**, 1–19 (2014).
23. White, R., Blow, F., Buck, A. H. & Duque-Correa, M. A. Organoids as tools to investigate gastrointestinal nematode development and host interactions. *Front Cell Infect Microbiol* **12**, 976017 (2022).
24. Organization, W. H. Global health situation and projections estimates. (1992).
25. Ye, Z., Eickhoff, J. & Kesler, M. Eosinophilic Pseudoleukemia Due to Toxocariasis in a 3-year-old Patient: Report of A Rare Case. *Am J Clin Pathol* **142**, A104–A104 (2014).
26. Sharma, R., Singh, B. B. & Gill, J. P. S. Larva migrans in India: veterinary and public health perspectives. *Journal of Parasitic Diseases* **39**, 604–612 (2015).

27. Genomics and Molecular Genetics of Plant-Nematode Interactions. *Genomics and Molecular Genetics of Plant-Nematode Interactions* (2011) doi:10.1007/978-94-007-0434-3.
28. Abad, P. *et al.* Genome sequence of the metazoan plant-parasitic nematode *Meloidogyne incognita*. *Nat Biotechnol* **26**, 909–915 (2008).
29. Sasser, J. N. A world perspective on nematology: the role of the society. *Vistas on Nematology*. 7–14 (1987).
30. Chitwood, D. J. Research on plant-parasitic nematode biology conducted by the United States Department of Agriculture–Agricultural Research Service. *Pest Manag Sci* **59**, 748–753 (2003).
31. Singh, S. K., Hodda, M. & Ash, G. J. Plant-parasitic nematodes of potential phytosanitary importance, their main hosts and reported yield losses. *EPPO Bulletin* **43**, 334–374 (2013).
32. Agriculture Overview: Development news, research, data | World Bank. <https://www.worldbank.org/en/topic/agriculture/overview>.
33. Macroeconomy. <https://www.fao.org/3/i2490e/i2490e01c.pdf>.
34. Summary - GOV.UK. <https://www.gov.uk/government/statistics/agriculture-in-the-united-kingdom-2021/summary>.
35. Chapter 7: Crops - GOV.UK. <https://www.gov.uk/government/statistics/agriculture-in-the-united-kingdom-2021/chapter-7-crops>.
36. Rich, J. R., Dunn, R. A. & Noling, J. W. Nematicides: past and present uses. *Nematology: advances and perspectives. Volume 2: Nematode management and utilization* 1179–1200 (2004) doi:10.1079/9780851996462.1179.
37. Toxic Pesticide Banned after Decades of Use - Scientific American. <https://www.scientificamerican.com/article/toxic-pesticide-banned-after-decades-of-use/>.
38. Chemical control of nematodes: efficiency and side-effects. <https://www.fao.org/3/V9978E/v9978e08.htm>.
39. Change required from top to bottom - cpm magazine. <https://www.cpm-magazine.co.uk/roots/change-required-from-top-to-bottom/>.

40. Trial shows best nematicide strategy for PCN in potatoes - Farmers Weekly. <https://www.fwi.co.uk/arable/crop-management/pests/trial-shows-best-nematicide-strategy-for-pcn-in-potatoes>.
41. Chen, J., Li, Q. X. & Song, B. Chemical Nematicides: Recent Research Progress and Outlook. *J Agric Food Chem* **68**, 12175–12188 (2020).
42. Nematicides Market Size, Share, Growth Trends, and Forecast to 2027 | MarketsandMarkets. <https://www.marketsandmarkets.com/Market-Reports/nematicides-market-193252005.html>.
43. Pesticides (Temik) - Hansard - UK Parliament. [https://hansard.parliament.uk/Commons/1986-11-24/debates/815804e7-ac30-4b54-a38b-ebddc898d716/Pesticides\(Temik\)](https://hansard.parliament.uk/Commons/1986-11-24/debates/815804e7-ac30-4b54-a38b-ebddc898d716/Pesticides(Temik)).
44. Potato growers lose Vydate in nematode battle - Farmers Weekly. <https://www.fwi.co.uk/arable/potatoes/potato-growers-lose-vydate-in-nematode-battle>.
45. European Union Risk Assessment Report.
46. EU Pesticides Database - Active substances - Active substance details. <https://ec.europa.eu/food/plant/pesticides/eu-pesticides-database/start/screen/active-substances/details/384>.
47. EU Pesticides Database - Active substances - Active substance details. <https://ec.europa.eu/food/plant/pesticides/eu-pesticides-database/start/screen/active-substances/details/208>.
48. EU Pesticides Database - Active substances - Active substance details. <https://ec.europa.eu/food/plant/pesticides/eu-pesticides-database/start/screen/active-substances/details/752>.
49. Lewis, K. A., Tzilivakis, J., Warner, D. J. & Green, A. An international database for pesticide risk assessments and management. *Human and Ecological Risk Assessment* **22**, 1050–1064 (2016).
50. EU Pesticides Database - Active substances - Active substance details. <https://ec.europa.eu/food/plant/pesticides/eu-pesticides-database/start/screen/active-substances/details/723>.
51. EU Pesticides Database - Active substances - Active substance details. <https://ec.europa.eu/food/plant/pesticides/eu-pesticides-database/start/screen/active-substances/details/508>.

52. Pesticide loss brings wireworm challenge for potato growers - Farmers Weekly. <https://www.fwi.co.uk/arable/crop-management/pests/pesticide-loss-brings-wireworm-challenge-for-potato-growers>.
53. Recitals Regulation (EU) 2023/128. <https://lexparency.org/eu/32023R0128/PRE/>.
54. EU Pesticides Database - Active substances - Active substance details. <https://ec.europa.eu/food/plant/pesticides/eu-pesticides-database/start/screen/active-substances/details/835>.
55. EU Pesticides Database - Active substances - Active substance details. <https://ec.europa.eu/food/plant/pesticides/eu-pesticides-database/start/screen/active-substances/details/238>.
56. EU Pesticides Database - Active substances - Active substance details. <https://ec.europa.eu/food/plant/pesticides/eu-pesticides-database/start/screen/active-substances/details/491>.
57. Dangl, J. L. & Jones, J. D. G. Plant pathogens and integrated defence responses to infection. *Nature* 2001 411:6839 **411**, 826–833 (2001).
58. Bent, A. F. & Mackey, D. Elicitors, effectors, and R genes: The new paradigm and a lifetime supply of questions. *Annu Rev Phytopathol* **45**, 399–436 (2008).
59. Van Der Biezen, E. A. & Jones, J. D. G. Plant disease-resistance proteins and the gene-for-gene concept. *Trends Biochem Sci* **23**, 454–456 (1998).
60. Davies, L. J. & Elling, A. A. Resistance genes against plant-parasitic nematodes: a durable control strategy? *Nematology* **17**, 249–263 (2015).
61. Sandal, N. N. *et al.* Backcrossing of nematode-resistant sugar beet: A second nematode resistance gene at the locus containing Hslpro-1? *Molecular Breeding* **3**, 471–480 (1997).
62. Genomics and Molecular Genetics of Plant-Nematode Interactions. *Genomics and Molecular Genetics of Plant-Nematode Interactions* 318 (2011) doi:10.1007/978-94-007-0434-3.
63. Tameling, W. I. L. *et al.* Mutations in the NB-ARC Domain of I-2 That Impair ATP Hydrolysis Cause Autoactivation. *Plant Physiol* **140**, 1233–1245 (2006).
64. Jones, J. D. G. & Dangl, J. L. The plant immune system. *Nature* 2006 444:7117 **444**, 323–329 (2006).

65. Sacco, M. A. *et al.* The Cyst Nematode SPRYSEC Protein RBP-1 Elicits Gpa2- and RanGAP2-Dependent Plant Cell Death. **5**, e1000564 (2009).
66. Janssen, R., Bakker, J., Nematol, F. G.-Rev. & 1991, undefined. Mendelian proof for a gene-for-gene relationship between virulence of *Globodera rostochiensis* and the H1 resistance gene in *Solanum tuberosum* ssp. *CiteseerR Janssen, J Bakker, FJ GommersRev. Nematol, 1991•Citeseer.*
67. van Steenbrugge, J. J. M. *et al.* Comparative genomics of two inbred lines of the potato cyst nematode *Globodera rostochiensis* reveals disparate effector family-specific diversification patterns. *BMC Genomics* **22**, (2021).
68. Siddique, S. *et al.* The genome and lifestage-specific transcriptomes of a plant-parasitic nematode and its host reveal susceptibility genes involved in trans-kingdom synthesis of vitamin B5. *Nature Communications* 2022 13:1 **13**, 1–19 (2022).
69. Radakovic, Z. S. *et al.* Arabidopsis HIP27 is a host susceptibility gene for the beet cyst nematode *Heterodera schachtii*. *Mol Plant Pathol* **19**, (2018).
70. Willig, J.-J. *et al.* From root to shoot; Quantifying nematode tolerance in *Arabidopsis thaliana* by high-throughput phenotyping of plant development. *bioRxiv* 2023.03.15.532731 (2023) doi:10.1101/2023.03.15.532731.
71. Seinhorst, J. W. Effects of Nematode Attack on the Growth and Yield of Crop Plants. *Cyst Nematodes* 191–209 (1986) doi:10.1007/978-1-4613-2251-1_11.
72. Shrestha, R., Uzzo, F., Wilson, M. J. & Price, A. H. Physiological and genetic mapping study of tolerance to root-knot nematode in rice. *New Phytologist* **176**, 665–672 (2007).
73. Willig, J. J. *et al.* The Arabidopsis transcription factor TCP9 modulates root architectural plasticity, reactive oxygen species-mediated processes, and tolerance to cyst nematode infections. *The Plant Journal* **112**, 1070–1083 (2022).
74. Recommended List - BBRO. <https://bbro.co.uk/sugar-beet-varieties/recommended-list/>.
75. Perry, R. N., Moens, M., Jones, J. (John T. & C.A.B. International. Cyst nematodes.
76. Trudgill, D. L., Phillips, M. S. & Elliott, M. J. Dynamics and management of the white potato cyst nematode *Globodera pallida* in commercial potato crops. *Annals of Applied Biology* **164**, 18–34 (2014).
77. Thomas, S. H., Schroeder, J. & Murray, L. W. The role of weeds in nematode management. *Weed Sci* **53**, 923–928 (2005).

78. Nelson, K. A., Johnson, W. G., Wait, J. D. & Smoot, R. L. Winter-Annual Weed Management in Corn (*Zea mays*) and Soybean (*Glycine max*) and the Impact on Soybean Cyst Nematode (*Heterodera glycines*) Egg Population Densities. *Weed Technology* **20**, 965–970 (2006).
79. Kirkegaard, J. A., Sarwar, M. & Matthiessen, J. N. Assessing the biofumigation potential of crucifers. *Acta Horti* **459**, 105–111 (1997).
80. Watts, W., Grove, I., Hand, P., Biology, M. B.-A. of A. & 2015, undefined. Brassica residue incorporation technique for optimized biofumigation of potato cyst nematodes. *cabdirect.org*.
81. Oka, Y. Mechanisms of nematode suppression by organic soil amendments—A review. *Applied Soil Ecology* **44**, 101–115 (2010).
82. Grainger, J. Factors Affecting the Control of Eelworm Diseases 1). *Nematologica* **10**, 5–20 (1964).
83. Michael, --, Robinson+, P., Atkinson+, H. J. & Perry, R. N. The influence of soil moisture and storage time on the motility, infectivity and lipid utilization of second stage juveniles of the potato cyst nematodes *Globodera rostochiensis* and *G. pallida*.
84. Scholte, K. & Vos, J. Effects of potential trap crops and planting date on soil infestation with potato cyst nematodes and root-knot nematodes. *Annals of Applied Biology* **137**, 153–164 (2000).
85. Rojas-Sandoval, J. *Solanum sisymbriifolium* (sticky nightshade). *CABI Compendium CABI Compendium*, (2022).
86. Mhatre, P. H. *et al.* Management of potato cyst nematodes with special focus on biological control and trap cropping strategies. *Pest Manag Sci* **78**, 3746–3759 (2022).
87. Urwin, P. E., Lilley, C. J. & Atkinson, H. J. Ingestion of double-stranded RNA by parasitic juvenile cyst nematodes leads to RNA interference. *Molecular Plant-Microbe Interactions* **15**, 747–752 (2002).
88. Rosso, M. N., Dubrana, M. P., Cimbolini, N., Jaubert, S. & Abad, P. Application of RNA Interference to Root-Knot Nematode Genes Encoding Esophageal Gland Proteins. <https://doi.org/10.1094/MPMI-18-0615> **18**, 615–620 (2007).
89. Haegeman, A., ... B. V.-M. P. & 2009, undefined. Characterization of a putative endoxylanase in the migratory plant-parasitic nematode *Radopholus similis*. *Wiley Online Library* **10**, 389–401 (2009).

90. Yadav, B. C., Veluthambi, K. & Subramaniam, K. Host-generated double stranded RNA induces RNAi in plant-parasitic nematodes and protects the host from infection. *Mol Biochem Parasitol* **148**, 219–222 (2006).
91. Banerjee, S. *et al.* RNA Interference: A Novel Source of Resistance to Combat Plant Parasitic Nematodes. *Front Plant Sci* **8**, 834 (2017).
92. amaryllis lesion nematode- Pratylenchus hippeastri. https://entnemdept.ufl.edu/creatures/NEMATODE/amarlyllis_nematode.htm.
93. Decraemer, W. & Robbins, R. T. The Who, What and Where of Longidoridae and Trichodoridae. *J Nematol* **39**, 295 (2007).
94. Gutiérrez-Gutiérrez, C., Bravo, M. A., Santos, M. T., Vieira, P. & Mota, M. **An update on the genus Longidorus, Paralongidorus and Xiphinema (Family Longidoridae) in Portugal**. *Zootaxa* **4189**, 99–114 (2016).
95. Technol, M. M.-Agric. Res. & 2018, undefined. Plant-parasitic nematodes and their management: A review. *pdfs.semanticscholar.org* **8**, (2018).
96. Claerbout, J. *et al.* A thorough study of a Paratylenchus sp. in glasshouse-grown lettuce: Characterisation, population dynamics, host plants and damage threshold as keys to its integrated management. *Annals of Applied Biology* **178**, 62–79 (2021).
97. Brooks. Burrowing Nematode. *Plant Health Instructor* (2008) doi:10.1094/PHI-I-2008-1020-01.
98. Kimpinski, J. Root lesion nematodes in potatoes. *Am Potato J* **56**, 79–86 (1979).
99. Rowe, R., Riedel, R., Phytopathology, M. M.- & 1985, undefined. Synergistic interactions between *Verticillium dahliae* and *Pratylenchus penetrans* in potato early dying disease. *apsnet.org*.
100. Lambert, K. & Bekal, S. Introduction to Plant-Parasitic Nematodes. *The Plant Health Instructor* (2002) doi:10.1094/PHI-I-2002-1218-01.
101. Ankrom, K. E. *et al.* Ecto- and endoparasitic nematodes respond differently across sites to changes in precipitation. *Oecologia* **193**, 761–771 (2020).
102. Holbein, J., Grundler, F. M. W. & Siddique, S. Plant basal resistance to nematodes: an update. *J Exp Bot* **67**, 2049–2061 (2016).

103. Verdejo-Lucas, S. & Kaplan, D. T. The citrus nematode: *Tylenchulus semipenetrans* . . *Plant resistance to parasitic nematodes* 207–219 (2002) doi:10.1079/9780851994666.0207.
104. Moens, M. & Perry, R. N. Migratory Plant Endoparasitic Nematodes: A Group Rich in Contrasts and Divergence. <https://doi.org/10.1146/annurev-phyto-080508-081846> **47**, 313–332 (2009).
105. Handoo, Z., Kantor, M. & Carta, L. Taxonomy and Identification of Principal Foliar Nematode Species (Aphelenchoides and Litylenchus). **9**, (2020).
106. Xvi A. XVI. A letter from Mr. Turbevil Needham, to the President; concerning certain chalky tubulous concretions, called malm; with some microscopical observations on the farina of the red lily, and of worms discovered in smutty corn. *Philos Trans R Soc Lond* **42**, 634–641 (1743).
107. Singh, V. K. *et al.* Spectroscopic investigation of wheat grains (*Triticum aestivum*) infected by wheat seed gall nematodes (*Anguina tritici*). *Biocatal Agric Biotechnol* **9**, 58–66 (2017).
108. Subbotin, S. A., Mundo-Ocampo, Manuel. & Baldwin, J. G. 2. *Biology And Evolution*. (Brill, 2010).
109. Perry, R. N. & Moens, M. Introduction to Plant-Parasitic Nematodes; Modes of Parasitism. *Genomics and Molecular Genetics of Plant-Nematode Interactions* 3–20 (2011) doi:10.1007/978-94-007-0434-3_1.
110. Palomares-Rius, J. E. *et al.* Gene expression changes in diapause or quiescent potato cyst nematode, *Globodera pallida*, eggs after hydration or exposure to tomato root diffusate. *PeerJ* **2016**, (2016).
111. Lane: Potato cyst nematode: A management guide - Google Scholar. https://scholar.google.com/scholar_lookup?title=Potato+cyst+nematode:+a+management+guide&author=A+Lane&author=D+Trudgill&publication_year=1999&.
112. Byrne, J., Twomey, U., Maher, N., Devine, K. J. & Jones, P. W. Detection of hatching inhibitors and hatching factor stimulants for golden potato cyst nematode, *Globodera rostochiensis*, in potato root leachate. *Annals of Applied Biology* **132**, 463–472 (1998).
113. Doncaster, C. C. & Seymour, M. K. Exploration and selection of penetration site by Tylenchida. *Nematologica* **19**, 137–145 (1973).

114. ROBINSON, M., ATKINSON, H., Nématol, R. P.-R. & 1987, undefined. potato cyst nematodes *Globodera rostochiensis* and *G. pallida*. *core.ac.uk*.
115. Mekete, T., Reynolds, K., Lopez-Nicora, H. D., Gray, M. E. & Niblack, T. L. Distribution and diversity of root-lesion nematode (*Pratylenchus* spp.) associated with *Miscanthus x giganteus* and *Panicum virgatum* used for biofuels, and species identification in a multiplex polymerase chain reaction. *Nematology* **13**, 673–686 (2011).
116. Curtis, R. H. C., Robinson, A. F. & Perry, R. N. Hatch and host location. *Root-knot Nematodes* 139–162 (2009) doi:10.1079/9781845934927.0139.
117. Santos-Garcia, D. *et al.* Complete Genome Sequence of “Candidatus Portiera aleyrodidarum” BT-QVLC, an Obligate Symbiont That Supplies Amino Acids and Carotenoids to *Bemisia tabaci*. *J Bacteriol* **194**, 6654–6655 (2012).
118. Perry, R. N. An evaluation of types of attractants enabling plant-parasitic nematodes to locate plant roots. *Russ J Nematol* **13**, 83–88 (2005).
119. Golinowski, W., Grundler, F. M. W. W. & Sobczak, M. Changes in the structure of *Arabidopsis thaliana* during female development of the plant-parasitic nematode *Heterodera schachtii*. *Protoplasma* **194**, 103–116 (1996).
120. Sobczak, M., Golinowski, W. & Grundler, F. M. W. Changes in the structure of *Arabidopsis thaliana* roots induced during development of males of the plant parasitic nematode *Heterodera schachtii*. *Eur J Plant Pathol* **103**, 113–124 (1997).
121. Golinowski, W., Sobczak, M., Kurek, W. & Grymaszewska, G. The Structure of Syncytia. 80–97 (1997) doi:10.1007/978-94-011-5596-0_7.
122. Hussey, R. S. & Mims, C. W. Ultrastructure of esophageal glands and their secretory granules in the root-knot nematode *Meloidogyne incognita*. *Protoplasma* **156**, 9–18 (1990).
123. Hussey, R. S. DISEASE-INDUCING SECRETIONS OF PLANT-PARASITIC NEMATODES. *Annu. Rev. Phytopathol* **27**, 123–164 (1989).
124. Hewezi, T. & Baum, T. J. Manipulation of plant cells by cyst and root-knot nematode effectors. *Molecular Plant-Microbe Interactions* **26**, 9–16 (2013).
125. Wyss, U. & Zunke, U. Observations on the behaviour of second stage juveniles of *Hetero* inside host roots.
126. Wyss, U. & Grundler, F. M. W. Feeding behavior of sedentary plant parasitic nematodes. *Netherlands Journal of Plant Pathology* **98**, 165–173 (1992).

127. Waetzig, G. H., Sobczak, M. & Grundler, F. M. W. Localization of hydrogen peroxide during the defence response of *Arabidopsis thaliana* against the plant-parasitic nematode *Heterodera glycines*. *Nematology* **1**, 681–686 (1999).
128. Sobczak, M. & Golinowski, W. Structure of Cyst Nematode Feeding Sites. 1–35 (2008) doi:10.1007/7089_2008_38.
129. Magnusson, C. & Golinowski, W. Ultrastructural relationships of the developing syncytium induced by *Heterodera schachtii* (Nematoda) in root tissues of rape. <https://doi.org/10.1139/b91-008> **69**, 44–52 (2011).
130. Grundler, F. M. W., Sobczak, M. & Golinowski, W. Formation of wall openings in root cells of *Arabidopsis thaliana* following infection by the plant-parasitic nematode *Heterodera schachtii*. *Eur J Plant Pathol* **104**, 545–551 (1998).
131. Magnusson, C. & Golinowski, W. Ultrastructural relationships of the developing syncytium induced by *Heterodera schachtii* (Nematoda) in root tissues of rape . *Canadian Journal of Botany* **69**, 44–52 (1991).
132. Sobczak, M. & Golinowski, W. Cyst Nematodes and Syncytia. *Genomics and Molecular Genetics of Plant-Nematode Interactions* 61–82 (2011) doi:10.1007/978-94-007-0434-3_4.
133. Rodiuc, N., Vieira, P., Banora, M. Y. & de Almeida Engler, J. On the track of transfer cell formation by specialized plant-parasitic nematodes. *Front Plant Sci* **5**, 76813 (2014). <https://creativecommons.org/licenses/by/3.0/>
134. Muller, J., Rehbock, K., Nématologie, U. W.-R. de & 1981, undefined. Growth of *Heterodera schachtii* with remarks on amounts of food consumed. *cabdirect.org* **4**, 227–234 (1981).
135. Anjam, M. S. *et al.* Host factors influence the sex of nematodes parasitizing roots of *Arabidopsis thaliana*. *Plant Cell Environ* **43**, 1160–1174 (2020).
136. Tytgat, T. *et al.* Development and pharyngeal gland activities of *Heterodera schachtii* infecting *Arabidopsis thaliana* roots. *Nematology* **4**, 899–908 (2002).
137. Evans, A., Nematologica, J. F.- & 1970, undefined. The effect of environment on nematode morphometrics. Comparison of *Ditylenchus myceliophagus* and *D. destructor*. *cabdirect.org*.
138. Politz, S. M. & Philipp, M. *Caenorhabditis elegans* as a model for parasitic nematodes: A focus on the cuticle. *Parasitology Today* **8**, 6–12 (1992).

139. O'Malley, R. C., Barragan, C. C. & Ecker, J. R. A User's Guide to the Arabidopsis T-DNA Insertional Mutant Collections. *Methods Mol Biol* **1284**, 323 (2015).
140. Rönspies, M., Schindele, P., Wetzel, R. & Puchta, H. CRISPR–Cas9-mediated chromosome engineering in Arabidopsis thaliana. *Nature Protocols* **2022** 17:5 **17**, 1332–1358 (2022).
141. Miki, D., Zhang, W., Zeng, W., Feng, Z. & Zhu, J. K. CRISPR/Cas9-mediated gene targeting in Arabidopsis using sequential transformation. *Nature Communications* **2018** 9:1 **9**, 1–9 (2018).
142. Clough, S. J. & Bent, A. F. Floral dip: a simplified method for Agrobacterium-mediated transformation of Arabidopsis thaliana. *Plant J* **16**, 735–743 (1998).
143. Alonso, J. M. *et al.* Genome-wide insertional mutagenesis of Arabidopsis thaliana. *Science* **301**, 653–657 (2003).
144. Sijmons, P., Grundler, F., ... N. von M.-T. P. & 1991, undefined. Arabidopsis thaliana as a new model host for plant-parasitic nematodes. *Wiley Online Library* **1**, 245–254 (1991).
145. Clarke, A. J. & Shepherd, A. M. Zinc and Other Metallic Ions as Hatching Agents for the Beet Cyst Nematode, *Heterocdera schachtii* Schm. *Nature* **1965** 208:5009 **208**, 502–502 (1965).
146. Kranse, O. *et al.* Toward genetic modification of plant-parasitic nematodes: delivery of macromolecules to adults and expression of exogenous mRNA in second stage juveniles. *G3 Genes/Genomes/Genetics* **11**, 2020.07.15.193052 (2021).
147. Vidal, M., Wolf, N., Rosenberg, B., Harris, B. P. & Mathis, A. Perspectives on Individual Animal Identification from Biology and Computer Vision. *Integr Comp Biol* **61**, 900–916 (2021).
148. Roberts, E. H. Temperature and seed germination. in *Symposia of the Society for Experimental Biology* vol. 42 109–132 (1988).
149. Hoagiand, D. R. Nutrition of strawberry plant under controlled conditions.(a) Effects of deficiencies of boron and certain other elements,(b) susceptibility to injury from sodium salts. in *Proc. Amer. Soc. Hort. Sci.* vol. 30 288–294 (1933).
150. Iyer, J., DeVaul, N., Hansen, T. & Nebenfuehr, B. Using Microinjection to Generate Genetically Modified *Caenorhabditis elegans* by CRISPR/Cas9 Editing. in *Methods in molecular biology (Clifton, N.J.)* vol. 1874 431–457 (2019).

151. Primer3Plus. <http://www.bioinformatics.nl/cgi-bin/primer3plus/primer3plus.cgi>.
152. Sambrook, J. Molecular cloning: a laboratory manual/Joseph Sambrook, David W. Russell, ed. DW Russell, L. Cold Spring Harbor 2001.
153. Conte, D., MacNei, L. T., Walhout, A. J. M. & Mello, C. C. RNA Interference in *Caenorhabditis Elegans*. *Curr Protoc Mol Biol* **109**, 26.3.1 (2015).
154. Zhang, X., Henriques, R., Lin, S. S., Niu, Q. W. & Chua, N. H. Agrobacterium-mediated transformation of *Arabidopsis thaliana* using the floral dip method. *Nature Protocols* **2006** 1:2 **1**, 641–646 (2006).
155. Ran, F. A. *et al.* Genome engineering using the CRISPR-Cas9 system. *Nature Protocols* **2013** 8:11 **8**, 2281–2308 (2013).
156. Kadandale, P., Chatterjee, I. & Singson, A. Germline transformation of *Caenorhabditis elegans* by injection. *Methods Mol Biol* **518**, 123 (2009).
157. Joung, J. K. & Sander, J. D. TALENs: a widely applicable technology for targeted genome editing. *Nature Reviews Molecular Cell Biology* **2012** 14:1 **14**, 49–55 (2012).
158. Nagy, A. Cre Recombinase: The Universal Reagent for Genome Tailoring. (2000) doi:10.1002/(SICI)1526-968X(200002)26:2.
159. Bakhietia, M., Charlton, W. L., Urwin, P. E., McPherson, M. J. & Atkinson, H. J. RNA interference and plant parasitic nematodes. *Trends Plant Sci* **10**, 362–367 (2005).
160. Brenner, S. THE GENETICS OF CAENORHABDITIS ELEGANS. *Genetics* **77**, 71–94 (1974).
161. Dickinson, D. J. & Goldstein, B. CRISPR-Based Methods for *Caenorhabditis elegans* Genome Engineering. *Genetics* **202**, 885–901 (2016).
162. Conte, D., MacNei, L. T., Walhout, A. J. M. & Mello, C. C. RNA Interference in *Caenorhabditis elegans*. *Curr Protoc Mol Biol* **109**, 26.3.1-26.3.30 (2015).
163. Kim, T. K. & Eberwine, J. H. Mammalian cell transfection: the present and the future. *Anal Bioanal Chem* **397**, 3173–3178 (2010).
164. Chow, Y. T. *et al.* Single Cell Transfection through Precise Microinjection with Quantitatively Controlled Injection Volumes. *Sci Rep* **6**, (2016).
165. Shi, B. *et al.* An improved method for increasing the efficiency of gene transfection and transduction. *Int J Physiol Pathophysiol Pharmacol* **10**, 95 (2018).

166. Yamano, S., Dai, J. & Moursi, A. M. Comparison of transfection efficiency of nonviral gene transfer reagents. *Mol Biotechnol* **46**, 287–300 (2010).
167. Mello, C. C., Kramer, J. M., Stinchcomb, D. & Ambros, V. Efficient gene transfer in *C. elegans*: extrachromosomal maintenance and integration of transforming sequences. *EMBO J* **10**, 3959–3970 (1991).
168. Lufino, M. M. P., Edser, P. A. H. & Wade-Martins, R. Advances in High-capacity Extrachromosomal Vector Technology: Episomal Maintenance, Vector Delivery, and Transgene Expression. *Molecular Therapy* **16**, 1525–1538 (2008).
169. Kim, T. K. & Eberwine, J. H. Mammalian cell transfection: The present and the future. *Anal Bioanal Chem* **397**, 3173–3178 (2010).
170. Recillas-Targa, F. Multiple strategies for gene transfer, expression, knockdown, and chromatin influence in mammalian cell lines and transgenic animals. *Mol Biotechnol* **34**, 337–354 (2006).
171. Moradian, H., Roch, T., Lendlein, A. & Gossen, M. mRNA Transfection-Induced Activation of Primary Human Monocytes and Macrophages: Dependence on Carrier System and Nucleotide Modification. *Scientific Reports 2020 10:1* **10**, 1–15 (2020).
172. Oh, S. & Kessler, J. A. Design, Assembly, Production, and Transfection of Synthetic Modified mRNA. *Methods* **133**, 29–43 (2018).
173. Mookkan, M. Particle bombardment – mediated gene transfer and GFP transient expression in *Seteria viridis*. *Plant Signal Behav* **13**, (2018).
174. Maas, C. & Werr, W. Mechanism and optimized conditions for PEG mediated DNA transfection into plant protoplasts. *Plant Cell Rep* **8**, 148–151 (1989).
175. Potter, H. & Heller, R. Transfection by Electroporation. *Current protocols in molecular biology / edited by Frederick M. Ausubel ... [et al.]* **CHAPTER**, Unit (2003).
176. Lok, J. B., Shao, H., Massey, H. C. & Li, X. Transgenesis in Strongyloides and related parasitic nematodes: historical perspectives, current functional genomic applications and progress towards gene disruption and editing. *Parasitology* **144**, 327 (2017).
177. Hashmi, S., Hashmi, G. & Gaugler, R. Genetic transformation of an entomopathogenic nematode by microinjection. *J Invertebr Pathol* **66**, 293–296 (1995).
178. Adams, S. *et al.* Liposome-based transfection enhances RNAi and CRISPR-mediated mutagenesis in non-model nematode systems. *bioRxiv* **9**, 429126 (2018).

179. Kramer, J. M., French, R. P., Park, E. C. & Johnson, J. J. The *Caenorhabditis elegans* rol-6 gene, which interacts with the sqt-1 collagen gene to determine organismal morphology, encodes a collagen. *Mol Cell Biol* **10**, 2081–2089 (1990).
180. Mello, C. & Fire, A. Chapter 19 DNA Transformation. *Methods Cell Biol* **48**, 451–482 (1995).
181. Felgner, P. L. *et al.* Lipofection: a highly efficient, lipid-mediated DNA-transfection procedure. *Proc Natl Acad Sci U S A* **84**, 7413 (1987).
182. Tenchov, R., Bird, R., Curtze, A. E. & Zhou, Q. Lipid Nanoparticles from Liposomes to mRNA Vaccine Delivery, a Landscape of Research Diversity and Advancement. *ACS Nano* **15**, 16982–17015 (2021).
183. Gregoriadis, G. Liposomes and mRNA: Two technologies together create a COVID-19 vaccine. *Med Drug Discov* **12**, 100104 (2021).
184. Nel, A. E. *et al.* Understanding biophysicochemical interactions at the nano–bio interface. *Nature Materials* 2009 8:7 **8**, 543–557 (2009).
185. Liu, X. & Huang, G. Formation strategies, mechanism of intracellular delivery and potential clinical applications of pH-sensitive liposomes. *Asian J Pharm Sci* **8**, 319–328 (2013).
186. Capecchi, M. R. Altering the genome by homologous recombination. *Science* (1979) **244**, 1288–1292 (1989).
187. I-SceI | NEB. <https://international.neb.com/products/r0694-i-scei#Product%20Information>.
188. Nicolás, A. L. & Young, C. S. Characterization of DNA end joining in a mammalian cell nuclear extract: junction formation is accompanied by nucleotide loss, which is limited and uniform but not site specific. *Mol Cell Biol* **14**, 170–180 (1994).
189. Cohen-Tannoudji, M. *et al.* I- Sce I-Induced Gene Replacement at a Natural Locus in Embryonic Stem Cells . *Mol Cell Biol* **18**, 1444–1448 (1998).
190. Wood, A. J. *et al.* Targeted genome editing across species using ZFNs and TALENs. *Science* (1979) **333**, 307 (2011).
191. Sander, J., Dahlborg, E., Goodwin, M., ... L. C.-N. & 2011, undefined. Selection-free zinc-finger-nuclease engineering by context-dependent assembly (CoDA). *nature.com*.

192. Miller, J., Holmes, M., Wang, J., ... D. G.-N. & 2007, undefined. An improved zinc-finger nuclease architecture for highly specific genome editing. *nature.com*.
193. Porteus, M. H. & Baltimore, D. Chimeric nucleases stimulate gene targeting in human cells. *Science (1979)* **300**, 763 (2003).
194. Sanjana, N. *et al.* A transcription activator-like effector toolbox for genome engineering. *nature.com*.
195. Moscou, M. J. & Bogdanove, A. J. A simple cipher governs DNA recognition by TAL effectors. *Science (1979)* **326**, 1501 (2009).
196. Boch, J. *et al.* Breaking the code of DNA binding specificity of TAL-type III effectors. *Science (1979)* **326**, 1509–1512 (2009).
197. Reyon, D., Tsai, S., Khayter, C., ... J. F.-N. & 2012, undefined. FLASH assembly of TALENs for high-throughput genome editing. *nature.com*.
198. Hockemeyer, D. *et al.* Genetic engineering of human pluripotent cells using TALE nucleases. *nature.com*.
199. Zhang, F. *et al.* Efficient construction of sequence-specific TAL effectors for modulating mammalian transcription. *nature.com*.
200. Christian, M. *et al.* Targeting DNA double-strand breaks with TAL effector nucleases. *academic.oup.com*.
201. Deveau, H., Garneau, J. E. & Moineau, S. CRISPR/Cas system and its role in phage-bacteria interactions. *Annu Rev Microbiol* **64**, 475–493 (2010).
202. Horvath, P. & Barrangou, R. CRISPR/Cas, the immune system of Bacteria and Archaea. *Science (1979)* **327**, 167–170 (2010).
203. Makarova, K., Haft, D., ... R. B.-N. R. & 2011, undefined. Evolution and classification of the CRISPR–Cas systems. *nature.com*.
204. Bhaya, D., Davison, M. & Barrangou, R. CRISPR-cas systems in bacteria and archaea: Versatile small RNAs for adaptive defense and regulation. *Annu Rev Genet* **45**, 273–297 (2011).
205. Cong, L. *et al.* Multiplex genome engineering using CRISPR/Cas systems. *Science (1979)* **339**, 819–823 (2013).
206. Mali, P. *et al.* RNA-guided human genome engineering via Cas9. *Science (1979)* **339**, 823–826 (2013).

207. Jinek, M. *et al.* RNA-programmed genome editing in human cells. *elifesciences.org* **2**, 471 (2013).
208. Cho, S., Kim, S., Kim, J., biotechnology, J. K.-N. & 2013, undefined. Targeted genome engineering in human cells with the Cas9 RNA-guided endonuclease. *nature.com*.
209. Urnov, F. D., Rebar, E. J., Holmes, M. C., Zhang, H. S. & Gregory, P. D. Genome editing with engineered zinc finger nucleases. *Nature Reviews Genetics* **2010 11:9 11**, 636–646 (2010).
210. Jinek, M. *et al.* A programmable dual-RNA-guided DNA endonuclease in adaptive bacterial immunity. *Science (1979)* **337**, 816–821 (2012).
211. Gasiunas, G., Barrangou, R., Horvath, P. & Siksnys, V. Cas9-crRNA ribonucleoprotein complex mediates specific DNA cleavage for adaptive immunity in bacteria. *Proc Natl Acad Sci U S A* **109**, (2012).
212. Garneau, J., Dupuis, M., Villion, M., Nature, D. R.- & 2010, undefined. The CRISPR/Cas bacterial immune system cleaves bacteriophage and plasmid DNA. *nature.com*.
213. Vujan, A., Jones, S. J. & Zetka, M. NHJ-1 Is Required for Canonical Nonhomologous End Joining in *Caenorhabditis elegans*. *Genetics* **215**, 635–651 (2020).
214. Chemistry, M. L.-J. of B. & 2008, undefined. The mechanism of human nonhomologous DNA end joining. *ASBMB*.
215. Radhakrishnan, S., Jette, N., repair, S. L.-M.-D. & 2014, undefined. Non-homologous end joining: emerging themes and unanswered questions. *Elsevier*.
216. Ceccaldi, R., Rondinelli, B., biology, A. D.-T. in cell & 2016, undefined. Repair pathway choices and consequences at the double-strand break. *Elsevier*.
217. Li, J., Sinica, X. X.-A. B. E. B. & 2016, undefined. DNA double-strand break repair: a tale of pathway choices. *academic.oup.com*.
218. Bétermier, M., Bertrand, P. & Lopez, B. S. Is Non-Homologous End-Joining Really an Inherently Error-Prone Process? *PLoS Genet* **10**, (2014).
219. Karanam, K., Kafri, R., Loewer, A., cell, G. L.-M. & 2012, undefined. Quantitative live cell imaging reveals a gradual shift between DNA repair mechanisms and a maximal use of HR in mid S phase. *Elsevier*.
220. Chiruvella, K., ... Z. L.-C. S. H. & 2013, undefined. Repair of double-strand breaks by end joining. *cshperspectives.cshlp.org* doi:10.1101/cshperspect.a012757.

221. Davis, A. J. & Chen, D. J. DNA double strand break repair via non-homologous end-joining. *Transl Cancer Res* **2**, 130–143 (2013).
222. Gu, J., development, M. L.-G. & & 2008, undefined. Mechanistic flexibility as a conserved theme across 3 billion years of nonhomologous DNA end-joining. *genesdev.cshlp.org* (2008) doi:10.1101/gad.1646608.
223. Chakraborty, A. *et al.* Classical non-homologous end-joining pathway utilizes nascent RNA for error-free double-strand break repair of transcribed genes. *Nature Communications* **2016 7:1 7**, 1–12 (2016).
224. Bolderson, E., Richard, D. J., Zhou, B. B. S. & Khanna, K. K. Recent advances in cancer therapy targeting proteins involved in DNA double-strand break repair. *Clinical Cancer Research* **15**, 6314–6320 (2009).
225. Pardo, B., Gómez-González, B. & Aguilera, A. DNA double-strand break repair: How to fix a broken relationship. *Cellular and Molecular Life Sciences* **66**, 1039–1056 (2009).
226. Malzahn, A., Lowder, L. & Qi, Y. Plant genome editing with TALEN and CRISPR. *Cell & Bioscience* **2017 7:1 7**, 1–18 (2017).
227. Jang, H. K., Song, B., Hwang, G. H. & Bae, S. Current trends in gene recovery mediated by the CRISPR-Cas system. *Exp Mol Med* **52**, 1016 (2020).
228. Symington, L. S. Mechanism and regulation of DNA end resection in eukaryotes. *Crit Rev Biochem Mol Biol* **51**, 195–212 (2016).
229. San Filippo, J., Sung, P. & Klein, H. Mechanism of Eukaryotic Homologous Recombination. <https://doi.org/10.1146/annurev.biochem.77.061306.125255> **77**, 229–257 (2008).
230. West, S. C. The search for a human Holliday junction resolvase. *Biochem Soc Trans* **37**, 519–526 (2009).
231. Heyer, W., Ehmsen, K., genetics, J. L.-A. review of & 2010, undefined. Regulation of homologous recombination in eukaryotes. *annualreviews.org* **44**, 113–139 (2010).
232. Symington, L. S. & Gautier, J. Double-strand break end resection and repair pathway choice. *Annu Rev Genet* **45**, 247–271 (2011).
233. McEwan, D. L., Weisman, A. S. & Hunter, C. P. Uptake of extracellular double-stranded RNA by SID-2. *Mol Cell* **47**, 746 (2012).

234. Winston, W. M., Sutherlin, M., Wright, A. J., Feinberg, E. H. & Hunter, C. P. *Caenorhabditis elegans* SID-2 is required for environmental RNA interference. *Proc Natl Acad Sci U S A* **104**, 10565–10570 (2007).
235. Edgar, R. C. MUSCLE: multiple sequence alignment with high accuracy and high throughput. *Nucleic Acids Res* **32**, 1792–1797 (2004).
236. Milne, I. *et al.* TOPALi: software for automatic identification of recombinant sequences within DNA multiple alignments. *Bioinformatics* **20**, 1806–1807 (2004).
237. Haeussler, M. *et al.* Evaluation of off-target and on-target scoring algorithms and integration into the guide RNA selection tool CRISPOR. *Genome Biol* **17**, 148 (2016).
238. Farboud, B., Severson, A. F. & Meyer, B. J. Strategies for Efficient Genome Editing Using CRISPR-Cas9. *Genetics* **211**, 431–457 (2019).
239. Ma, L. *et al.* The Current State and Future of CRISPR-Cas9 gRNA Design Tools. (2018) doi:10.3389/fphar.2018.00749.
240. Hendel, A. *et al.* Chemically modified guide RNAs enhance CRISPR-Cas genome editing in human primary cells. *Nat Biotechnol* **33**, 985–989 (2015).
241. Kim, S. *et al.* CRISPR RNAs trigger innate immune responses in human cells. *Genome Res* **28**, 367–373 (2018).
242. Cameron, P. *et al.* Mapping the genomic landscape of CRISPR-Cas9 cleavage. *Nat Methods* **14**, 600–606 (2017).
243. Joseph, S., Gheysen, G. & Subramaniam, K. RNA interference in *Pratylenchus coffeae*: knock down of Pc-pat-10 and Pc-unc-87 impedes migration. *Mol Biochem Parasitol* **186**, 51–9 (2012).
244. Boulin, T. & Hobert, O. From genes to function: The *C. elegans* genetic toolbox. *Wiley Interdisciplinary Reviews: Developmental Biology* vol. 1 114–137 Preprint at <https://doi.org/10.1002/wdev.1> (2012).
245. Leonhardt, C. *et al.* Single-cell mRNA transfection studies: delivery, kinetics and statistics by numbers. *Nanomedicine* **10**, 679–688 (2014).
246. Rydzik, A. M. *et al.* Synthetic dinucleotide mRNA cap analogs with tetraphosphate 5', 5' bridge containing methylenebis (phosphonate) modification. *Org Biomol Chem* **7**, 4763–4776 (2009).

247. Lee, J., Boczkowski, D. & Nair, S. Programming human dendritic cells with mRNA. *Synthetic Messenger RNA and Cell Metabolism Modulation: Methods and Protocols* 111–125 (2013).
248. Boczkowski, D., Nair, S. K., Snyder, D. & Gilboa, E. Dendritic cells pulsed with RNA are potent antigen-presenting cells in vitro and in vivo. *J Exp Med* **184**, 465–472 (1996).
249. Sahin, U., Karikó, K. & Türeci, Ö. mRNA-based therapeutics—developing a new class of drugs. *Nat Rev Drug Discov* **13**, 759–780 (2014).
250. Schlager, B., Wang, X., Braach, G. & Sommer, R. J. Molecular cloning of a dominant roller mutant and establishment of DNA-mediated transformation in the nematode *Pristionchus pacificus*. *Genesis* **47**, 300–304 (2009).
251. Mello, C. & Fire, A. DNA transformation. in *Methods in cell biology* vol. 48 451–482 (Elsevier, 1995).
252. Kramer, J. M. & Johnson, J. J. Analysis of mutations in the *sqt-1* and *rol-6* collagen genes of *Caenorhabditis elegans*. *Genetics* **135**, 1035–1045 (1993).
253. Luger, K., Mader, A. W., Richmond, R. K., Sargent, D. F. & Richmond, T. J. *Crystal Structure of the Nucleosome Core Particle at 2.8 Å Resolution*. *Nature* © Macmillan Publishers Ltd vol. 389 <https://www.nature.com/articles/38444.pdf> (1997).
254. Hinz, J. M., Laughery, M. F. & Wyrick, J. J. Nucleosomes inhibit Cas9 endonuclease activity in vitro. *Biochemistry* **54**, 7063–7066 (2015).
255. Singh, R., Kuscu, C., Quinlan, A., Qi, Y. & Adli, M. Cas9-chromatin binding information enables more accurate CRISPR off-target prediction. *Nucleic Acids Res* **43**, e118–e118 (2015).
256. Wu, X. *et al.* Genome-wide binding of the CRISPR endonuclease Cas9 in mammalian cells. *Nat Biotechnol* **32**, 670–676 (2014).
257. Chen, X. *et al.* Probing the impact of chromatin conformation on genome editing tools. *Nucleic Acids Res* **44**, 6482–6492 (2016).
258. Knight, S. C. *et al.* Dynamics of CRISPR-Cas9 genome interrogation in living cells. *Science* **350**, 823–6 (2015).
259. Smith, J. D. *et al.* Quantitative CRISPR interference screens in yeast identify chemical-genetic interactions and new rules for guide RNA design. *Genome Biol* **17**, 45 (2016).
260. Clustal Colour Scheme. <https://www.jalview.org/help/html/colourSchemes/clustal.html>.

261. Adams, S., Pathak, P., Shao, H., Lok, J. B. & da Silva, A. P. Liposome-based transfection enhances RNAi and CRISPR-mediated mutagenesis in non-model nematode systems. *bioRxiv* 429126 (2018).
262. Adams, S., Pathak, P., Shao, H., Lok, J. B. & Pires-daSilva, A. Liposome-based transfection enhances RNAi and CRISPR-mediated mutagenesis in non-model nematode systems. *Scientific Reports* 2019 9:1 **9**, 1–12 (2019).
263. Urwin, P. E., Lilley, C. J. & Atkinson, H. J. Ingestion of Double-Stranded RNA by Preparasitic Juvenile Cyst Nematodes Leads to RNA Interference. <https://doi.org/10.1094/MPMI.2002.15.8.747> **15**, 747–752 (2007).
264. Becker, W. Fluorescence lifetime imaging – techniques and applications. *J Microsc* **247**, 119–136 (2012).
265. Datta, R. *et al.* Fluorescence lifetime imaging microscopy: fundamentals and advances in instrumentation, analysis, and applications. <https://doi.org/10.1117/1.JBO.25.7.071203> **25**, 071203 (2020).
266. Bangham, A. D., Standish, M. M. & Watkins, J. C. Diffusion of univalent ions across the lamellae of swollen phospholipids. *J Mol Biol* **13**, 238–252 (1965).
267. Dimitriadis, G. J. Translation of rabbit globin mRNA introduced by liposomes into mouse lymphocytes. *Nature* 1978 274:5674 **274**, 923–924 (1978).
268. Malone, R. W., Felgner, P. L. & Verma, I. M. Cationic liposome-mediated RNA transfection. *Proc Natl Acad Sci U S A* **86**, 6077 (1989).
269. Martinon, F. *et al.* Induction of virus-specific cytotoxic T lymphocytes in vivo by liposome-entrapped mRNA. *Eur J Immunol* **23**, 1719–1722 (1993).
270. RNA-Immunotherapy of IVAC_W_bre1_uID and IVAC_M_uID - Full Text View - ClinicalTrials.gov. <https://classic.clinicaltrials.gov/ct2/show/NCT02316457>.
271. Miah, K. M., Hyde, S. C. & Gill, D. R. Emerging gene therapies for cystic fibrosis. *Expert Rev Respir Med* **13**, 709–725 (2019).
272. Study Record | ClinicalTrials.gov. <https://www.clinicaltrials.gov/study/NCT04470427?cond=Covid19&intr=mRNA-1273&rank=3>.
273. EGFP :: Fluorescent Protein Database. <https://www.fpbase.org/protein/egfp/>.
274. mCherry :: Fluorescent Protein Database. <https://www.fpbase.org/protein/mcherry/>.

275. Frumkin, I. *et al.* Codon usage of highly expressed genes affects proteome-wide translation efficiency. *Proc Natl Acad Sci U S A* **115**, E4940–E4949 (2018).
276. Simen Zhao, B., Roundtree, I. A. & He, C. S-Adenosyl methionine Post-transcriptional gene regulation by mRNA modifications. *Nature Publishing Group* **18**, 31 (2016).
277. Hughes, T. A. Regulation of gene expression by alternative untranslated regions. *Trends in Genetics* vol. 22 119–122 Preprint at <https://doi.org/10.1016/j.tig.2006.01.001> (2006).
278. Lu, J. *et al.* Types of nuclear localization signals and mechanisms of protein import into the nucleus. *Cell Communication and Signaling* **19**, 1–10 (2021).
279. Darkroom illumination equipment. (1997).
280. Donati, S. & Tambosso, T. Single-Photon Detectors: From Traditional PMT to Solid-State SPAD-Based Technology. *IEEE Journal of Selected Topics in Quantum Electronics* **20**, 204–211 (2014).
281. Craig, F. F., Simmonds, A. C., Watmore, D., McCapra, F. & White, M. R. H. Membrane-permeable luciferin esters for assay of firefly luciferase in live intact cells. *Biochemical Journal* **276**, 637–641 (1991).
282. DeLuca, M. & McElroy, W. D. Kinetics of the Firefly Luciferase Catalyzed Reactions. *Biochemistry* **13**, 921–925 (1974).
283. Imani, M., Hosseinkhani, S., Ahmadian, S. & Nazari, M. Design and introduction of a disulfide bridge in firefly luciferase: increase of thermostability and decrease of pH sensitivity. *Photochemical & Photobiological Sciences* **9**, 1167–1177 (2010).
284. Mehrabi, M., Hosseinkhani, S. & Ghobadi, S. Stabilization of firefly luciferase against thermal stress by osmolytes. *Int J Biol Macromol* **43**, 187–191 (2008).
285. Rasouli, S., Hosseinkhani, S., Yaghmaei, P. & Ebrahim-Habibi, A. Effects of sucrose and trehalose on stability, kinetic properties, and thermal aggregation of firefly luciferase. *Appl Biochem Biotechnol* **165**, 572–582 (2011).
286. Lohrasbi-Nejad, A., Torkzadeh-Mahani, M. & Hosseinkhani, S. Hydrophobin-1 promotes thermostability of firefly luciferase. *FEBS J* **283**, 2494–2507 (2016).
287. Kakaire, S., Grove, I. G. & Haydock, P. P. J. Effect of temperature on the life cycle of *Heterodera schachtii* infecting oilseed rape (*Brassica napus* L.). *Nematology* **14**, 855–867 (2012).

288. Green, O. *et al.* Opening a Gateway for Chemiluminescence Cell Imaging: Distinctive Methodology for Design of Bright Chemiluminescent Dioxetane Probes. *ACS Cent Sci* **3**, 349–358 (2017).
289. Hattori, M. *et al.* Confocal Bioluminescence Imaging for Living Tissues with a Caged Substrate of Luciferin. *Anal Chem* **88**, 6231–6238 (2016).
290. Lippert, A. R. Unlocking the Potential of Chemiluminescence Imaging. *ACS Cent Sci* **3**, 269–271 (2017).
291. Yu, X. *et al.* Improved delivery of Cas9 protein/gRNA complexes using lipofectamine CRISPRMAX. *Biotechnol Lett* **38**, 919–929 (2016).
292. LeBlanc, C. *et al.* Increased efficiency of targeted mutagenesis by CRISPR/Cas9 in plants using heat stress. *The Plant Journal* **93**, 377–386 (2018).
293. Xiang, G., Zhang, X., An, C., Cheng, C. & Wang, H. Temperature effect on CRISPR-Cas9 mediated genome editing. *Journal of Genetics and Genomics* **44**, 199–205 (2017).
294. Chen, F. *et al.* Targeted activation of diverse CRISPR-Cas systems for mammalian genome editing via proximal CRISPR targeting. *Nature Communications* 2017 8:1 **8**, 1–12 (2017).
295. Park, H., Shin, J., Choi, H., Cho, B. & Kim, J. Valproic Acid Significantly Improves CRISPR/Cas9-Mediated Gene Editing. *Cells* 2020, Vol. 9, Page 1447 **9**, 1447 (2020).
296. Gaudelli, N. M. *et al.* Programmable base editing of A•T to G•C in genomic DNA without DNA cleavage. *Nature* 2017 551:7681 **551**, 464–471 (2017).
297. Endo, B. Y. Penetration+ Development of *Heterodera glycines* in Soybean Roots+ Related Anatomical Changes. *Phytopathology* **54**, 79 (1964).
298. Hermsmeier, D., Mazarei, M. & Baum, T. J. Differential Display Analysis of the Early Compatible Interaction Between Soybean and the Soybean Cyst Nematode. <https://doi.org/10.1094/MPMI.1998.11.12.1258> **11**, 1258–1263 (2007).
299. Hofmann, J. *et al.* Metabolic profiling reveals local and systemic responses of host plants to nematode parasitism. *Plant J* **62**, 1058–1071 (2010).
300. Ithal, N. *et al.* Developmental transcript profiling of cyst nematode feeding cells in soybean roots. *Mol Plant Microbe Interact* **20**, 510–525 (2007).

301. Puthoff, D. P., Nettleton, D., Rodermel, S. R. & Baum, T. J. Arabidopsis gene expression changes during cyst nematode parasitism revealed by statistical analyses of microarray expression profiles. *Plant J* **33**, 911–921 (2003).
302. Wan, J. *et al.* Whole-genome gene expression profiling revealed genes and pathways potentially involved in regulating interactions of soybean with cyst nematode (*Heterodera glycines* Ichinohe). *BMC Genomics* **16**, 1–14 (2015).
303. Szakasits, D. *et al.* The transcriptome of syncytia induced by the cyst nematode *Heterodera schachtii* in Arabidopsis roots. *Plant Journal* **57**, 771–784 (2009).
304. Panella, L. & Lewellen, R. T. Broadening the genetic base of sugar beet: introgression from wild relatives. *Euphytica* **154**, 383–400 (2006).
305. Cai, D. *et al.* Positional cloning of a gene for nematode resistance in sugar beet. *Science* **275**, 832–834 (1997).
306. Cheng, C. Y. *et al.* Araport11: a complete reannotation of the Arabidopsis thaliana reference genome. *Plant Journal* **89**, 789–804 (2017).
307. Details - Arabidopsis_thaliana - Ensembl Genomes 66. https://ensembl.gemene.org/Arabidopsis_thaliana/Info/Annotation/#assembly.
308. Kover, P. X. *et al.* A Multiparent Advanced Generation Inter-Cross to Fine-Map Quantitative Traits in Arabidopsis thaliana. *PLoS Genet* **5**, e1000551 (2009).
309. Zhu, Y. *et al.* Large-scale field phenotyping using backpack LiDAR and CropQuant-3D to measure structural variation in wheat. *Plant Physiol* **187**, 716–738 (2021).
310. Colmer, J. *et al.* SeedGerm: a cost-effective phenotyping platform for automated seed imaging and machine-learning based phenotypic analysis of crop seed germination. *New Phytologist* **228**, 778–793 (2020).
311. Tardieu, F., Cabrera-Bosquet, L., Pridmore, T. & Bennett, M. Plant Phenomics, From Sensors to Knowledge. *Current Biology* **27**, R770–R783 (2017).
312. Mochida, K. *et al.* Computer vision-based phenotyping for improvement of plant productivity: a machine learning perspective. *Gigascience* **8**, 1–12 (2019).
313. Mutka, A. M. & Bart, R. S. Image-based phenotyping of plant disease symptoms. *Front Plant Sci* **5**, 734 (2015).
314. Canny, J. A Computational Approach to Edge Detection. *IEEE Trans Pattern Anal Mach Intell* **PAMI-8**, 679–698 (1986).

315. Lowe, D. G. Object recognition from local scale-invariant features. *Proceedings of the IEEE International Conference on Computer Vision* **2**, 1150–1157 (1999).
316. Lecun, Y., Bengio, Y. & Hinton, G. Deep learning. *Nature* **521**, 436–444 (2015).
317. Jiao, L. *et al.* A survey of deep learning-based object detection. *IEEE Access* **7**, 128837–128868 (2019).
318. Zhou, J. *et al.* Leaf-GP: An open and automated software application for measuring growth phenotypes for arabidopsis and wheat. *Plant Methods* **13**, 1–17 (2017).
319. Halcro, K. *et al.* The BELT and phenoSEED platforms: Shape and colour phenotyping of seed samples. *Plant Methods* **16**, 1–13 (2020).
320. Pound, M. P., Fozard, S., Torres Torres, M., Forde, B. G. & French, A. P. AutoRoot: Open-source software employing a novel image analysis approach to support fully-automated plant phenotyping. *Plant Methods* **13**, 1–10 (2017).
321. Raspberry Pi Documentation - Raspberry Pi hardware. <https://www.raspberrypi.com/documentation/computers/raspberry-pi.html#voltage-specifications>.
322. Raspberry Pi Documentation - Camera software. https://www.raspberrypi.com/documentation/computers/camera_software.html.
323. Valle, B. *et al.* PYM: A new, affordable, image-based method using a Raspberry Pi to phenotype plant leaf area in a wide diversity of environments. *Plant Methods* **13**, 1–17 (2017).
324. Hull, C. W. & Arcadia, C. Apparatus for production of three-dimensional objects by stereolithography. (1984).
325. Apparatus and method for creating three-dimensional objects. (1989).
326. Legland, D., Arganda-Carreras, I. & Andrey, P. MorphoLibJ: Integrated library and plugins for mathematical morphology with ImageJ. *Bioinformatics* **32**, 3532–3534 (2016).
327. Reinhard, E., Ashikhmin, M., Gooch, B. & Shirley, P. Color transfer between images. *IEEE Comput Graph Appl* **21**, 34–41 (2001).

328. Rogers, H., Baricz, N. & Pawar, K. S. 3D printing services: classification, supply chain implications and research agenda. *International Journal of Physical Distribution and Logistics Management* **46**, 886–907 (2016).
329. 3D People UK | 3D Printing Service | Order Online. <https://www.3dpeople.uk/>.
330. Puchalt, J. C., Gonzalez-Rojo, J. F., Gómez-Escribano, A. P., Vázquez-Manrique, R. P. & Sánchez-Salmerón, A. J. Multiview motion tracking based on a cartesian robot to monitor *Caenorhabditis elegans* in standard Petri dishes. *Scientific Reports* **2022 12:1** **12**, 1–11 (2022).
331. The Great Raspberry Pi Shortage Might Be Coming to an End. <https://www.howtogeek.com/894161/the-great-raspberry-pi-shortage-might-be-coming-to-an-end/>.
332. These 169 industries are being hit by the global chip shortage. https://finance.yahoo.com/news/these-industries-are-hit-hardest-by-the-global-chip-shortage-122854251.html?guccounter=1&guce_referrer=aHR0cHM6Ly9lbi53aWtpcGVkaWEub3JnLw&guce_referrer_sig=AQAAAIJtMEGO9ypS4EoYq3Zww-Kdm1fc7emYRBoo0RG03USDBRcFt6ZphgGI2A_QpM_GzRohPm70lrTtXup2roloZVFOLsNGi51gX5spWHlh9VtotoBq2cZDuzWAIMiiHqxSaO1IM33NIQ7CDyP6qe-aPh1Ao_3YPIRXAHuVHI4z9eQz.
333. The Meaning of Light and Color. <https://hubblesite.org/contents/articles/the-meaning-of-light-and-color>.
334. Zhang, Q. *et al.* Knock-Down of Arabidopsis PLC5 Reduces Primary Root Growth and Secondary Root Formation While Overexpression Improves Drought Tolerance and Causes Stunted Root Hair Growth. *Plant Cell Physiol* **59**, 2004–2019 (2018).
335. Steele, A. E. Invasion of Sugarbeet Leaf Blades by Larvae of *Heterodera schachtii*. *J Nematol* **13**, 91 (1981).
336. Golinowski, W., Grundler, F. M. W. & Sobczak, M. *Changes in the Structure Of Arabidopsis Thaliana during Female Development of the Plant-Parasitic Nematode Heterodera Schachtii*. *Protoplasma* vol. 194 (1996).
337. Dobin, A. *et al.* STAR: ultrafast universal RNA-seq aligner. *Bioinformatics* **29**, 15–21 (2013).

338. Anders, S., Pyl, P. T. & Huber, W. HTSeq—a Python framework to work with high-throughput sequencing data. *Bioinformatics* **31**, 166 (2015).
339. Love, M. I., Huber, W. & Anders, S. Moderated estimation of fold change and dispersion for RNA-seq data with DESeq2. *Genome Biol* **15**, 1–21 (2014).
340. Shanmukhan, A. P. *et al.* Regulation of touch dependant de novo root regeneration in Arabidopsis. *bioRxiv* 2020.11.04.367714 (2020) doi:10.1101/2020.11.04.367714.
341. Liu, G. *et al.* Detached and Attached Arabidopsis Leaf Assays Reveal Distinctive Defense Responses Against Hemibiotrophic Colletotrichum spp. <https://doi.org/10.1094/MPMI-20-10-1308> **20**, 1308–1319 (2007).
342. Bailey-Serres, J. & Colmer, T. D. Plant tolerance of flooding stress – recent advances. *Plant Cell Environ* **37**, 2211–2215 (2014).
343. Pierik, R., Djakovic-Petrovic, T., Keuskamp, D. H., De Wit, M. & Voesenek, L. A. C. J. Auxin and Ethylene Regulate Elongation Responses to Neighbor Proximity Signals Independent of Gibberellin and DELLA Proteins in Arabidopsis. *Plant Physiol* **149**, 1701–1712 (2009).
344. Siddique, S. *et al.* Myo-inositol oxygenase genes are involved in the development of syncytia induced by Heterodera schachtii in Arabidopsis roots. *New Phytologist* **184**, 457–472 (2009).
345. Wieczorek, K. *et al.* Expansins are involved in the formation of nematode-induced syncytia in roots of Arabidopsis thaliana. *The Plant Journal* **48**, 98–112 (2006).
346. Zhang, S. *et al.* Functional Characterization of the 1-Deoxy-D-Xylulose 5-Phosphate Synthase Genes in Morus notabilis. *Front Plant Sci* **11**, 521621 (2020).
347. Pracharoenwattana, I., Zhou, W. & Smith, S. M. Fatty acid beta-oxidation in germinating Arabidopsis seeds is supported by peroxisomal hydroxypyruvate reductase when malate dehydrogenase is absent. *Plant Mol Biol* **72**, 101–109 (2010).
348. Pracharoenwattana, I., Cornah, J. E. & Smith, S. M. Arabidopsis peroxisomal malate dehydrogenase functions in β -oxidation but not in the glyoxylate cycle. *Plant Journal* **50**, 381–390 (2007).
349. Konishi, N. *et al.* Cytosolic Glutamine Synthetase Isozymes Play Redundant Roles in Ammonium Assimilation Under Low-Ammonium Conditions in Roots of Arabidopsis thaliana. *Plant Cell Physiol* **59**, 601–613 (2018).
350. Givan, C. V. The Biochemistry of Plants. A Comprehensive Treatise. Preprint at (1980).

351. von Mering, C. *et al.* STRING: a database of predicted functional associations between proteins. *Nucleic Acids Res* **31**, 258 (2003).
352. Xu, Z., Mahmood, K. & Rothstein, S. J. ROS Induces Anthocyanin Production Via Late Biosynthetic Genes and Anthocyanin Deficiency Confers the Hypersensitivity to ROS-Generating Stresses in Arabidopsis. *Plant Cell Physiol* **58**, 1364–1377 (2017).
353. Gou, J. Y., Felippes, F. F., Liu, C. J., Weigel, D. & Wang, J. W. Negative Regulation of Anthocyanin Biosynthesis in Arabidopsis by a miR156-Targeted SPL Transcription Factor. *Plant Cell* **23**, 1512–1522 (2011).
354. Janeeshma, E., Rajan, V. K. & Puthur, J. T. Spectral variations associated with anthocyanin accumulation; an apt tool to evaluate zinc stress in *Zea mays* L. *Chemistry and Ecology* **37**, 32–49 (2021).
355. Mo, X. *et al.* Phosphate (Pi) starvation up-regulated *gmcsn5a/b* participates in anthocyanin synthesis in soybean (*glycine max*) dependent on pi availability. *Int J Mol Sci* **22**, (2021).
356. Marowa, P., Ding, A. & Kong, Y. Expansins: roles in plant growth and potential applications in crop improvement. *Plant Cell Rep* **35**, 949 (2016).
357. An, Y. Q., Huang, S., McDowell, J. M., McKinney, E. C. & Meagher, R. B. Conserved expression of the Arabidopsis ACT1 and ACT 3 actin subclass in organ primordia and mature pollen. *Plant Cell* **8**, 15–30 (1996).
358. Vitale, A., Wu, R. J., Cheng, Z. & Meagher, R. B. Multiple conserved 5' elements are required for high-level pollen expression of the Arabidopsis reproductive actin ACT1. *Plant Mol Biol* **52**, 1135–1151 (2003).
359. Cosma, M. A., Curtis, N. L., Pain, C., Kriechbaumer, V. & Bolanos-Garcia, V. M. Biochemical, biophysical, and functional characterisation of the E3 ubiquitin ligase APC/C regulator CDC20 from Arabidopsis thaliana. *Front Physiol* **13**, 938688 (2022).
360. De Almeida Engler, J. *et al.* Molecular markers and cell cycle inhibitors show the importance of cell cycle progression in nematode-induced galls and syncytia. *Plant Cell* **11**, 793–807 (1999).
361. De Almeida Engler, J. & Gheysen, G. Nematode-Induced Endoreduplication in Plant Host Cells: Why and How? <https://doi.org/10.1094/MPMI-05-12-0128-CR> **26**, 17–24 (2012).

362. van Damme, D. *et al.* Arabidopsis α Aurora Kinases Function in Formative Cell Division Plane Orientation. *Plant Cell* **23**, 4013–4024 (2011).
363. Wu, J. *et al.* Deficient plastidic fatty acid synthesis triggers cell death by modulating mitochondrial reactive oxygen species. *Cell Res* **25**, 621–633 (2015).
364. Mou, Z., He, Y., Dai, Y., Liu, X. & Li, J. Deficiency in Fatty Acid Synthase Leads to Premature Cell Death and Dramatic Alterations in Plant Morphology. *Plant Cell* **12**, 405 (2000).
365. Marella, H. H., Nielsen, E., Schachtman, D. P. & Taylor, C. G. The amino acid permeases AAP3 and AAP6 are involved in root-knot nematode parasitism of Arabidopsis. *Mol Plant Microbe Interact* **26**, 44–54 (2013).
366. Wiśniewska, A., Wojszko, K., Róžańska, E., Lenarczyk, K. & Sobczak, M. Arabidopsis thaliana AtHRS1 gene is involved in the response to Heterodera schachtii infection and its overexpression hampers development of syncytia and involves a jasmonic acid-dependent mechanism. *J Plant Physiol* **272**, (2022).
367. Zhao, Q. *et al.* Pinoresinol reductase 1 impacts lignin distribution during secondary cell wall biosynthesis in Arabidopsis. *Phytochemistry* **112**, 170–178 (2015).
368. Chen, Y. *et al.* Identification of the Abundant Hydroxyproline-Rich Glycoproteins in the Root Walls of Wild-Type Arabidopsis, an ext3 Mutant Line, and Its Phenotypic Revertant. *Plants* 2015, Vol. 4, Pages 85-111 **4**, 85–111 (2015).
369. Schultz, C. J., Hsu, M., Miesak, B. & Coruzzi, G. M. Arabidopsis Mutants Define an in Vivo Role for Isoenzymes of Aspartate Aminotransferase in Plant Nitrogen Assimilation. *Genetics* **149**, 491–499 (1998).
370. Eswaramoorthy, S., Bonanno, J. B., Burley, S. K. & Swaminathan, S. Mechanism of action of a flavin-containing monooxygenase. *Proc Natl Acad Sci U S A* **103**, 9832–9837 (2006).
371. Pucker, B., Kleinbölting, N. & Weisshaar, B. Large scale genomic rearrangements in selected Arabidopsis thaliana T-DNA lines are caused by T-DNA insertion mutagenesis. *BMC Genomics* **22**, 1–21 (2021).
372. Donaldson, L. Autofluorescence in Plants. *Molecules* **25**, (2020).
373. Baschong, W., Suetterlin, R. & Hubert Laeng, R. Learn how to Remove Autofluorescence from your Confocal Images. *Journal of Histochemistry and Cytochemistry* **49**, 1565–1571 (2020).

374. Liljeruhm, J. *et al.* Engineering a palette of eukaryotic chromoproteins for bacterial synthetic biology. *J Biol Eng* **12**, 1–10 (2018).
375. Philip, S. M., Fosu-Nyarko, J., Iqbal, S., Wang, Z. & Jones, M. G. K. In-plant activation of root-specific expression of a cytotoxic gene disrupts the development of the root-knot nematode, *Meloidogyne javanica*. *Plant Pathol* **71**, 702–714 (2022).
376. Sternberg, N., biology, D. H.-J. of molecular & 1981, undefined. Bacteriophage P1 site-specific recombination: I. Recombination between loxP sites. *Elsevier*.
377. Meinke, G., Bohm, A., Hauber, J., Pisabarro, M. T. & Buchholz, F. Cre Recombinase and Other Tyrosine Recombinases. *Chem Rev* **116**, 12785–12820 (2016).
378. Branda, C., cell, S. D.-D. & 2004, undefined. Talking about a revolution: The impact of site-specific recombinases on genetic analyses in mice. *cell.comCS Branda, SM DymeckiDevelopmental cell, 2004•cell.com*.
379. Gossen, M. & Bujard, H. Tight control of gene expression in mammalian cells by tetracycline-responsive promoters. *Proc Natl Acad Sci U S A* **89**, 5547–5551 (1992).
380. Brocard, J. *et al.* Spatio-temporally controlled site-specific somatic mutagenesis in the mouse. *Proc Natl Acad Sci U S A* **94**, 14559–14563 (1997).
381. Kühn, R., Schwenk, F., Aguet, M. & Rajewsky, K. Inducible gene targeting in mice. *Science* **269**, 1427–1429 (1995).
382. Metzger, D., Methods, P. C.- & 2001, undefined. Site-and time-specific gene targeting in the mouse. *Elsevier* **24**, 71–80 (2001).
383. Kim, H., Kim, M., Im, S. K. & Fang, S. Mouse Cre-LoxP system: general principles to determine tissue-specific roles of target genes. *Lab Anim Res* **34**, 147 (2018).
384. Hirrlinger, J. *et al.* Split-cre complementation indicates coincident activity of different genes in vivo. *PLoS One* **4**, (2009).
385. Odell, J. T., Hoopes, J. L. & Vermerris, W. Seed-specific gene activation mediated by the Cre/lox site-specific recombination system. *Plant Physiol* **106**, 447 (1994).
386. Wu, J. *et al.* A non-invasive far-red light-induced split-Cre recombinase system for controllable genome engineering in mice. *Nature Communications* 2020 11:1 **11**, 1–11 (2020).
387. Chen, J. *et al.* Off-target effects of RNAi correlate with the mismatch rate between dsRNA and non-target mRNA. *RNA Biol* **18**, 1747 (2021).

388. Kage-Nakadai, E. *et al.* A Conditional Knockout Toolkit for *Caenorhabditis elegans* Based on the Cre/loxP Recombination. *PLoS One* **9**, (2014).
389. Mundt, C. C. Durable resistance: A key to sustainable management of pathogens and pests. *Infection, Genetics and Evolution* **27**, 446–455 (2014).
390. Engelhardt, Stam, R. & Hükelhoven, R. Good Riddance? Breaking Disease Susceptibility in the Era of New Breeding Technologies. *Agronomy 2018, Vol. 8, Page 114* **8**, 114 (2018).
391. chia56028/Color-Transfer-between-Images: This is the open-source implement the paper 'Color Transfer between Images' by Erik Reinhard, Michael Ashikhmin, Bruce Gooch and Peter Shirley. <https://github.com/chia56028/Color-Transfer-between-Images>.